THERMOMECHANICAL BEHAVIORS OF ACTIVE NETWORK POLYMERS

A Dissertation
Presented to
The Academic Faculty

by

Kai Yu

In Partial Fulfillment
of the Requirements for the Degree
Doctor of Philosophy in the
The George W.Woodruff School of Mechanical Engineering

Georgia Institute of Technology
August, 2015

THERMOMECHANICAL BEHAVIORS OF ACTIVE NETWORK POLYMERS

Approved by:

Dr. H. Jerry Qi, Advisor
The George W.Woodruff School of Mechanical Engineering
Georgia Institute of Technology

Dr. David L. McDowell
The George W.Woodruff School of Mechanical Engineering
Georgia Institute of Technology

Dr. Min Zhou
The George W.Woodruff School of Mechanical Engineering
Georgia Institute of Technology

Dr. Ken Gall
School of Materials Science and Engineering
Georgia Institute of Technology

Dr. Karl I. Jacob
School of Materials Science and Engineering
Georgia Institute of Technology

Dr. Zhiqun Lin
School of Materials Science and Engineering
Georgia Institute of Technology

Date Approved: [April 7th, 2015]

ACKNOWLEDGEMENTS

I would never finish this dissertation without the generous support from many people inside and outside of the George W. Woodruff School of Mechanical Engineering at Georgia Tech. I would like to express my gratitude to all of them.

First and foremost, my deepest gratitude is to my advisor, Prof. H. Jerry Qi, for his continuous support, unique perspective and insights on my study and research in the past four and half years. I never imagined before that an advisor could also be my friend, life mentor and career instructor outside of the academic world. Thanks to him, my Ph.D adventure turns out to be a productive and pleasant journey. He has also given me invaluable advice on my teaching and presenting skills from which I will benefit through my career.

I also acknowledge my thesis committee members, Prof. McDowell, Prof. Zhou, Prof. Gall, Prof. Jacob and Prof. Lin, who agreed to serve on my Ph.D committee despite their tight schedules. Their challenging questions and bountiful support contributed to the success of my research projects. Special gratitude presents to Prof. Zhou, Prof. Gall and Prof. Jacob for their kind references for my job searching.

I would like to thank Prof. Yifu Ding, Prof. Jianliang Xiao and Prof. Martin L Dunn. I won't forget those days when we shared ideas together when I was in the University of Colorado at Boulder. Their knowledge, valuable discussions and accessibility tremendously enriched my Ph.D research. I am also thankful to all my previous and current lab mates for the wonderful discussion, collaboration and pleasant time together.

Finally, I wish to thank my parents, my sister and brother-in-law for their support and encouragement throughout this endeavor, and have been a constant source of unconditional love, concern and strength all these years. To them, I dedicate this dissertation.

TABLE OF CONTENTS

ACKNOWLEDGEMENTS III
LIST OF TABLES VI
LIST OF FIGURES VII
LIST OF ABBREVIATIONS AND SYMBOLS XIII
Chapter 1 INTRODUCTION 1
1.1 Background 1
1.2 Research Motivation and Goals 7
1.3 Thesis Plan 9
1.4 References 9
Chapter 2 ONE-DIMENSIONAL CONSTITUTIVE MODELING OF SHAPE MEMORY POLYMERS 18
2.1 Glass Transition in Amorphous Polymers 18
2.2 1D Constitutive Modeling based on Thermoviscoelasticity 19
2.3 Material Parameters Identification 22
2.4 Predictions on the Shape Fixity and Recovery 25
2.5 Influence of Stretch Induced Softening Effect on the Free Recovery Behavior 26
2.6 Multi-shape Memory Effect and Associated Energy Releasing Mechanism 30
2.7 Conclusion 34
2.8 References 34
Chapter 3 A UNIFIED METHOD TO PREDICT SHAPE FIXITY AND RECOVERY OF SHAPE MEMORY POLYMERS 38
3.1 Experimental Observations on Shape Fixity and Recovery 38
3.2 A Unified Parameter: Reduced Time 41
3.3 A Master Performance Map 47
3.4 Application in Studying the Temperature Memory Effect 49
3.5 Conclusion 56
Appendix A: Influence of Loading Rate and Thermal Expansion 57
3.6 References 60
Chapter 4 THREE-DIMENSIONAL FINITE DEFORMATION CONSTITUTIVE MODELING FOR SHAPE MEMORY POLYMERS 63

4.1 Constitutive Relations 63
4.2 Material Parameters Identification 67
4.3 Applications in the Studying of SMP Composites 71
4.4 Conclusion 84
Appendix B: 3D Fluid-Structure (FS) Simulation on the Microvascular SMP Composite 85
4.5 References 86
Chapter 5 COVALENT ADAPTIVE NETWORKS WITH BOND EXCHANGE REACTIONS 89
5.1 Material 90
5.2 Glass Transition Behavior 92
5.3 Stress Relaxation Behavior 93
5.4 Reprocessing, Recycling and Repairing Capability based on Surface Welding 101
5.5 Conclusion 111
5.6 References 112
Chapter 6 INTERFACIAL MECHANICS OF COVALENT ADAPTIVE NETWORKs 115
6.1 Experimental and Results 115
6.2. Constitutive Modeling 118
6.3. Results and Discussions 126
6.4 Conclusion 133
6.5 References 134
Chapter 7 OVERALL CONCLUSIONS AND RECOMMENDED FUTURE WORK 137
7.1 Overall Conclusions 137
7.2 Future Work Recommendation 138
7.3 References 139
VITA 140

LIST OF TABLES

Table 2-1. Parameters of the multi-branched constitutive model 25
Table 2-2. Relaxation times (in minutes) of individual rubbery branches at different temperatures 32
Table 3-1. The reduced programming times before unloading in the two programming conditions that achieve the same shape fix ratio (90%) 44
Table 4-1. Physical properties of the 316 stainless steel microvascular tubes 78
Table 5-1. Stoichiometry (normalized mole content) of each composition 91

LIST OF FIGURES

Figure 1.1. Schematic views of (a) glass transition (modified according to [3]) and (b) phase evolution 2
Figure 1.2. Typical actuation methods for the thermally sensitive SMPs. (a) Direct heating [64], (b) Magnetic actuation [48], (c) Electric actuation [54], (d) Infrared light actuation [56] and (e) Water actuation[59]. 3
Figure 1.3. Typical applications of SMPs. (a) SMP suture [65], (b) SMP stent [66] and (c) SMP controlling the surface pattern [68] 4
Figure 1.4. (a) A schematic illustration of the thermomechanical history of the programming and free recovery process in an SM cycle. (b) A typical free recovery curve as a function of time. 5
Figure 1.5. Schematic of bond exchange reactions (BERs) 6
Figure 1.6. Stress relaxation in thermosetting polymers based on the BERs 7
Figure 1.7. Reprocessing of broken epoxy active network polymer in an injection machine to recover its initial aspect [73] 7
Figure 2.1. 1D rheological representation of the developed model 21
Figure 2.2. Stress relaxation tests and shifting factors: (a) Stress relaxation tests at temperatures increasing from 15 ℃ to 45 ℃ with 2.5 ℃ interval. (b) The stress relaxation master curve at 27.5 ℃. (c) Shifting factors at different temperatures 24
Figure 2.3. 1D estimation for the DMA result of SMP by using NLREG software. The original experimental curves are shown in solid lines 25
Figure 2.4. Predictions on the experimentally tested shape fixity and recovery. (a) Shape fixity. Dot data indicates experimental results. (b) Shape recovery ratio. Solid lines indicate experimental results. 26
Figure 2.5. Stretch induced softening effect in SMP composite and its influence on the free recovery behavior. (a) Cyclic tension tests on SMP composites with 9 wt% CB. The strain amplitude is fixed amplitude at 10%. (n) Shape recovery ratio plot as a function of heating. Two samples were pre-stretched to 10% and 20% respectively during the programming step 27
Figure 2.6. Shape recovery ratio plot as a function of heating time during the free recovery of CB9 SMP composites. Solid lines denote experimental results and dash line denotes corresponding simulations. 29
Figure 2.7. Multi-SME simulated under stress controlled programming and staged heating recovery conditions. (a) temperature and stress history. (b) strain evolution in both simulation and experiment. 31
Figure 2.8. (a) Strain evolution of dashpots in each rubbery nonequilibrium branch during the free recovery process of multi-SME simulation. Key: solid line, normalized strain release; dotted line, temperature. (b) Elastic strain energy stored in each rubbery branch 33

Figure 3.1. Shape fixity and shape recovery behavior of SMP programmed at different temperatures (T_d). (a) Shape fix ratio and Shape recovery time ($t_{0.95}$) as a function of programming temperature (evenly distributed from 25^{o}C to 50^{o}C) (b) Shape recovery ratio as a function of heating time. (c) Free shape recovery behavior of SMP under different recovery temperatures (T_r). T_r is taken as four different temperatures: 30 ℃, 35 ℃, 40 ℃ and 50 ℃ respectively. 40
Figure 3.2. (a) Shape fixity as a function of programming temperature (T_d) and holding time at T_d. Note: Dots denote the experimental results and solid lines denote simulation results, which is discussed in detail in the following section; The low temperature T_L is always 20 ^{o}C in all the experimental cases. (b) Shape recovery behavior of SMPs experienced by two programming conditions that achieve the same shape fix ratio (90%). 41
Figure 3.3. Stress evolutions in each branch of the multi-branch model during the two programming processes that achieve the same shape fixity (90%). Note: the number in the x-axis label denotes the *i-th* nonequilibrium branch 42
Figure 3.4. Stress status within the multi-branch model at different physical programming time but the same reduced programming time for two different programming conditions 45
Figure 3.5. After transferring the physical free recovery time into the reduced free recovery time, the four shape recovery curves joined to form a master free recovery curve. 46
Figure 3.6. Prediction on the shape recovery behavior at different recovery temperatures. (a) The recovery temperature in each case is 27.5 ^{o}C while the programming temperature varies to achieve different shape fix ratio. Note: the 98.7% shape fixity represent the actual experimental results where the programming temperature is 40 ^{o}C (b) Selecting R_f= 98.7% shape recovery curve as the master curve, then transfer the reduced time back into the real physical free recovery time according to the specified thermal condition (the dash lines represent the corresponding recovery temperatures) (c) Comparisons between the simulation and experimental results. The simulation curves are denoted as dash lines 47
Figure 3.7. The shape memory performance map. (a) A general referential contour. (b) Reduced programming time as a function of holding time and programming temperature T_d. (c) Reduced free recovery time as a function of heating temperature T_H. Note: Other influencing factors are: Loading rate=1%/s; Cooling rate=2.5^{o}C/min; T_L=20^{o}C; Holding time at T_L=1hour; Heating rate=2.5^{o}C/min. 49
Figure 3.8. Influence of programming temperature and heating rate on the temperature dependent. (a) shape recovery ratio and (b) normalized shape recovery speed. Note: the dash line denote simulation curves by using the 1D multi-branch model. 51
Figure 3.9. Parametric study on the influence of programing temperature and holding time. (a) Shape recovery ratio as a function of recovery temperature. (b) Shape recovery

ratio with different holding times. T_d=35 ^{o}C. (b) T_c plotted as a function of both holding time t_h and T_d..... 52
Figure 3.10. (a) The constructed master curve of Tc. the referece holding time t_{h0}=6 ×10^{1}s. (b) The holding time dependent shift factors during the construction of master curve.... 54
Figure 3.11. Influence of both Td and heating rate q on the free recovery profiles and Tc of SMPs. (a) The predicted free recovery curves with different heating rates. T_d=35 ^{o}C and holding time equals to 6s. (b) T_c plotted as a function of both T_d and q. (c) The constructed master curve of T_c. The referece heating rate q_0=10^{0} ^{o}C/min. (d) The heating rate dependent shift factors during the construction of master curve. 56
Figure 4.1. 1D rheological representation for the 3D finite deformation constitutive model..... 64
Figure 4.2. Experimental results from the thermal expansion experiments (CTE). 69
Figure 4.3. Stress-strain behavior of Veriflex E epoxy SMP at different temperatures. (a) 25^{o}C, (b) 60^{o}C, (c) 90^{o}C, (d) 100^{o}C, (e) 110^{o}C and (f) 130^{o}C. Note: Finite simulations are denoted as dash lines and the experimental data is copied from McClung et al[11]..... 71
Figure 4.4. a) The 3D representative volume element (RVE) for a magnetic particles reinforced SMP composite. Note: Point A represents one of the farthest points from the magnetic particle heating surface on the 3D RVE. (b) Finite element model mesh for the 3D RVE for a filler volume fraction of 1% and a filler diameter of 1 *m*m..... 72
Figure 4.5. Mises stress distribution within the 3D RVE during the finite element analysis 74
Figure 4.6. The strain recovery ratio and temperature of the 3D RVE during the free recovery process. Note: temperature data is collected on point A on the 3D RVE..... 74
Figure 4.7. Temperature distribution within the 3D RVE during the finite element analysis..... 75
Figure 4.8. Hydraulic pressure evolution on the curved surface of 3D RVE during the particle heating process..... 75
Figure 4.9. Prediction of critical particle diameters by showing effect of particle size on shape recovery time of the SMP composites 77
Figure 4.10. Modeling method of the SMP composite in ABAQUS. (a) A representative microvascular SMP composite in the 3D setting. (b) A cross-sectional view of the 3D model. (c) The finite element meshing result with temperature reference points. 78
Figure 4.11. Comparisons between the simulation and experiments. The shape recovery ratio is captured on Point 3 in the stretching direction 79
Figure 4.12. Temperature distribution within the half-size periodic model during the shape memory cycle. Note: the dash boxes indicate the initial size of the periodic model without defamation. 80
Figure 4.13. Evolution of temperature and shape recovery ratio on Point 1, Point 2 and Point 3 respectively, as well as the shape recovery ratio of the model in the stretching

direction (R_r). Note: the shape recovery ratios on Point 1, Point 2 and Point 3 are collected in the thickness direction. 80
Figure 4.14. Density and total shape recovery times of the SMP composite under different tube spaces and composite thickness. 82
Figure 4.15. (a) Temperature variation on Points 1 and 4 as a function heating time and composite thickness. (b) Normalized shape recovery time plot as a function of location of tube center (measure from the top surface) and composite thickness. Note: for each curve, the data points are normalized by the initial value, namely the shape recovery time when the tube depth is 0.5B..... 83
Figure 5.1. Schematic view of the chemical reagents used in this study, as well as the reactant repeating unit after synthesis. 91
Figure 5.2. Comparisons of glass transition behavior of the five epoxy samples. (a) Tan δ curves as a function of temperature. The T_g is taken to be the temperature corresponding to the peak value. (b) Storage Modulus curves as a function of temperature (c) Comparison of T_g, rubbery modulus and glassy modulus as a function of mole content of glutaric anhydride linkers. Note: the glassy modulus is taken to be the initial value on the storage modulus curves as shown in Figure 3b 93
Figure 5.3. Schematic of the bond exchange reaction. (a) from left to right: before exchange, intermediate state and after exchange. (b) Structure change of the active groups during a bond exchange reaction. 94
Figure 5.4. The temperature dependent stress relaxation behavior of the epoxy soft network. Solid lines denote experimental results and dash lines show the prediction. The inset view shows the linear relationship between τ and 1000/T 95
Figure 5.5. (a) A master curve is constructed at the reference temperature of 160 ^oC. (b) Shift factors plotted as a function of temperature. Simulation curve are obtained based on Eq. 5-6. The slope determines the energy barrier for BERs. 97
Figure 5.6. The stress relaxation curves, master relxation curves and associated shift factors plots of (a) Epoxy 2, (b) Epoxy 3, (c) Epoxy 4 and (d) Epoxy 5. The stress relaxation behavior of Epoxy 1 is shown in Figure 1 99
Figure 5.7. Topological illustration of the epoxy network with different composition. (a) Schematic view of the repeating unit of the glutaric anhydride and C18 dicarboxylic acid. (b) Topological illustration of the epoxy network as gradually increasing the proportion of glutaric anhydride. 100
Figure 5.8. (a) The master relaxation curves in each epoxy sample. The reference temperature is uniformly chosen to be 160 ^oC. (b) The Arrhenius type shift factors plotted as a function of temperature. The energy barriers for the BERs in each epoxy sample are calculated based on the curve slopes. (c) Plot of the energy barrier for BERs and the difference between T_c and T_g as a function T_g. 101
Figure 5.9. The schematic graphs for a typical reprocessing and recycling routine..... 102

Figure 5.10. Analysis of particle sizes. (a) Microscopic observation of the isolated polymer particles. (b) Particle size and distribution analysis in Imagine J..... 103
Figure 5.11. Experimental setup for the reprocessing and recycling test of thermosetting polymer. (a) Aluminum punch mold. (b) Polymer Powder is placed into the mold. (c) The heating is conducted in a customized thermal chamber with pressure applied via the MTS machine. 104
Figure 5.12. The typical reprocessing and recycling routine for the thermosetting polymer and the stress-strain behavior after different reprocessing times. (a) A fresh bulk thermosetting polymer. (b) the typical reprocessing and recycling routine (180^{o}C in temperature and 45KPa in pressure). From left to right: pulverous polymer after milling, polymer powder after being heated for 10 min and 30min respectively. (c) Stress-strain curves of the reprocessed sample after being heated for different time and with 45 KPa pressure applied. Note: the fresh sample is also heated at 180 ^{o}C for 1h to normalize the comparison. Inset view: Stress-strain curves of powder sample without pressure applied. (d) Surface morphology of both fresh sample and powder samples at different heating time. 106
Figure 5.13. The time and pressure dependent ultimate stretch and initial modulus of the reprocessed thermosetting polymer (a) Ultimate stretch (maximum strain before fracture) plot of the reprocessed sample as a function of heating time. (b) Initial elastic modulus (within the first 15% stretch) as a function of heating time. (c) Ultimate stretch as a function of applied pressure. (d) Initial elastic modulus as a function of applied pressure. Note: R_f1 denotes the referencial property of a fresh bulk sample after being heating at 180 ^{o}C, while R_f 2 denotes that of the fresh sample without any heat treatment. 107
Figure 5.14. The recycling ability of the thermosetting polymer. (a) Top view: Sample manufactured by using polymer powder after being recycled for multiple times. Digit numbers indicate the recycle generation. Bottom view: the surface roughness observation on the 1st, 3rd and 4th recycled samples. (b). Stress-strain behavior of the polymer powder sample after being recycled for different times. The heating time is 30 min in each cycle. (c) Glass transtion behavior of the fresh sample and sample recycled for four times. (d) Ultimate stretch and initial elastic modulus plots as a function of recycle generations. Two sets of experiment are presented in the figure where the heating time in each reprocessing cycle is 30 min and 2 h respectively..... 109
Figure 5.15. Welding isolated bulk thermoset strip by using the pulverous polymer. (a) Two separated pieces of the thermosetting polymer are placed on a glass slide. (b) The gap is filled with the polymer powder. (c) The separated thermosetting polymer is healed and assembled together after being heated at 180^{o}C for 30min (45 KPa in pressure). (d) The sample is further trimmed into rectangular shape for tension test. (e) The stress-strain curves of the welded sample by using polymer powder recycled for different times. The heating time is 30 min in each test. (f) Ultimate stretch and initial elastic modulus plots as a function of recycle times of the applied polymer powder. Two sets of experiment are

presented in the figure where the heating time in each test is 30 min and 2 h respectively. 110
Figure 6.1. Interface morphology of two epoxy samples after being welded at 180 ^{o}C for 20min with 40 KPa applied..... 116
Figure 6.2.Mechanical properties of the welded epoxy sample. (a) Stress-strain curves of the thermosetting samples after being welded for different times. Inset view shows the appearance of the welded sample during experiment. The applied pressure is 40 KPa. (b) Initial elastic modulus (within the first 10% stretch) of welded sample with different pressure applied. The sample length is 6mm (c) Initial elastic modulus (within the first 10% stretch) of welded sample with different sample length. The applied pressure is 40 KPa. 117
Figure 6.3.Peeling force as a function of displacement after the epoxy sample being welded at 180 ^{o}C for 30min and 3h respectively. Inset view shows the sample appearance on the DMA machine during the T-peeling tests. 118
Figure 6.4.The proposed two dimensional (2D) squared lattice model to characterize interfacial kinetics. (a) The lattice geometry and (b) BER induced local chain redistribution between two neighboring lattice sides..... 119
Figure 6.5. Real contact area increases as the increment of processing time. 123
Figure 6.6. Normalized chain density evolution on the interface with different lattice size considered. 127
Figure 6.7**.** (a) Normalized chain density distribution within the lattice model at different timing point. The temperature is 180 ^{o}C. (b) Normalized chain density distribution at different heating time along the normal direction of the interface. The temperature is 180 ^{o}C..... 128
Figure 6.8. Both experimental results and theoretical predictions of the initial modulus of the welded epoxy sample. The welding temperature is 180 ^{o}C. (a) Initial modulus with different pressure applied. The sample length is 6mm. (b) Initial modulus with different sample length. The applied pressure is 40 KPa. 129
Figure 6.9. Both experimental results and theoretical predictions of the normalized interfacial fracture energy. The experimental results are plotted as dots. (a) Normalized interfacial fracture energy of epoxy samples after being welded at 180 ^{o}C for different time and with different pressure applied. (b) Normalized interfacial fracture energy of epoxy samples after being welded at 140 ^{o}C for different time and with different pressure applied..... 131
Figure 6.10. A master map for the prediction of effective modulus of the welded sample. The reference temperature for the reduced processing time is 160 ^{o}C 132
Figure 6.11. A master map for the prediction of interfacial fracture energy of the welded sample. The reference temperature for the reduced processing time is 160 ^{o}C..... 133

LIST OF ABBREVIATIONS AND SYMBOLS

The following table lists universal abbreviations and symbols used in this dissertation.

Abbreviations	
1D	One Dimensional
3D	Three Dimensional
ASTM	American Society for Testing and Materials
BER	Bond Exchange Reaction
CB	Carbon Black
CTE	Coefficient of Thermal Expansion
DGEBA	Diglycidyl Ether of Bisphenol
DMA	Dynamic Mechanical Analysis
DSC	Differential Scanning Calorimetry
FEM	Finite Element Method
FS Simulation	Fluid Structure Simulation
ID	Inner Diameter
MD	Molecular Dynamics
m-SME	Multi-Shape Memory Effect
MTS	Material Testing Machine
NLREG	Nonlinear Regression
OD	Outer Diameter
PEGDMA	Poly (ethylene glycol) Dimethacrylate
PTFE	Polytetrafluoroethylene
RVE	Representative Volume Element
SEM	Scanning Electron Microscope
SM	Shape Memory
SME	Shape Memory Effect
SMP	Shape Memory Polymer
tBA	Tert-butyl Acrylate
TME	Temperature Memory Effect
TTSP	Time Temperature Superposition Principle
UMAT	User Material Subroutine
WLF equation	Williams-Landel-Ferry Equation
Symbols	
E_a	Energy Barrier

E_l	Loss Modulus
E_s	Storage Modulus
k_b	Boltzman's Constant
R	Gas Constant
R_f	Shape Fixity
R_r	Shape Recovery Ratio
$tan\delta$	Ratio between Loss and Storage Modulus
T_d	Programming Temperature
T_g	Glassy Transition Temperature
T_L	Shape Fixing Temperature
T_M	WLF Reference Temperature
T_s	Crossing Point of Two Curves

CHAPTER 1

INTRODUCTION

1.1 Background

1.1.1 Overview

An active network polymer is known as a "smart" thermosetting polymer that can recognize a stimulus as a signal, judge the degree of this signal, and consequently change their conformation or properties as a direct response [1, 2]. It can be sensitive to a number of signals, such as heat [3-9], pH [10-15], light [16-22], chemical and ionic strength [23-26] etc., and respond in various ways, such as altering color, shape, modulus, conductivity and permeability[2, 27-29]. One of the most prominent features of the active network polymers is that a slight change in the environment is sufficient to induce rapid and large changes in the material's properties [29-32].

The sensitivity of these polymers is originated from various microscopic physical or chemical processes within the networks. If properly designed and utilized, these microscopic alternations could be beneficial in achieving polymer intelligence and multi-functionality. However, before an active polymer can be widely applied in the industrial, a comprehensive understanding of the material properties is essential. In this dissertation, we will focus on the properties of thermally induced active network polymers, and their thermomechanical behaviors are studied from both experimental and theoretical points of view. Specifically, two types of such active materials are selected, namely the shape memory polymers (SMPs) and covalent adaptive network (CANs) based on bond exchange reactions (BERs). While the shape memory effect in SMPs is considered to be a general feature of polymer materials, BERs in the CANs represent a novel chemistry of polymer engineering, which enables the reuse and recycle of thermosetting polymers.

1.1.2 Shape memory polymers

For SMPs, currently there are two physically processes can be utilized to achieve the shape memory effect. One is glass transition in amorphous polymer materials (see Figure 1.1a), where the polymer chain mobility will be dramatically changed upon changing the temperature. The spontaneous free shape recovery at high temperatures is attributed to

the tendency of network to increase the entropy until the crosslinking sites return to their original spatial positions [3, 33-37]. The other physical process for the shape memory effect is phase evolution in semi-crystalline polymer materials [38-45], where both crystalline region and amorphous region coexists, and acts as frozen phase and active phase respectively (see Figure 1.1b). Upon changing the temperature, different phases will be born at different times, and carry different stress and strain history. The main difference between the aforementioned two physically processes is that: in the glass transition, the shape memory effect is attributed to the temperature dependent mobility of polymer chains, while for the phase evolution, that is resulted from the temperature dependent volume fraction of different phases.

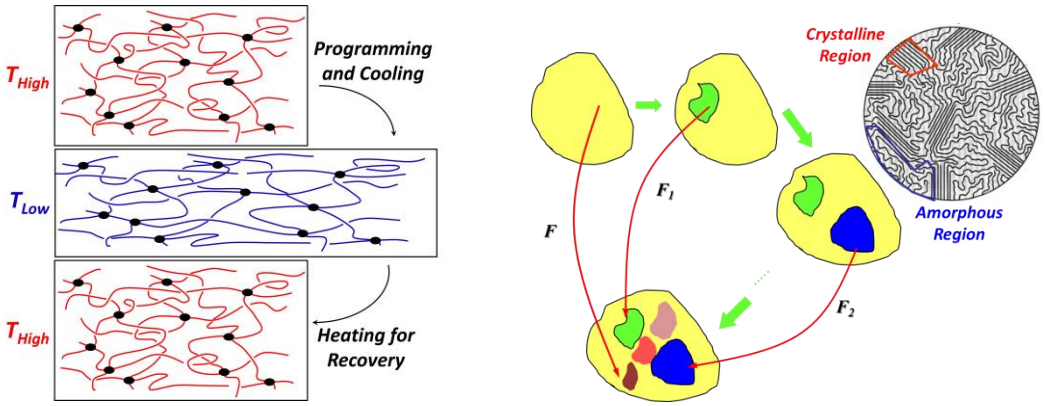

(a) (b)

Figure 1.1. Schematic views of (a) glass transition (modified according to [3]) and (b) phase evolution

For the thermally induced SMPs, the most convenient and straightforward actuation method is direct heating method (Figure 1.2a), where thermal energy is gradually transferred from the material surface to the inside. However, due to the low thermal conductivity of polymers, recovery rate of SMP is usually limited, especially when the SMP component is large. Recently, efforts have been made to improve the recovery rate of SMPs by using indirect heating methods. For example, after dispersing magnetic particles, the shape memory effect of SMPs can be realized by applying electromagnetic energy (Figure 1.2b) [46-49]. This approach offers the advantages of fast and remote heating. Similarly, SMP composites incorporated with conductive fillers (such as carbon fiber or particles) [50-55] or light absorbers [56] can be respectively activated by electricity (Figure 1.2c) or light (Figure 1.2d). A general feature of these actuation

methods is that the internal reinforcements convert other types of energy into thermal energy to volumetrically heat up the SMP matrix. In the contrast, water-driven SMPs [57-63] (Figure 1.2e) use different principle. When a deformed SMP is immersed into the solvent, the transition temperature will be decreased as solvent molecules diffusing into the polymer matrix. In this manner, the shape recovery can be induced at the room temperature. All these different actuation methods possess merits and can be used in different engineering applications.

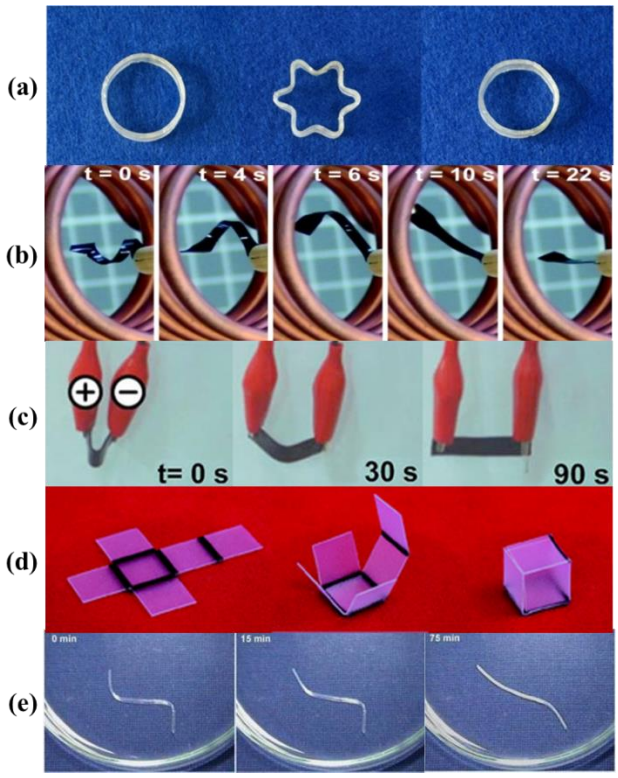

Figure 1.2. Typical actuation methods for the thermally sensitive SMPs. (a) Direct heating [64], (b) Magnetic actuation [48], (c) Electric actuation [54], (d) Infrared light actuation [56] and (e) Water actuation[59].

Since SMPs can sense the environmental changes and then take reactions in a predetermined sequence with deformation, they are considered as a promising alternative for the future's spontaneous shape changing and tunable components in various applications. Currently, the major applications of SMPs lie in the biomedical area. In 2002, Lendlein et al. [65] demonstrated that SMP could be used as self-tightening suture for minimum invasive surgery. The shape recovery of the suture can be triggered by human body heat, leading to the shrinkage of the suture (see Figure 1.3a) and the

tightening of the knot without external intervention. In another application, biocompatible SMPs are designed to be stent [66], which can be implanted into the human body with recovered configuration (see Figure 1.3b) sustaining the cardiovascular. In addition to biomedical applications, SMPs could also be used as functional materials, where they exhibit advantages in combining both shape changing and fixing capabilities, and hence can be applied in microelectromechanical systems, surface patterning control (Figure 1.3c), aerospace deployable and morphing structures [7, 27, 44, 66-71].

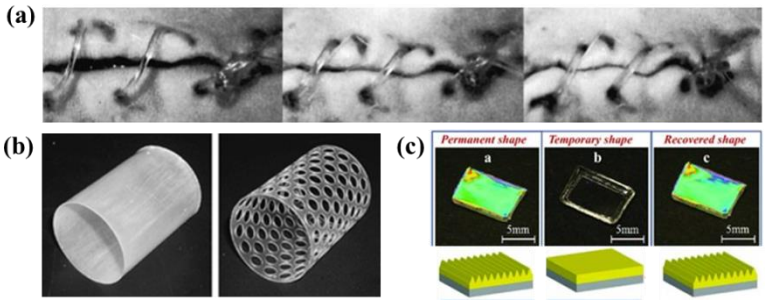

Figure 1.3. Typical applications of SMPs. (a) SMP suture [65], (b) SMP stent [66] and (c) SMP controlling the surface pattern [68]

During the applications, SMPs are typically operated in a shape memory cycle, where the material will be firstly deformed at the programming temperature T_d, followed by a specified holding time before being cooled to the shape-fixing temperature T_L. This finishes the programming step. In the recovery step, depending on whether or not the external force still exists, the SMPs will exhibit recovery stress or spontaneous free shape recovery upon increasing the recovery temperature T_r. Figure 1.4a illustrates a free shape memory cycle for the thermo-sensitive SMPs with uniaxial programming deformation. Two parameters are routinely adopted to characterize the material shape memory behavior, namely the shape fixity, which is calculated by the spring back deformation during the unloading step:

$$R_f = (e_{\max} - \Delta e)/e_{\max}\,, \tag{1-1a}$$

and the shape recovery ratio, which is based on the strain evolution in the recovery step and calculated as:

$$R_r = 1 - e(t)/(e_{\max} - \Delta e)\,. \tag{1-1b}$$

Figure 1.4b shows a typical free recovery curve as a function of time.

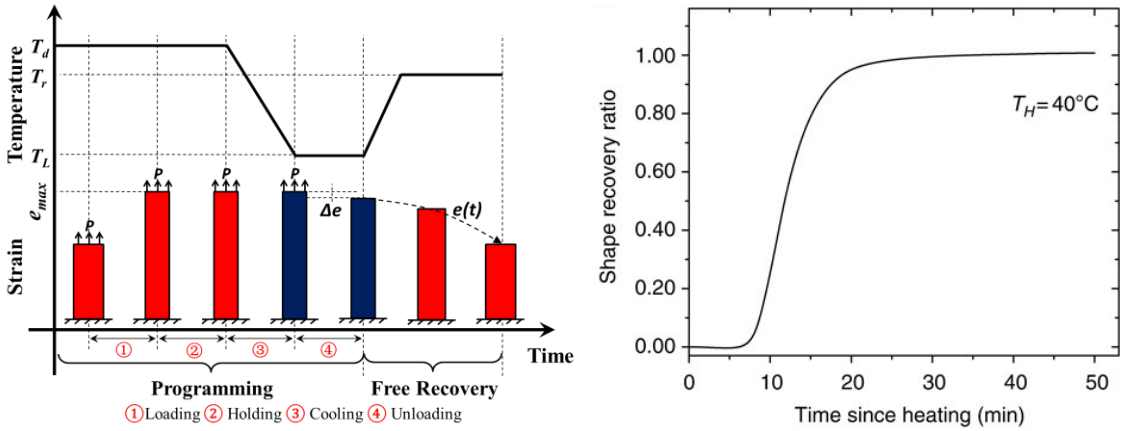

Figure 1.4. (a) A schematic illustration of the thermomechanical history of the programming and free recovery process in an SM cycle. (b) A typical free recovery curve as a function of time.

To achieve a higher shape fixity and recovery rate, thermosetting network polymers are typically preferred due to their superior thermomechanical and mechanical properties. Although a stable network enable excellent shape memory properties, the applications and service time of SMPs are limited by the material's mold-determined permanent shapes. In addition, once damaged or retired, it is hard to dispose the polymer wastes by using traditional methods, which typically relies on high heat or toxic chemicals and can lead to environmentally recycling difficulties and pollutions. From both environmental and economic point of view, we desire a new technology that can enable the healing of thermosets and repair their components in service to improve the sustainability, or reprocess and recycle the polymer into valuable resources without environmental impact.

1.1.3 Covalent adaptive network

The key of effective repair and recycle of thermosetting polymers is to design proper mechanisms to enable surface welding. Tremendous efforts were made in the past in this realm, such as surface interlocking [72, 73], inter-diffusion of network defects [74] and adding linear thermoplastic chains at the interface [75-77]. For more robust and efficient welding and reprocessing effect, various dynamic covalent chemistries have been utilized, where specific functional groups capable of reversible chemical reactions are integrated into the polymer chains [19, 78-90]. This new type of active network polymers is usually referred as covalent adaptive network (CAN) [81, 91], malleable thermosetting polymers [80, 92] or dynamic covalent bond network [86, 93] in different literatures. In this dissertation, we will refer it as covalent adaptive network

The functional groups in the CANs can break and reform the thermosetting network, and consequently render it adaptiveness upon stimuli. Figure 1.5 shows schematic view of the bond exchange reactions (BERs). When a proper stimulus is applied, an active group will move around within the free volume and approach another connected pair to form the intermediate state. During the reaction, the active group will kick off one unit in the connected pair and connect with another one to form a new connected pair of exchangeable bonds.

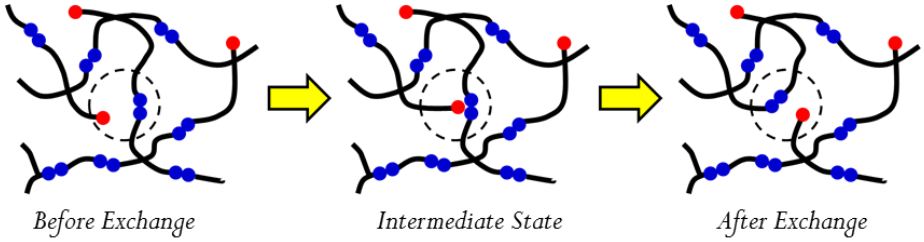

Figure 1.5. Schematic of bond exchange reactions (BERs)

When numerous BERs undergoing within the network, the network topology is expected to evolve with time, leading to the malleability of thermosetting polymers. As shown in Figure 1.6, the thermally induced BERs will release the internal stress of a deformed thermosetting polymer, which consequently retains the fusilli shape after unloading. Besides, polymer chains will be reconnected on the interface when desired polymer parts are brought into contact. Therefore, the CANs possess merits in combining the malleability of bulk material with the surface welding effect, leading to the self-healing [82, 92, 94-96], reprocessing (see Figure 1.7) and recycling of thermosetting polymers [80, 92, 97, 98]. Currently, various chemical reactions have been applied to achieve the dynamic bond exchanging. For example, the well-established Diels-Alder reaction [96, 99-101] between diene and dienophile groups can be thermally triggered, and displace the thermosetting polymer from equilibrium toward deploymerization upon heating. Recently, Montarnal et al [80] developed adaptive epoxy thermoset based on transesterfication exchange reactions at high temperature, which enables the topology rearrangement of network and avoids impairing the network integrity. Other covalent adaptive reactions in this realm include amino carbonyl reaction [95, 102, 103], siloxane

equilibration [78], and photo-sensitive radicals to initiate exchange reaction and malleability in thermosets [94, 104, 105].

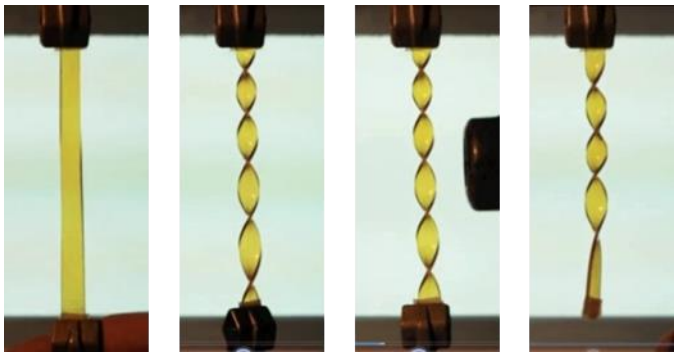

Figure 1.6. Stress relaxation in thermosetting polymers based on the BERs

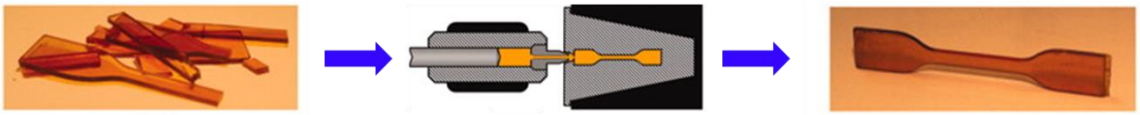

Figure 1.7. Reprocessing of broken epoxy active network polymer in an injection machine to recover its initial aspect [73]

1.2 Research Motivation and Goals

While both SMPs and CANs are currently under intensive investigations, there are still research challenges or unclear principles in our understanding before the materials can be widely applied in engineering applications. For example, although the basic concept of SMPs has been known for decades, recent advances have led to the discovery of previously uncovered properties [4, 5, 106-112]. First, experimental work revealed complicated dependency of the SM performance on thermo-temporal conditions in an SM cycle: the recovery of SMPs programmed under the same conditions strongly depends on the recovery temperature and heating rate in the recovery step [40, 111, 113-118]; in addition, the programming temperature has been shown to affect significantly the free recovery behavior for SMPs under the same thermo-temporal recovery conditions [5, 66, 107, 109, 119, 120]. To date, because the recovery behavior of an SMP depends on the aforementioned multiple thermo-temporal input parameters, there is no clear understanding how these input parameters can affect the SM performance individually or collectively. Such complicated dependency also hinders the development of SMP applications from the material and product design point of view. Second, some newly discovered shape memory effects, such as multiple and temperature memory effect are

challenging our previous understanding of this type of active network polymer. A comprehensive study on the thermomechanical and shape memory properties of SMPs is therefore necessary to explain these experimental observations, understand material behavior, and assist the design in engineering applications.

For the CANs, since the BERs represent a novel chemistry of polymer engineering, most investigations are focusing on the experimental area. For theoretical study, different molecular theories have been adopted, such as polymer sticky reputation theory [121], scaling theory [122] and particle patching [123]. Molecular dynamics (MD) method was also applied to explore the macromolecular details of CANs [124]. Despite of merits in all these models, molecular parameters are typically hard to be determined by using the standard polymer testing methods. Photo-induced BERs can be modeled as a phase evolution process where chain addition-fragmentation process was considered as a phase transformation between stressed phases and newly-born phases. Such a modeling scheme exhibits reasonable fidelity but is computationally expensive. Recently, within the scope of continuum mechanics, Long et al. [125] studied the mechanics of CANs with thermally induced Diels-Alder reactions. Long et al. [126] investigated the stress relaxation of epoxy thermoset with thermally induced bond exchange reactions (BERs). Ma et al [127] studied the time-dependent stress relaxation and photo-induced plastic deformation in a photoactivated CANs. However, for the surface welding effect of the CANs, to the best of our knowledge, little work has been conducted. To characterize the interfacial kinetics and mechanics, a concise modeling frame with fewer parameters that can be easily obtained based on the behavior of bulk material is highly desirable for the practical applications.

The overall objective of our study is to tackle the aforementioned research challenges and advance our understanding of the material behaviors through experimental and theoretical investigations. In particular, we will 1) reveal the underlying mechanism of several recently discovered SMEs by using the thermoviscoelastic constitutive model, 2) develop a unified method to predict the shape memory behavior of SMPs, 3) investigate the shape memory behaviors of SMP composites based on a 3D finite deformation constitutive model; 4) characterize the thermomechanical behaviors of CANs, and 5) develop a continuum level theoretical model to examine the interfacial mechanics of

CANs. Our research methods involve experimental testing on the material thermomechanical behaviors, and then develop constitutive models to describe the experimental observations, unravel the underlying mechanism and further assist the development and engineering application of the CANs.

1.3 Thesis Plan

This dissertation is arranged as the following: the thermomechanical and shape memory behaviors of amorphous thermo-sensitive SMPs will be investigated in Chapter 2-4. Chapter 5 and 6 will then present our studies on the CANs based on thermally induced BERs. Specifically, we will introduce the typical thermoviscoelastic modeling approaches for amorphous SMPs in Chapter 2. Then based on a one-dimensional (1D) multi-branched constitutive model, some new and interesting shape memory effects will be studied, such as multi-shape memory effect (m-SME), which help to advance our previous understanding of the material behaviors. In Chapter 3, we will present our unified method to predict the shape memory performance of thermo-rheologically simple SMPs under different thermo-temporal conditions. This unified method will be further applied to study the temperature memory effect (TME) in amorphous SMPs. In Chapter 4, we will extend the 1D thermoviscoelastic constitutive relations into three-dimensional (3D) finite deformation model, which is applied to investigate the thermomechanical and shape memory properties of two types of SMP composites that are respectively reinforced by magnetic parties and microvascular. Chapter 5 will present our experimental characterization results of the CANs, which will include the malleability, surface welding, reprocessing and recycling properties. Chapter 6 develops a continuum level theoretical model on the interfacial mechanics based on the BER kinetics. The developed mode possesses concise modeling frame and is effective in predicting the effective modulus and interfacial fracture energy of welded samples.

1.4 References

1. Kaneko, Y., et al., *Rapid deswelling response of poly(N-isopropylacrylamide) hydrogels by the formation of water release channels using poly(ethylene oxide) graft chains.* Macromolecules, 1998. **31**(18): p. 6099-6105.
2. Roy, I. and M.N. Gupta, *Smart polymeric materials: Emerging biochemical applications.* Chemistry & Biology, 2003. **10**(12): p. 1161-1171.

3. Lendlein, A. and S. Kelch, *Shape-memory polymers.* Angew Chem Int Ed Engl, 2002. **41**(12): p. 2035-57.
4. Yu, K., G. Qi, and H.J. Qi, *Reduced time as a unified parameter determining fixity and free recovery of shape memory polymers.* Nature communications, 2014. **5**: p. 3066.
5. Xie, T., *Tunable polymer multi-shape memory effect.* Nature, 2010. **464**(7286): p. 267-270.
6. Xie, T., *Recent advances in polymer shape memory.* Polymer, 2011. **52**(22): p. 4985-5000.
7. Lendlein, A. and S. Kelch, *Shape-memory polymers as stimuli-sensitive implant materials.* Clinical Hemorheology and Microcirculation, 2005. **32**(2): p. 105-116.
8. Gan, L.H., Y.Y. Gan, and G.R. Doon, *Poly(N-acryloyl-N '-propylpiperazine): A new stimuli-responsive polymer.* Macromolecules, 2000. **33**(21): p. 7893-7897.
9. Kurihara, S., Y. Ueno, and T. Nonaka, *Preparation of poly(vinyl alcohol) graft N-isopropylacrylamide copolymer membranes with triphenylmethane leucocyanide and permeation of solutes through the membranes.* Journal of Applied Polymer Science, 1998. **67**(11): p. 1931-1937.
10. Lim, Y.B., et al., *Biodegradable polyester, poly[alpha-(4 aminobutyl)-L-glycolic acid], as a non-toxic gene carrier.* Pharmaceutical Research, 2000. **17**(7): p. 811-816.
11. Lim, Y.B., Y.H. Choi, and J.S. Park, *A self-destroying polycationic polymer: Biodegradable poly(4-hydroxy-L-proline ester).* Journal of the American Chemical Society, 1999. **121**(24): p. 5633-5639.
12. Choi, Y.H., et al., *Characterization of a targeted gene carrier, lactose-polyethylene glycol-grafted poly-L-lysine, and its complex with plasmid DNA.* Human Gene Therapy, 1999. **10**(16): p. 2657-2665.
13. Murthy, N., et al., *The design and synthesis of polymers for eukaryotic membrane disruption.* Journal of Controlled Release, 1999. **61**(1-2): p. 137-143.
14. Luo, L.B., et al., *Stimuli-sensitive polymer gels that stiffen upon swelling.* Macromolecules, 2000. **33**(14): p. 4992-4994.
15. Sardar, M., et al., *Noncovalent immobilization of enzymes on an enteric polymer Eudragit S-100.* Enzyme and Microbial Technology, 1997. **20**(5): p. 361-367.
16. Irie, M. and D. Kunwatchakun, *Photoresponsive Polymers .8. Reversible Photostimulated Dilation of Polyacrylamide Gels Having Triphenylmethane Leuco Derivatives.* Macromolecules, 1986. **19**(10): p. 2476-2480.
17. Kippelen, B., et al., *Infrared photorefractive polymers and their applications for imaging.* Science, 1998. **279**(5347): p. 54-57.
18. Park, T.G. and A.S. Hoffman, *Thermal Cycling Effects on the Bioreactor Performances of Immobilized Beta-Galactosidase in Temperature-Sensitive Hydrogel Beads.* Enzyme and Microbial Technology, 1993. **15**(6): p. 476-482.
19. Scott, T.F., et al., *Photoinduced plasticity in cross-linked polymers.* Science, 2005. **308**(5728): p. 1615-1617.
20. Ryu, J., et al., *Photo-origami-Bending and folding polymers with light.* Applied Physics Letters, 2012. **100**(16).
21. Li, M.H., et al., *Light-driven side-on nematic elastomer actuators.* Advanced Materials, 2003. **15**(7-8): p. 569-572.

22. Lendlein, A., et al., *Light-induced shape-memory polymers.* Nature, 2005. **434**(7035): p. 879-882.
23. Ding, Z.L., G.H. Chen, and A.S. Hoffman, *Unusual properties of thermally sensitive oligomer-enzyme conjugates of poly(N-isopropylacrylamide)-trypsin.* Journal of Biomedical Materials Research, 1998. **39**(3): p. 498-505.
24. Thu, B., O. Smidsrod, and G. SkjakBraek, *Alginate gels - Some structure-function correlations relevant to their use as immobilization matrix for cells.* Immobilized Cells: Basics and Applications, 1996. **11**: p. 19-30.
25. Strand, B.L., Y.A. Morch, and G. Skjak-Braek, *Alginate as immobilization matrix for cells.* Minerva Biotecnologica, 2000. **12**(4): p. 223-233.
26. Song, S.C., et al., *A new class of biodegradable thermosensitive polymers. I. Synthesis and characterization of poly(organophosphazenes) with methoxy-poly(ethylene glycol) and amino acid esters as side groups.* Macromolecules, 1999. **32**(7): p. 2188-2193.
27. Sun, L., et al., *Stimulus-responsive shape memory materials: A review.* Materials & Design, 2012. **33**: p. 577-640.
28. Hoffman, A.S., et al., *Really smart bioconjugates of smart polymers and receptor proteins.* Journal of Biomedical Materials Research, 2000. **52**(4): p. 577-586.
29. Gil, E.S. and S.M. Hudson, *Stimuli-reponsive polymers and their bioconjugates.* Progress in Polymer Science, 2004. **29**(12): p. 1173-1222.
30. Galaev, I.Y. and B. Mattiasson, *'Smart' polymers and what they could do in biotechnology and medicine.* Trends in Biotechnology, 1999. **17**(8): p. 335-340.
31. Hoffman, A.S. and P.S. Stayton, *Bioconjugates of smart polymers and proteins: Synthesis and applications.* Macromolecular Symposia, 2004. **207**: p. 139-151.
32. Luzinov, I., S. Minko, and V.V. Tsukruk, *Adaptive and responsive surfaces through controlled reorganization of interfacial polymer layers.* Progress in Polymer Science, 2004. **29**(7): p. 635-698.
33. Behl, M., M.Y. Razzaq, and A. Lendlein, *Multifunctional Shape-Memory Polymers.* Advanced Materials, 2010. **22**(31): p. 3388-3410.
34. Behl, M., J. Zotzmann, and A. Lendlein, *Shape-Memory Polymers and Shape-Changing Polymers.* Shape-Memory Polymers, 2010. **226**: p. 1-40.
35. Mather, P.T., X.F. Luo, and I.A. Rousseau, *Shape Memory Polymer Research.* Annual Review of Materials Research, 2009. **39**: p. 445-471.
36. Ratna, D. and J. Karger-Kocsis, *Recent advances in shape memory polymers and composites: a review*. Journal of Materials Science, 2008. **43**(1): p. 254-269.
37. Rousseau, I.A., *Challenges of Shape Memory Polymers: A Review of the Progress Toward Overcoming SMP's Limitations.* Polymer Engineering and Science, 2008. **48**(11): p. 2075-2089.
38. Fulcher, G.S., *Analysis of recent measurements of the viscosity of glasses.* Journal of the American Ceramic Society, 1925. **8**(6): p. 339-355.
39. Fulcher, G.S., *Analysis of recent measurements of the viscosity of glasses. II.* Journal of the American Ceramic Society, 1925. **8**(12): p. 789-794.
40. Qi, H.J., et al., *Finite deformation thermo-mechanical behavior of thermally induced shape memory polymers.* Journal of the Mechanics and Physics of Solids, 2008. **56**(5): p. 1730-1751.

41. Volk, B.L., D.C. Lagoudas, and Y.C. Chen, *Analysis of the finite deformation response of shape memory polymers: II. 1D calibration and numerical implementation of a finite deformation, thermoelastic model.* Smart Materials & Structures, 2010. **19**(7).
42. Chen, Y.C. and D.C. Lagoudas, *A constitutive theory for shape memory polymers. Part I - Large deformations.* Journal of the Mechanics and Physics of Solids, 2008. **56**(5): p. 1752-1765.
43. Chen, Y.C. and D.C. Lagoudas, *A constitutive theory for shape memory polymers. Part II - A linearized model for small deformations.* Journal of the Mechanics and Physics of Solids, 2008. **56**(5): p. 1766-1778.
44. Liu, Y.P., et al., *Thermomechanics of shape memory polymers: Uniaxial experiments and constitutive modeling.* International Journal of Plasticity, 2006. **22**(2): p. 279-313.
45. Long, K.N., M.L. Dunn, and H.J. Qi, *Mechanics of soft active materials with phase evolution.* International Journal of Plasticity, 2010. **26**(4): p. 603-616.
46. Yu, K., et al., *Design considerations for shape memory polymer composites with magnetic particles.* Journal of Composite Materials, 2013. **47**(1): p. 51-63.
47. Buckley, P.R., et al., *Inductively heated shape memory polymer for the magnetic actuation of medical devices.* Ieee Transactions on Biomedical Engineering, 2006. **53**(10): p. 2075-2083.
48. Mohr, R., et al., *Initiation of shape-memory effect by inductive heating of magnetic nanoparticles in thermoplastic polymers.* Proceedings of the National Academy of Sciences of the United States of America, 2006. **103**(10): p. 3540-3545.
49. Weigel, T., R. Mohr, and A. Lendlein, *Investigation of parameters to achieve temperatures required to initiate the shape-memory effect of magnetic nanocomposites by inductive heating.* Smart Materials & Structures, 2009. **18**(2).
50. Leng, J.S., et al., *Conductive nanoparticles in electro activated shape memory polymer sensor and actuator.* Nanosensors and Microsensors for Bio-Systems 2008, 2008. **6931**.
51. Yu, K., Y.J. Liu, and J.S. Leng, *Conductive Shape Memory Polymer Composite Incorporated with Hybrid Fillers: Electrical, Mechanical, and Shape Memory Properties.* Journal of Intelligent Material Systems and Structures, 2011. **22**(4): p. 369-379.
52. Lv, H.B., J.S. Leng, and S.Y. Du, *Electro-induced shape-memory polymer nanocomposite containing conductive particles and short fibers.* Behavior and Mechanics of Multifunctional and Composite Materials 2008, 2008. **6929**.
53. Lu, H.B., et al., *Fabrication and properties of shape-memory polymer coated with conductive nanofiber paper.* Second International Conference on Smart Materials and Nanotechnology in Engineering, 2009. **7493**.
54. Leng, J.S., et al., *Significantly reducing electrical resistivity by forming conductive Ni chains in a polyurethane shape-memory polymer/carbon-black composite.* Applied Physics Letters, 2008. **92**(20).
55. Lu, H.B. and J.H. Gou, *Study on 3-D High Conductive Graphene Buckypaper for Electrical Actuation of Shape Memory Polymer.* Nanoscience and Nanotechnology Letters, 2012. **4**(12): p. 1155-1159.

56. Liu, Y., et al., *Self-folding of polymer sheets using local light absorption.* Soft Matter, 2012. **8**(6): p. 1764-1769.
57. Pierce, B.F., et al., *Demonstrating the influence of water on shape-memory polymer networks based on poly[(rac-lactide)-co-glycolide] segments in vitro.* International Journal of Artificial Organs, 2011. **34**(2): p. 172-179.
58. Xiao, R. and T.D. Nguyen, *Modeling the solvent-induced shape-memory behavior of glassy polymers.* Soft Matter, 2013. **9**(39): p. 9455-9464.
59. Huang, W.M., et al., *Water-driven programmable polyurethane shape memory polymer: Demonstration and mechanism.* Applied Physics Letters, 2005. **86**(11).
60. Huang, W.M., et al., *Water-responsive programmable shape memory polymer devices - art. no. 64231S.* International Conference on Smart Materials and Nanotechnology in Engineering, Pts 1-3, 2007. **6423**: p. S4231-S4231.
61. Kalita, H., M. Mandal, and N. Karak, *Biodegradable solvent-induced shape-memory hyperbranched polyurethane.* Journal of Polymer Research, 2012. **19**(10).
62. Lu, H.B., et al., *Qualitative separation of the effect of the solubility parameter on the recovery behavior of shape-memory polymer.* Smart Materials & Structures, 2009. **18**(8).
63. Lu, H.B., et al., *Qualitative separation of the physical swelling effect on the recovery behavior of shape memory polymer.* European Polymer Journal, 2010. **46**(9): p. 1908-1914.
64. Huang, W.M., et al., *Thermo/chemo-responsive shape memory effect in polymers: a sketch of working mechanisms, fundamentals and optimization.* Journal of Polymer Research, 2012. **19**(9).
65. Lendlein, A. and R. Langer, *Biodegradable, elastic shape-memory polymers for potential biomedical applications.* Science, 2002. **296**(5573): p. 1673-1676.
66. Yakacki, C.M., et al., *Unconstrained recovery characterization of shape-memory polymer networks for cardiovascular applications.* Biomaterials, 2007. **28**(14): p. 2255-2263.
67. Liu, Y.P., et al., *Thermomechanics of shape memory polymer nanocomposites.* Mechanics of Materials, 2004. **36**(10): p. 929-940.
68. Wang, Z., et al., *Programmable, Pattern-Memorizing Polymer Surface.* Advanced Materials, 2011. **23**(32): p. 3669-3673.
69. Sun, L., et al., *Wrinkling Atop Shape Memory Materials.* Surface Review and Letters, 2012. **19**(2).
70. Sun, L., et al., *Formation of Combined Surface Features of Protrusion Array and Wrinkles Atop Shape-Memory Polymer.* Surface Review and Letters, 2009. **16**(6): p. 929-933.
71. Francis W.H., et al., *Elastic Memory Composite Microbuckling Mechanics: Closed-Form Model with Empirical Correlation,* in *48th AIAA/ASME/ASCE/AHS/ASC Structures, Structural Dynamics, and Materials Conference*. 2007, AIAA 2007-2164: Honolulu, Hawaii.
72. Outwater, J.O. and D.J. Gerry, *On Fracture Energy, Rehealing Velocity and Refracture Energy of Cast Epoxy Resin.* Journal of Adhesion, 1969. **1**(Oct): p. 290-&.

73. Rahmathullah, M.A.M. and G.R. Palmese, *Crack-Healing Behavior of Epoxy-Amine Thermosets.* Journal of Applied Polymer Science, 2009. **113**(4): p. 2191-2201.
74. Yamaguchi, M., S. Ono, and M. Terano, *Self-repairing property of polymer network with dangling chains.* Materials Letters, 2007. **61**(6): p. 1396-1399.
75. Hayes, S.A., et al., *A self-healing thermosetting composite material.* Composites Part a-Applied Science and Manufacturing, 2007. **38**(4): p. 1116-1120.
76. Luo, X.F., et al., *A Thermoplastic/Thermoset Blend Exhibiting Thermal Mending and Reversible Adhesion.* Acs Applied Materials & Interfaces, 2009. **1**(3): p. 612-620.
77. Peterson, A.M., et al., *Investigation of interpenetrating polymer networks for self-healing applications.* Composites Science and Technology, 2012. **72**(2): p. 330-336.
78. Zheng, P.W. and T.J. McCarthy, *A Surprise from 1954: Siloxane Equilibration Is a Simple, Robust, and Obvious Polymer Self-Healing Mechanism.* Journal of the American Chemical Society, 2012. **134**(4): p. 2024-2027.
79. Capelot, M., et al., *Catalytic Control of the Vitrimer Glass Transition.* Acs Macro Letters, 2012. **1**(7): p. 789-792.
80. Montarnal, D., et al., *Silica-Like Malleable Materials from Permanent Organic Networks.* Science, 2011. **334**(6058): p. 965-968.
81. Kloxin, C.J., et al., *Covalent Adaptable Networks (CANS): A Unique Paradigm in Cross-Linked Polymers.* Macromolecules, 2010. **43**(6): p. 2643-2653.
82. Canadell, J., H. Goossens, and B. Klumperman, *Self-Healing Materials Based on Disulfide Links.* Macromolecules, 2011. **44**(8): p. 2536-2541.
83. Ghosh, B. and M.W. Urban, *Induced self-repairing oxetane-substituted chitosan polyurethane networks.* Abstracts of Papers of the American Chemical Society, 2009. **238**.
84. Ghosh, B. and M.W. Urban, *Self-Repairing Oxetane-Substituted Chitosan Polyurethane Networks.* Science, 2009. **323**(5920): p. 1458-1460.
85. Higaki, Y., H. Otsuka, and A. Takahara, *A thermodynamic polymer cross-linking system based on radically exchangeable covalent bonds.* Macromolecules, 2006. **39**(6): p. 2121-2125.
86. Maeda, T., H. Otsuka, and A. Takahara, *Dynamic covalent polymers: Reorganizable polymers with dynamic covalent bonds.* Progress in Polymer Science, 2009. **34**(7): p. 581-604.
87. Park, H.Y., et al., *Stress Relaxation by Addition-Fragmentation Chain Transfer in Highly Cross-Linked Thiol-Yne Networks.* Macromolecules, 2010. **43**(24): p. 10188-10190.
88. Rowan, S.J., et al., *Dynamic covalent chemistry.* Angewandte Chemie-International Edition, 2002. **41**(6): p. 898-952.
89. Wojtecki, R.J., M.A. Meador, and S.J. Rowan, *Using the dynamic bond to access macroscopically responsive structurally dynamic polymers.* Nature Materials, 2011. **10**(1): p. 14-27.
90. Taynton, P., et al., *Heat- or Water-Driven Malleability in a Highly Recyclable Covalent Network Polymer.* Advanced Materials, 2014. **26**(23): p. 3938-3942.

91. Bowman, C.N. and C.J. Kloxin, *Covalent Adaptable Networks: Reversible Bond Structures Incorporated in Polymer Networks.* Angewandte Chemie-International Edition, 2012. **51**(18): p. 4272-4274.
92. Capelot, M., et al., *Metal-Catalyzed Transesterification for Healing and Assembling of Thermosets.* Journal of the American Chemical Society, 2012. **134**(18): p. 7664-7667.
93. Jackson, A.W. and D.A. Fulton, *Making polymeric nanoparticles stimuli-responsive with dynamic covalent bonds.* Polymer Chemistry, 2013. **4**(1): p. 31-45.
94. Amamoto, Y., et al., *Repeatable Photoinduced Self-Healing of Covalently Cross-Linked Polymers through Reshuffling of Trithiocarbonate Units.* Angewandte Chemie, 2011. **123**(7): p. 1698-1701.
95. Deng, G.H., et al., *Covalent Cross-Linked Polymer Gels with Reversible Sol-Gel Transition and Self-Healing Properties.* Macromolecules, 2010. **43**(3): p. 1191-1194.
96. Zhang, Y., A.A. Broekhuis, and F. Picchioni, *Thermally Self-Healing Polymeric Materials: The Next Step to Recycling Thermoset Polymers?* Macromolecules, 2009. **42**(6): p. 1906-1912.
97. Yu, K., et al., *Influence of stoichiometry on the glass transition and bond exchange reactions in epoxy thermoset polymers.* Rsc Advances, 2014. **4**(89): p. 48682-48690.
98. Yu, K., et al., *Reprocessing and recycling of thermosetting polymers based on bond exchange reactions.* Rsc Advances, 2014. **4**(20): p. 10108-10117.
99. Chen, X.X., et al., *A thermally re-mendable cross-linked polymeric material.* Science, 2002. **295**(5560): p. 1698-1702.
100. Reutenauer, P., et al., *Room Temperature Dynamic Polymers Based on Diels–Alder Chemistry.* Chemistry – A European Journal, 2009. **15**(8): p. 1893-1900.
101. Adzima, B.J., et al., *Rheological and Chemical Analysis of Reverse Gelation in a Covalently Cross-Linked Diels−Alder Polymer Network.* Macromolecules, 2008. **41**(23): p. 9112-9117.
102. Lehn, J.M., *Dynamers: Dynamic Molecular and Supramolecular Polymers.* Australian Journal of Chemistry, 2010. **63**(4): p. 611-623.
103. Skene, W.G. and J.M.P. Lehn, *Dynamers: Polyacylhydrazone reversible covalent polymers, component exchange, and constitutional diversity.* Proceedings of the National Academy of Sciences of the United States of America, 2004. **101**(22): p. 8270-8275.
104. Nicolay, R., et al., *Responsive Gels Based on a Dynamic Covalent Trithiocarbonate Cross-Linker.* Macromolecules, 2010. **43**(9): p. 4355-4361.
105. Scott, T.F., R.B. Draughon, and C.N. Bowman, *Actuation in crosslinked polymers via photoinduced stress relaxation.* Advanced Materials, 2006. **18**(16): p. 2128-+.
106. Yu, K., et al., *Mechanisms of multi-shape memory effects and associated energy release in shape memory polymers.* Soft Matter, 2012. **8**(20): p. 5687-5695.
107. Xie, T., K.A. Page, and S.A. Eastman, *Strain-Based Temperature Memory Effect for Nafion and Its Molecular Origins.* Advanced Functional Materials, 2011. **21**(11): p. 2057-2066.

108. Xie, T., X.C. Xiao, and Y.T. Cheng, *Revealing Triple-Shape Memory Effect by Polymer Bilayers.* Macromolecular Rapid Communications, 2009. **30**(21): p. 1823-1827.
109. Miaudet, P., et al., *Shape and temperature memory of nanocomposites with broadened glass transition.* Science, 2007. **318**(5854): p. 1294-1296.
110. Chen, X. and T.D. Nguyen, *Influence of thermoviscoelastic properties and loading conditions on the recovery performance of shape memory polymers.* Mechanics of Materials, 2011. **43**(3): p. 127-138.
111. Castro, F., et al., *Time and Temperature Dependent Recovery of Epoxy-Based Shape Memory Polymers.* Journal of Engineering Materials and Technology-Transactions of the Asme, 2011. **133**(2).
112. Sun, L. and W.M. Huang, *Mechanisms of the multi-shape memory effect and temperature memory effect in shape memory polymers.* Soft Matter, 2010. **6**(18): p. 4403-4406.
113. Ge, Q., et al., *Prediction of Temperature Dependent Free Recovery Behaviors of Shape Memory Polymers.* Soft Matter, 2012. **8**: p. 11098–11105.
114. Ge, Q., et al., *Thermomechanical behavior of shape memory elastomeric composites.* Journal of the Mechanics and Physics of Solids, 2011. **60**(1): p. 67-83.
115. Westbrook, K.K., et al., *A 3D finite deformation constitutive model for amorphous shape memory polymers: A multi-branch modeling approach for nonequilibrium relaxation processes.* Mechanics of Materials, 2011. **43**(12): p. 853-869.
116. Westbrook, K.K., et al., *Improved testing system for thermomechanical experiments on polymers using uniaxial compression equipment.* Polymer Testing, 2010. **29**(4): p. 503-512.
117. Castro, F., et al., *Effects of thermal rates on the thermomechanical behaviors of amorphous shape memory polymers.* Mechanics of Time-Dependent Materials, 2010. **14**(3): p. 219-241.
118. Nguyen, T.D., et al., *A thermoviscoelastic model for amorphous shape memory polymers: Incorporating structural and stress relaxation.* Journal of the Mechanics and Physics of Solids, 2008. **56**(9): p. 2792-2814.
119. Cui, J., K. Kratz, and A. Lendlein, *Adjusting shape-memory properties of amorphous polyether urethanes and radio-opaque composites thereof by variation of physical parameters during programming.* Smart Materials & Structures, 2010. **19**(6).
120. Wong, Y.S. and S.S. Venkatraman, *Recovery as a measure of oriented crystalline structure in poly(L-lactide) used as shape memory polymer.* Acta Materialia, 2010. **58**(1): p. 49-58.
121. Leibler, L., M. Rubinstein, and R.H. Colby, *Dynamics of Reversible Networks.* Macromolecules, 1991. **24**(16): p. 4701-4707.
122. Stukalin, E.B., et al., *Self-Healing of Unentangled Polymer Networks with Reversible Bonds.* Macromolecules, 2013. **46**(18): p. 7525-7541.
123. Smallenburg, F., L. Leibler, and F. Sciortino, *Patchy Particle Model for Vitrimers.* Physical Review Letters, 2013. **111**(18).

124. Rottach, D.R., et al., *Molecular dynamics simulations of polymer networks undergoing sequential cross-linking and scission reactions.* Macromolecules, 2007. **40**(1): p. 131-139.
125. Long, K.N., *The mechanics of network polymers with thermally reversible linkages.* Journal of the Mechanics and Physics of Solids, 2014. **63**: p. 386-411.
126. Long, R., H.J. Qi, and M.L. Dunn, *Modeling the mechanics of covalently-adaptable polymer networks with temperature-dependent bond exchange reactions.* Soft Matter, 2013. **9**(15): p. 4083 - 4096.
127. Ma, J., et al., *A photoviscoplastic model for photoactivated covalent adaptive networks.* Journal of the Mechanics and Physics of Solids, 2014. **70**: p. 84-103.

CHAPTER 2

ONE-DIMENSIONAL CONSTITUTIVE MODELING OF SHAPE MEMORY POLYMERS

The shape memory polymers (SMPs) studied in this dissertation are amorphous network polymers, where the shape memory behavior is based on the thermally induced glass transition. In this chapter, the nature of glass transition will be firstly introduced, and then followed by the one-dimensional (1D) thermoviscoelastic modeling approach of SMPs. The 1D constitutive model is also applied to reveal the driven force and energy release mechanism during the shape recovery of SMPs by studying some new and interesting shape memory effects, such as multiple memory effect etc.

2.1 Glass Transition in Amorphous Polymers

The glass transition refers to a unique thermodynamic process of amorphous polymer materials where the macromolecules experience dramatic mobility change upon environmental temperature alteration. At a low temperature, the polymer atoms are fixed to points in an irregular space lattice and the macromolecule chains do not undergo significant translational displacements in response to external forces. Thus, the material demonstrates a high-elastic solid state. When the temperature is ramped to a certain degree, sufficient thermal energy is transferred into the kinetic energy of polymer chains to allow changes in the conformation at a microscopic level. The material is then gradually converted to a low-elastic rubbery state featuring macromolecule chains sliding past each other in compliance with the macroscopic deformation. Glass transition occurs in a range of temperature and is usually experimentally characterized by the temperature changes of certain physical properties of the polymers, such as differential scanning calorimetry (DSC), thermomechanical analysis (TMA) and dynamic mechanical analysis (DMA). Specially, a glassy transition temperature (T_g), which is dependent on the polymer chemical composition and structure, thermal history and testing methods, is graphically determined on curves to distinguish the glassy and rubbery behavior of a

polymer material. Besides, since there is no latent heat involved in the glass transition process, the temperature of the polymer material is continuously increased as the material is heated, and hence this transition is called a second order transition.

The glassy transition could be utilized to achieve spontaneous shape recovery of a polymer material, namely the thermally induced shape memory behavior. To achieve large recoverable shape changes, crosslinked polymers are preferred as the crosslinks can retain the original permanent shape. At temperatures above T_g, SMPs lie in a rubbery state. Deforming the material would reduce the possible configurations of polymer chains and hence decrease the system configurational entropy, leading to the well-known entropic behavior of elastomers. After unloading, the tendency of SMPs to increase the entropy would lead to spontaneous shape recovery until the crosslinking sites within the material return to their original spatial positions. However, in some occasions, the SMPs are required to fix the temporary deformed shapes by lowering the temperature below T_g and then release them later on demand. There, the material is transformed into a glassy state and the mobility of macromolecular chains is significantly reduced by the reduction in free volume. Consequently, most deformation of SMPs incurred at the rubbery state is frozen. The shape memory effect would be invoked as further increasing the temperature above T_g, where the individual macromolecular chains become active again and the shape recovery mechanism described above is permitted.

2.2 1D Constitutive Modeling based on Thermoviscoelasticity

Since the inherent complexity of the thermally triggered glass transition and polymer SM effects that involving multiple shape changing events and different application purposes, theoretical models are desired to predict the behaviors for the targeted design. The early modeling efforts for the most commonly used thermally induced SMPs were one-dimensional, small strain, rheological models which could capture the characteristic SM behavior but with limited prediction capability due to the loss of the strain storage and release mechanisms. In these studies, the temperature dependent material viscosity is described by using an Arrhenius or Williams-Landel-Ferry (WLF) equation. Recently, the phase evolution modeling approach was proposed and considered to be an effective tool to explain some thermomechanical properties of SMPs [1-8]. This concept can be

applied to a wide variety of SMP materials, such as crystallizable [2, 6, 8, 9] or photo-activated [5, 10-13] SMPs, but it fails to physically relate the polymer glass transition behavior to their SM effect. In this regards, thermoviscoelastic modeling approaches [14-20] have emerged for the modeling of SMPs in which the mobility of polymer chains can be correlated with viscosity or relaxation time of a Maxwell element. The viscous strain developed at temperature above T_g is restricted at temperature below T_g (temporary shape fixing)[20]. Reheating to above T_g will reduce the viscosity, reactive the dashpot and allows the structure to relax to its equilibrium configuration, which leads to shape recovery.

With the modeling concept of glass transition, more comprehensive three-dimensional thermoviscoelastic models have been developed [14-17] with the merits in capturing various polymer behaviors in addition to the SM effect, such as finite-deformation, entropic elasticity of the rubbery network, nonlinear thermal expansion, structural relaxation and viscoplastic flow below T_g. However, for a real polymer system, multiple relaxation processes are involved as the temperature crosses T_g. Some polymers even demonstrate unique glass transition behaviors, such as perfluorosulphonic acid ionomer (PFSA) with a wide glass transition temperature range from 55 ^{o}C to 130 ^{o}C, and the Verflex E epoxy polymer showing two peaks on its tan δ curve. In these cases, the traditional modeling approach with single Maxwell element seems to be insufficient. In order to describe the material glass transition behaviors in real thermally triggered SMPs, two modeling strategies can be applied. The first one is based on a modified standard linear solid (SLS) model with Kohlrausch-Williams-Watts (KWW) stretched exponential function, where the regular material relaxation is mapped into a new timing space in describing the material clock. Previous modeling efforts in this realm are still limited within one dimensional (1D) small deformation of SMPs. In the second modeling strategy, the multi-branch models that resembling the 1D generalized viscoelastic model or Prony series are applied [21]. Based on this modeling frame, three dimensional (3D) model is constructed that considers finite deformation stress-strain behaviors (including yielding, post-yielding, and rate dependency), constrained recovery behaviors and free recovery behaviors. In this chapter, we will focus on the 1D constitutive model while the 3D finite deformation model will be introduced in Chapter 4.

The 1D rheological representation of the multi-branch model is shown in Figure 2.1, where an equilibrium branch and several nonequilibrium branches placed in parallel. The equilibrium branch is a linear spring with a Young's modulus of E_{eq} to represent the equilibrium behavior, and the nonequilibrium branches are Maxwell elements where an elastic spring and a dashpot are placed in series to represent the viscoelastic response. These nonequilibrium branches represent different relaxation processes (or modes) in the polymer system. In the *i-th* (*i* varies from 1 to *n*) nonequilibrium branch, the Young's modulus of the spring is denoted as E_i, and the corresponding stress relaxation time of the dashpot is denoted as τ_i.

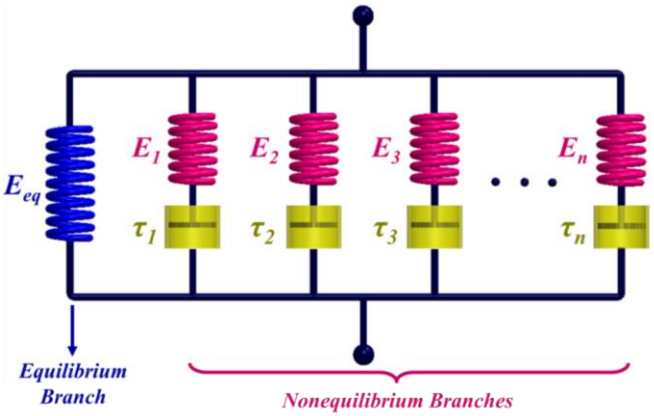

Figure 2.1. 1D rheological representation of the developed model

By using the Boltzmann's superposition principle [22], the total stress is given by

$$\sigma(t) = E_{eq}e(t) + \sum_{i=1}^{n} E_i \int_0^t \frac{de(s)}{dt} \exp\left(-\frac{t-s}{\tau_i(T)}\right) ds, \tag{2-1}$$

where $\sigma(t)$ and $e(t)$ are the total stress and strain of the multi-branched model. In Eq. 2-1, the relaxation times in individual branches vary as the temperature changes. Here, it is assumed that the time-temperature shift for each branch follows the same rule. According to the well-established "thermorheological simplicity" principle [47],

$$\tau_i(T) = \tau_0^i \alpha_T(T), \tag{2-2}$$

where $\alpha_T(T)$ is the time-temperature superposition shift factor, and τ_0^i is the reference relaxation time at the temperature when $\alpha_T(T) = 1$.

Following O'Connell and McKenna [48], the method for calculating the temperature influence on the viscoelastic behavior depends on whether the material temperature is

above or below a temperature T_s. At temperatures above T_s, the Williams-Landel-Ferry (WLF) Equation [49] is used

$$\log \alpha_T(T) = -\frac{C_1(T - T_M)}{C_2 + (T - T_M)}, \tag{2-3a}$$

where log is the base 10 logarithm, C_1 and C_2 are material constants and T_M is the WLF reference temperature. For temperature below T_s, $\alpha_T(T)$ follows the Arrhenius-Type behavior [50]:

$$\ln \alpha_T(T) = -\frac{AF_c}{k_b}\left(\frac{1}{T} - \frac{1}{T_g}\right), \tag{2-3b}$$

where A and F_c are material constants, k_b is Boltzman's constant. T_s is the crossing point of two curves representing Eqs.2-3a and 2-3b on a α_T vs T plot.

Eq. 2-1 was solved under the imposed mechanical conditions in a shape memory cycle. During the free recovery, since there was no force applied to the sample, the total stress was zero. Eq. 2-1 was solved for e(t) with the left hand side of the equation being zero. In all these cases, elastic strain e_i^e and viscous strain e_i^v (the strain in the dashpot) in individual nonequilibrium branches were given as

$$e_i^e = \int_0^t \frac{de(s)}{dt} \exp\left(-\frac{t-s}{\tau_i(T)}\right) ds, \; e_i^v = e - e_i^e. \tag{2-4}$$

The elastic energy stored in individual branches were calculated as

$$U_i = \frac{1}{2} E_i \left(e_i^e\right)^2. \tag{2-5}$$

2.3 Material Parameters Identification

The material parameters for the multi-branched model can be determined by using standard polymer tests. Here, we demonstrate the typical parameters identification method for an acrylate-based network polymer. Its liquid monomer tert-butyl acrylate (tBA), liquid cross-linker poly (ethylene glycol) dimethacrylate (PEGDMA) and the photo polymerization initiator (2, 2-dimethoxy-2-phenylacetophenone) in powder form were ordered from Aldrich and used in their as received conditions without any further purification. The synthesis procedure of the SMP followed Yakacki et al [23] by mixing

the tBA monomer, cross-linker and photo polymerization initiator with a weight ratio of 4000:1000:1, and the solution was then exposed in a UV irradiation for 10 min before the final heat treatment at 90 ℃ for 1 hour to assist the complete conversion of monomers.

There are two groups of material parameters need to be identified, namely the parameters for the TTSP (in Eq. 2-3) and the elastic modulus and relaxation time in each nonquilirbium branch. The TTSP parameters can be determined by the stress relaxation behavior of acrylate SMP material at different temperatures. In each relaxation test, the rectangular SMP specimen was firstly preloaded by 1×10^{-3} N force to maintain the straightness. After reaching the testing temperature, it was allowed 30 min for the thermal equilibrium. The specimen was stretched by 1% on the DMA machine and the deformation was maintained during the entire test (30 minutes). The decrease of stress was recorded and the stress relaxation modulus was calculated as shown in Figure 2.2a. Then selecting 27.5 ^{o}C as a reference temperature (T_s), each modulus curve in Figure 2.2a is shifted horizontally to superimpose with the next. This produces the master curve shown in Figure 2.2b, which spans many decades of modulus (from 1436 MPa to 3.05 MPa) and represents the actual relaxation behavior of the acrylate SMPs within a long time scale (around 20 years) at 27.5 ^{o}C. When shifting the curves in Figure 2.2a, the shifting factors are termed as α_T and plotted as a function of temperature in Figure 2.2c. By fitting with the experimentally tested shift factors, the parameters for both Arrhenius and WLF equations are determined as: $C_1 = 17.44$, $C_2 = 51.6℃$ and $AF_c k_B^{-1} = -40000\text{K}$.

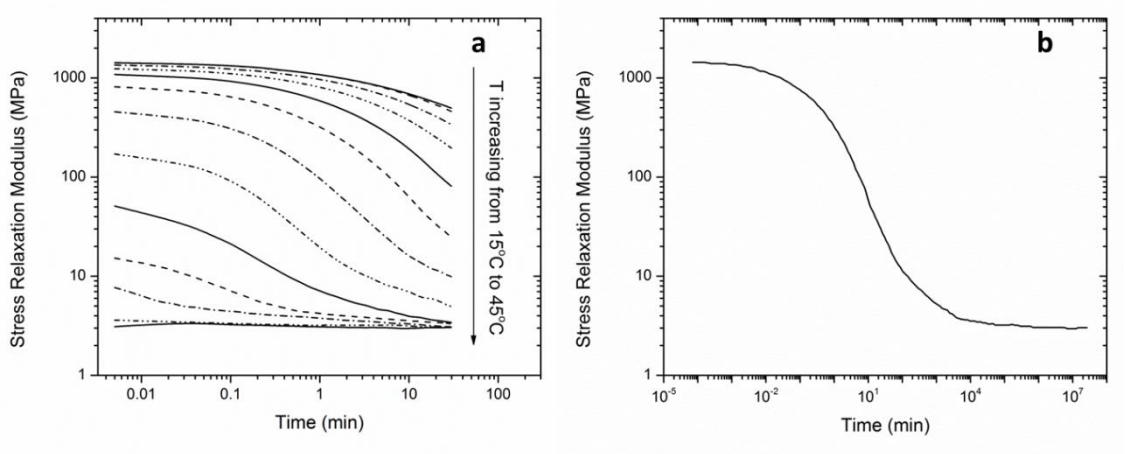

(a) (b)

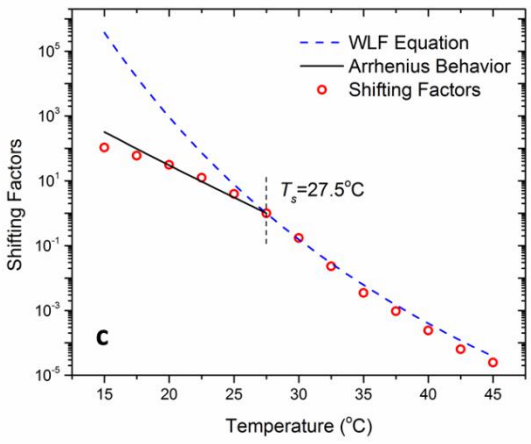

(c)

Figure 2.2. Stress relaxation tests and shifting factors: (a) Stress relaxation tests at temperatures increasing from 15 ℃ to 45 ℃ with 2.5 ℃ interval. (b) The stress relaxation master curve at 27.5 ℃. (c) Shifting factors at different temperatures

The elastic modulus and relaxation time in each nonequilibrium branch can be determined based on the tan δ and storage modulus of the SMP obtained in the DMA tests. For the 1D multi-branch linear model, the temperature dependent storage modulus $E_s(T)$, loss modulus $E_l(T)$ and $\tan\delta(T)$ are respectively expressed as:

$$E_s(T) = E_{eq} + \sum_{i=1}^{n} \frac{E_i w^2 (\tau_i(T))^2}{1 + w^2 (\tau_i(T))^2}, \tag{2-6a}$$

$$E_l(T) = \sum_{i=1}^{n} \frac{E_i w \tau_i(T)}{1 + w^2 (\tau_i(T))^2}, \tag{2-6b}$$

$$\tan\delta(T) = \frac{E_l(T)}{E_s(T)}, \tag{2-6c}$$

where w is the testing frequency, $\tau^i(T)$ is the temperature dependent relaxation time in each nonequilibrium branch. By using nonlinear regression (NLREG) method [24, 25], the initial modulus and relaxation time (at T_s) in each branch were estimated by fitting the model prediction with the experimental results. As shown in Figure 2.3, the identified parameters could enable the multi-branch model to successfully capture the experimental storage modulus and tanδ curves within the entire testing temperature range (5^o C-95^o C). The final set of model parameters are listed in Table 1.

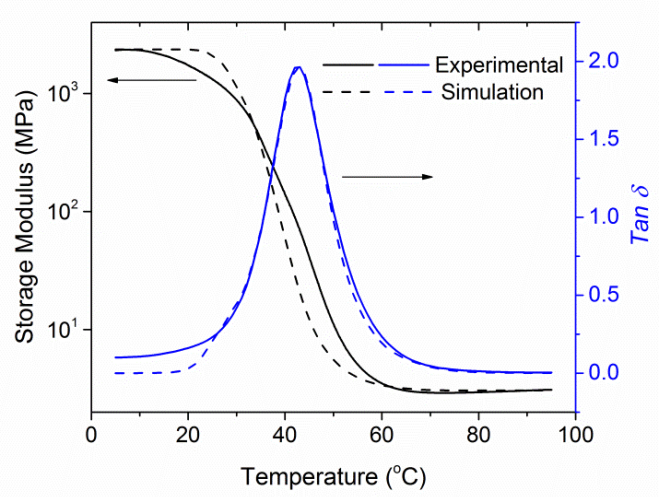

Figure 2.3. 1D estimation for the DMA result of SMP by using NLREG software. The original experimental curves are shown in solid lines

Table 2-1. Parameters of the multi-branched constitutive model

Parameters	***Values***	***Parameters***	***Values***
C_1	16.44	C_2	51.6 °C
$AF_c k_b^{-1}$	-40000 K	T_g	42.7 °C
T_s	27.5 °C	T_M	30 °C
E_{eq}	3.05 MPa		
E_i	(618.45, 440, 330, 38, 4, 2, 0.5) MPa for $i \in [1,7]$		
τ_i^0	(2, 20, 200, 2000, 20000, 200000, 2000000) s, or $3.33\times(10^{-2}, 10^{-1}, 10^{0}, 10^{1}, 10^{2}, 10^{3}, 10^{4})$ min for $i \in [1,7]$		

2.4 Predictions on the Shape Fixity and Recovery

After determining the model parameters, the 1D multi-branched model is applied to predict the shape fixity and recovery ratios of the acrylate SMPs. Following the schematic view of Figure 1.4a, we define a representative shape memory cycle as the following: In the programming step, the SMP is stretched to a target strain $e_{\max}$ (20%) with a constant loading rate (0.01 s^{-1}) at the programming temperature T_d, followed by a specified holding time at T_d before being cooled to the shape fixing temperature T_L (20 °C) at a rate of q (2.5 °C min^{-1}). Once T_L is reached, the specimen is held for 1 hour and then the tensile force is removed. In the free recovery step, the temperature is increased to the

recovery temperature T_r at the same rate of cooling and subsequently stabilized for another 50 min. The corresponding shape fixity and recovery ratio is calculated by using Eqs. 1-1a and 1-1b.

As shown in Figure 2.4, the model predictions adequately capture the shape fixity as a function of programing temperature and holding time, as well as the shape recovery ratio as a function of recovery temperature and heating time.

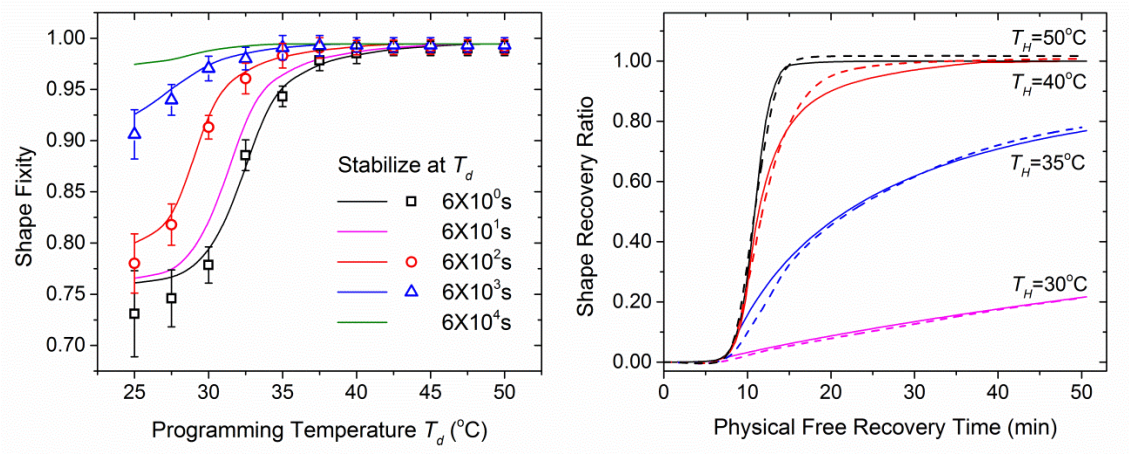

(a) (b)

Figure 2.4. Predictions on the experimentally tested shape fixity and recovery. (a) Shape fixity. Dot data indicates experimental results. (b) Shape recovery ratio. Solid lines indicate experimental results.

2.5 Influence of Stretch Induced Softening Effect on the Free Recovery Behavior

In addition to predict the shape memory behavior, the 1D constitutive model is also applied to study some new and interesting shape memory effects, which helps to reveal the secrets behind the shape memory effect, such as the driven force and energy releasing mechanism, and advances our previous understanding of this material.

In this section, the model is firstly applied to study the influence of stretch induced softening effect on the free recovery behavior of SMP composite incorporate with carbon black (CB). Such softening effect is generally experienced during cyclic loading of hydrostatic tensions [26, 27], equi-biaxial tensions [28-31], uniaxial compressions [32, 33] or simple shears [28, 34, 35], where the elastomeric materials exhibit more compliant stress-strain behavior before reaching the previous maximum strain. In our study, the matrix material is still the aforementioned acrylate SMP. The spherical CB particles with

a diameter of 50 nm (Sigma Aldrich, St. Louis, MO) were used in their as received conditions without any further purification.

As shown in Figure 2.5a, the stress-strain behavior of the SMP composites with 9 wt% CB tends to be stable after a few cycles (typically N=4), with most softening occurred during the first cycle. As the reloading curves approaching the maximum strain encountered in prior cycles, the stress tends to rejoin the stress level of that in the first cycle test. However, all the unloading paths after the 10% strain follow the same curve. As a result, the residual strain after each tension cycle is also independent of the cycle number.

Another feature of the softening effect is that a larger strain will lead to a larger degree of softening. To demonstrate how such different softening degrees affect the free recovery behavior, two SMP/CB samples were subjected to free shape memory cycle, where the programming strain is set to be 10% and 20% respectively. Other procedures are identical. A detailed experimental procedure can be found in our previous work[36].

Figure 2.5b shows the shape recovery ratio of the SMP composite as a function of heating time. The time for a full shape recovery was taken to be when the shape recovery ratio reaches 95%. It is seen that the sample pre-stretched by 20% shows an obvious delay (360s) for a full shape recovery compared with that of the 10% pre-stretched sample. Such decrease in the shape recovery speed is considered as impairment in the recovery ability of the material, and could be explained by the greater softening in this sample given by a larger prior stretching in the programming step.

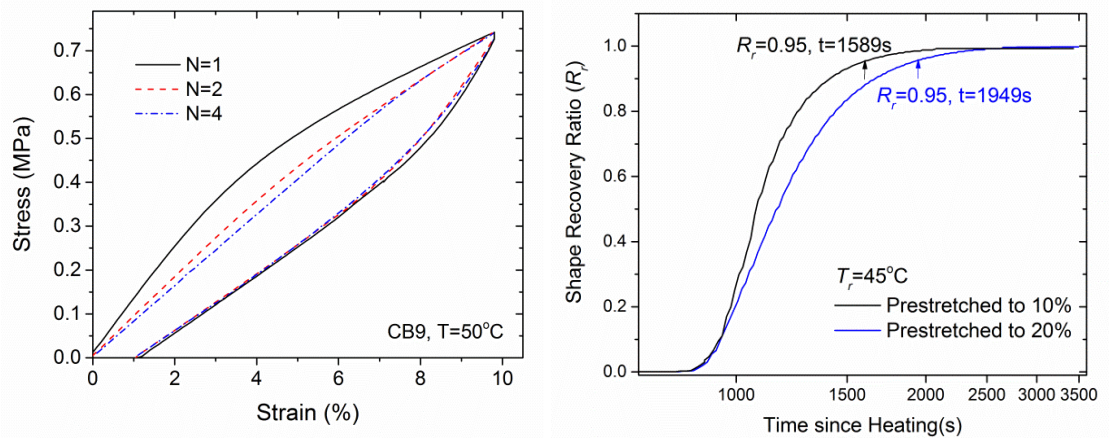

(a) (b)

Figure 2.5. Stretch induced softening effect in SMP composite and its influence on the free recovery behavior. (a) Cyclic tension tests on SMP composites with 9 wt% CB. The strain

amplitude is fixed amplitude at 10%. (n) Shape recovery ratio plot as a function of heating. Two samples were pre-stretched to 10% and 20% respectively during the programming step

As shown in Qi and Boyce[37], the stretched softening is mainly attributed to the softening in the equilibrium path, the modulus evolution in the equilibrium branch is modeled based on the detailed physical mechanism. For the polymer composites, researchers believe that by incorporating stiffer fillers into the elastomers, some rubber-filler attachments would be generated [38-40], and subsequently confine the entropy deformation of materials. While an external load is applied, the softening effect is produced due to the strain-induced relative motion or even micro-damage of local separation between the fillers and elastomer chains [41-44]. Following Holzapfel [45] for the modeling of material damage , the evolution of modulus in the equilibrium branch can be defined to be a function of a reduction factor $(1-\xi)$,

$$E_{eq}(t) = (1-\xi)E_{eq}^{0}, \tag{2-7}$$

where E_{eq}^{0} is the equilibrium modulus of the virgin material, $\xi \in [0,1]$ is a scalar and referred to as the softening variable, and is defined as a damage-like function $\xi = \xi(\varepsilon_{\max})$ with conditions of $\xi(0) = 0$ and $\xi(\infty) \in [0,1]$.

$$\xi = \xi(\lambda_{\max}) = \xi_{\infty}\left(1-\exp(-\frac{\varepsilon_{\max}}{\iota})\right), \tag{2-8}$$

where $\varepsilon_{\max}$ denotes the maximum strain of material encountered during its previous loading history, ξ_{∞} describes the dimensionless maximum softening and ι is referred to as the softening saturation parameter. According to Eq. 2-8, for a given unloading process, as well as a loading process before the strain ε exceeds $\varepsilon_{\max}$, the softening variable remains its value attained at $\varepsilon_{\max}$ encountered in the loading history. When $\varepsilon \geq \varepsilon_{\max}$, ξ is modeled to increase with increasing $\varepsilon_{\max}$, which is updated by $\varepsilon_{\max} = \varepsilon$. The parameters for the damage evolution were determined by fitting the stress-strain curves show in Figure 2.5a.

The rest model parameters were determined by following the procedure in Section 2.3. Both the prediction and experimental data of the time-dependent shape recovery ratio are plotted in Figure 2.6. For the simulation case of 20% pre-stretch, the increase in the total shape recovery time is resulted from the more significant reduction in the equilibrium

modulus, which is providing the driven force for the shape recovery of SMPs. In comparison with the experimental results, the numerical simulations fit for the shape recovery ratio curves well and provide a good prediction for softening resulted impartation on the shape recovery ability of SMP composite.

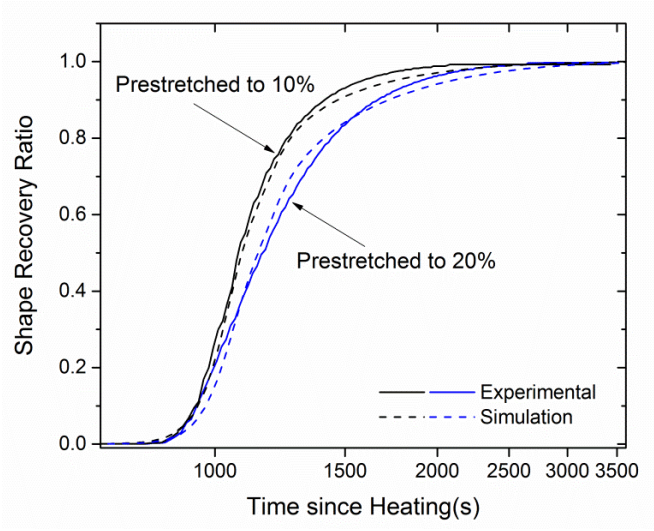

Figure 2.6. Shape recovery ratio plot as a function of heating time during the free recovery of CB9 SMP composites. Solid lines denote experimental results and dash line denotes corresponding simulations.

The effect of stretch induced softening effect to the free recovery behavior of SMP composites can also be explained from a physical point of view. As mentioned before, the shape memory effect in SMP is caused by the transition of polymer from a state dominated by internal energy to a state dominated by entropic energy as the temperature increasing. At temperatures above the glassy transition temperature T_g, macromolecular chains possess large mobility and random conformational changes. Stretching the material would lead long macromolecular chains to align, reduce the possible configurations and hence decrease the configuration entropy of macromolecular chains. After the removal of the mechanical load, the material tends to regain the lost entropy during the programming step and recover the original shape if such motion is not limited by the mobility of macromolecular chains. In this manner, the shape recovery speed could be evaluated by the entropy increasing rate within the material. From a molecular viewpoint, the cross-linking network and CB-polymer chain bonding serve as constraints within the SMP/CB composite, give rise to the elastic modulus and resist the macroscopic deformation before the macromolecular chains reaching their stretching limit. Vice versa,

these two effects would also be responsible for the spontaneous entropy increase during the free recovery of SMP composite. As revealed in the above cyclic tension tests, the interaction between CB and polymer chains is weakened in a manner that comply the internal macromolecular rearrangement during stretching, and such weakness is deemed to be irreversible within the time scale concerned in this study. Therefore, the entropy increase during the free recovery is slowed and the shape recovery speed is decreased, especially in the SMP composite with larger pre-stretch.

2.6 Multi-shape Memory Effect and Associated Energy Releasing Mechanism

In the multi-shape memory effect (m-SME), the SMPs could memorize more than one temporary shape in a single shape memory cycle. Technically speaking, such m-SME could be observed in any polymer system with a broad thermomechanical transition temperature range. When the stepped heating method is applied during the recovery step, shape recovery and energy release will occur in a stepped manner which enables the stepped recovery behavior. In this section, we use the 1D multi-branched model to study the polymer m-SME, which helps to reveal the underling associated energy release mechanism during the shape recovery of SMPs.

The experimental resulted used for this study was presented by Xie[46]. The material tested is the perfluorosulphonic acid ionomer (PFSA), which is a thermo-sensitive SMP with a broad thermal transition temperature range from 55 ^{o}C to 130 ^{o}C. During the shape memory cycle for m-SME, The material is first stretched (stress=0.65 MPa) at a deformation temperature of 140 ^{o}C. This stress is maintained constant during subsequent cooling at a rate of 5 ^{o}C/min. The stress is removed ten minutes after the temperature reaches 20 ^{o}C. The SMP is further equilibrated for 10 min. Afterwards, the SMP is heated under a stress free condition following a multistage heating procedure. In each stage, the temperature is ramped to a recovery temperature (T_r) and held constant for 40 min before the next heating process starts. Five recovery temperatures are set as: T_{r1} = 60 ^{o}C, T_{r2} = 80 ^{o}C, T_{r3} = 100 ^{o}C, T_{r4} = 120 ^{o}C, T_{r5} = 140 ^{o}C, and the heating rate is 5 ^{o}C/min.

A detailed description of model parameters identification can be found in our previous work[47]. Figure 2.7 shows the comparison between model predictions and experimental results. It is clear that the simulation predicts the experimental results very

well, indicating the model is able to capture m-SME.

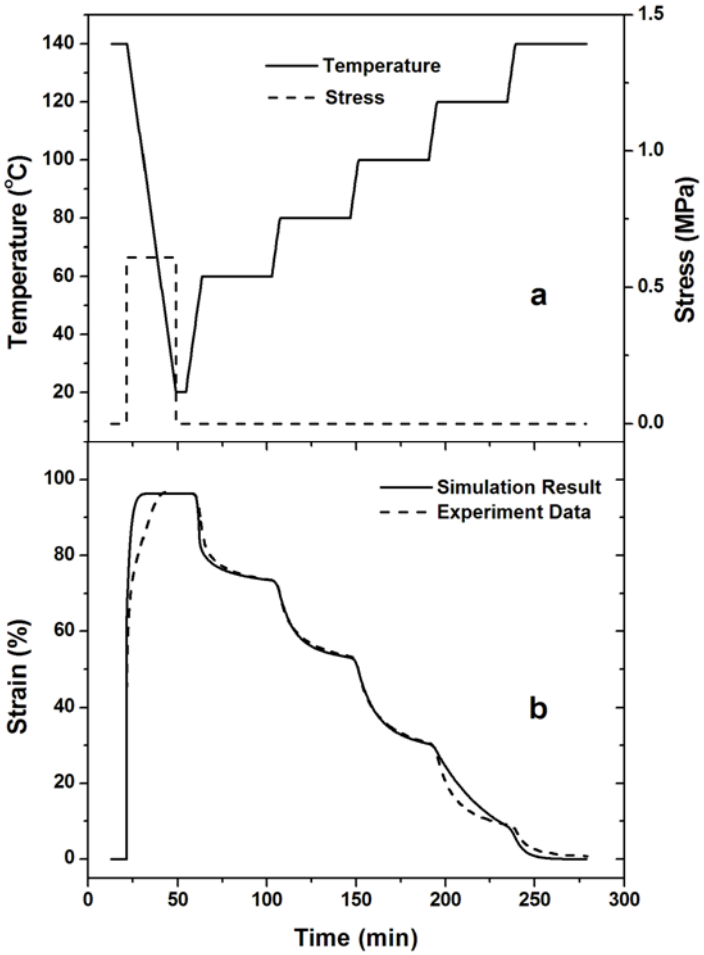

Figure 2.7. Multi-SME simulated under stress controlled programming and staged heating recovery conditions. (a) temperature and stress history. (b) strain evolution in both simulation and experiment.

Figure 2.8a shows the relaxation of viscous strains in the rubbery branches during the free recovery process. The staged heating leads to a staggered release of viscous strains stored in the dashpots and thus a staggered recovery. This is because the number of active dashpots varies at different recovery temperatures. Table 2-2 lists the relaxation times of the individual dashpots in the rubbery branches at different temperatures. The so called SM active or inactive corresponds to whether or not the branch can develop viscous strain. Therefore, it should be taken in a relative manner depending on the experimental time scale. Here, for the purpose of easy discussion, we use ~10^2 min relaxation time as the criterion for SM active or inactive. In Table 2-2, the SM inactive branches are marked with gray shadows. Based on this criterion, at the first staged temperature of 60 ^{o}C, only

3 rubbery branches are active. At the second staged temperature of 80 ^{o}C, the number of active rubbery branches increases to 5, causing more recovery. At the final temperature of 140 ^{o}C, all the rubbery branches become active, leading to a full recovery of the SMP.

Table 2-2. Relaxation times (in minutes) of individual rubbery branches at different temperatures

T	1	2	3	4	5	6	7
20 °C	3.28×10^{440}	3.28×10^{441}	3.28×10^{442}	3.28×10^{443}	3.28×10^{444}	3.28×10^{445}	3.28×10^{446}
60 °C	6.45×10^{-1}	6.45×10^{0}	6.45×10^{1}	6.45×10^{2}	6.45×10^{3}	6.45×10^{4}	6.45×10^{5}
80 °C	4.35×10^{-3}	4.35×10^{-2}	4.35×10^{-1}	4.35×10^{0}	4.35×10^{1}	4.35×10^{2}	4.35×10^{3}
100 °C	1.52×10^{-4}	1.52×10^{-3}	1.52×10^{-2}	1.52×10^{-1}	1.52×10^{0}	1.52×10^{1}	1.52×10^{2}
120 °C	1.37×10^{-5}	1.37×10^{-4}	1.37×10^{-3}	1.37×10^{-2}	1.37×10^{-1}	1.37×10^{0}	1.37×10^{1}
140 °C	2.24×10^{-6}	2.24×10^{-5}	2.24×10^{-4}	2.24×10^{-3}	2.24×10^{-2}	2.24×10^{-1}	2.24×10^{0}

Figure 2.8b shows the storage and release of elastic energy during the entire shape memory cycle. For the individual rubbery branches, the energy is stored in tensile strains before heating starts. Instead of being released directly, the energy increases first, is stored in compressive strains, and then gradually released. Therefore, before the stored elastic energy being released, significant energy transfer among different rubbery branches occurs. The similarity in the energy transfer and release during the recovery of dual-SME, triple-SME, and m-SME is expected. The difference among these three SMEs is the different heating schemes used during free recovery that can only pause the recovery and therefore energy transfer and release.

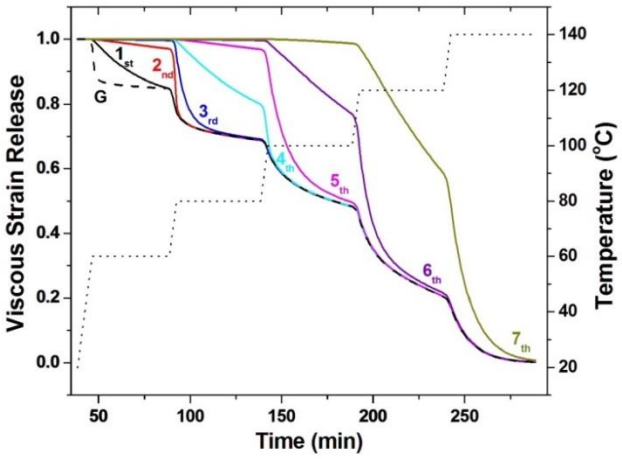

(a)

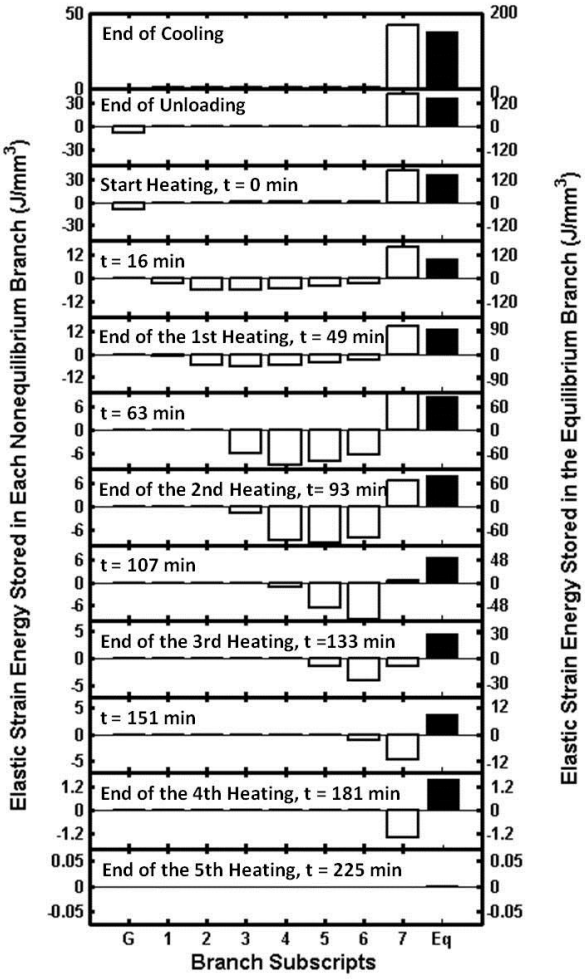

(b)

Figure 2.8. (a) Strain evolution of dashpots in each rubbery nonequilibrium branch during the free recovery process of multi-SME simulation. Key: solid line, normalized strain release; dotted line, temperature. (b) Elastic strain energy stored in each rubbery branch

2.7 Conclusion

In this chapter, we firstly introduced existing thermoviscoelastic modeling approaches for amorphous SMPs, where the shape memory effect is based on the thermally induced glass transition. Then the developed parameter identification method for the multi-branched constitutive model is presented, which enables the model to adequately capture the glass transition and shape memory behaviors. The multi-branched constitutive model is further applied to study some new and interesting shape memory effects, which helps to reveal the secrets behind the polymer shape memory effect, such as the driven force and energy releasing mechanism. Specifically, by studying the influence of stretch induced softening effect, we demonstrated that the material equilibrium modulus provides the driven force to the shape recovery of SMPs. If there is softening effect involved during the programming step, shape recovery speed will be decreased under a given thermal condition. Such a decrease in recovery rate is more obvious when a higher programming strain is applied. The energy releasing mechanism during the shape recovery of SMPs was revealed by investigating the multi-shape memory effect (m-SME). Our study suggests that the m-SME arises from the shifting of individual nonequilibrium branches (or relaxation modes) between a SM active state and a SM inactive state at different programming and recovery temperatures. Due to the complex molecular relaxation, the strain energy stored during shape fixing and released during recovery depends on the deformation temperature, holding time, and cooling time. During free recovery, the stored stress in the individual nonequilibrium branches first reverses its state (for example, from tensile to compression) before it declines to zero.

2.8 References

1. Chen, Y.C. and D.C. Lagoudas, *A constitutive theory for shape memory polymers. Part I-Large deformations.* Journal of the Mechanics and Physics of Solids, 2008. **56**(5): p. 1752-1765.
2. Barot, G., I.J. Rao, and K.R. Rajagopal, *A thermodynamic framework for the modeling of crystallizable shape memory polymers.* International Journal of Engineering Science, 2008. **46**(4): p. 325-351.
3. Liu, Y.P., et al., *Thermomechanics of shape memory polymers: Uniaxial experiments and constitutive modeling.* International Journal of Plasticity, 2006. **22**(2): p. 279-313.

4. Qi, H.J., et al., *Finite deformation thermo-mechanical behavior of thermally induced shape memory polymers.* Journal of the Mechanics and Physics of Solids, 2008. **56**(5): p. 1730-1751.
5. Long, K.N., et al., *Photomechanics of light-activated polymers.* Journal of the Mechanics and Physics of Solids, 2009. **57**(7): p. 1103-1121.
6. Ge, Q., et al., *Thermomechanical behavior of shape memory elastomeric composites.* Journal of the Mechanics and Physics of Solids, 2011. **60**(1): p. 67-83.
7. Long, K.N., M.L. Dunn, and H.J. Qi, *Mechanics of soft active materials with phase evolution.* International Journal of Plasticity, 2010. **26**(4): p. 603-616.
8. Westbrook, K.K., et al., *Constitutive Modeling of Shape Memory Effects in Semicrystalline Polymers With Stretch Induced Crystallization.* Journal of Engineering Materials and Technology-Transactions of the Asme, 2010. **132**(4): p. -.
9. Westbrook, K.K., et al., *Two-Way Reversible Shape Memory Effects in a Free-Standing Polymer Composite.* Smart Material and Structures, 2011. **20**: p. 065010.
10. Jennie Ryu, et al., *Photo-Origami.* Applied Physics Letter, 2012. **100**(161908).
11. Long, K.N., M.L. Dunn, and H.J. Qi, *Photo-Induced Deformation of Active Polymer Films: Single Spot Irradiation.* Int. J. Solids and Struc., 2011. **48**: p. 2089-2101.
12. Long, K.N., et al., *Light-Induced Stress Relief to Improve Flaw Tolerance in Network Polymers.* Journal of Applied Physics, 2010. **107**(053519).
13. Long, K.N., et al., *Photo-Induced Creep of Network Polymers.* International Journal of Structural Changes in Solids, 2010. **2**: p. 41-52.
14. Westbrook, K.K., et al., *A 3D finite deformation constitutive model for amorphous shape memory polymers: A multi-branch modeling approach for nonequilibrium relaxation processes.* Mechanics of Materials, 2011. **43**(12): p. 853-869.
15. Diani, J., Y.P. Liu, and K. Gall, *Finite Strain 3D Thermoviscoelastic Constitutive Model for Shape Memory Polymers.* Polymer Engineering & Science, 2006. 46(4): p. 486-492.
16. Nguyen, T.D., et al., *A thermoviscoelastic model for amorphous shape memory polymers: Incorporating structural and stress relaxation* Journal of the Mechanics and Physics of Solids, 2008. **56** (9): p. 2792-2814
17. Srivastava, V., S.A. Chester, and L. Anand, *Thermally actuated shape-memory polymers: Experiments, theory, and numerical simulations.* Journal of the Mechanics and Physics of Solids, 2010. **58**(8): p. 1100-1124.
18. Castro, F., et al., *Effects of thermal rates on the thermomechanical behaviors of amorphous shape memory polymers.* Mechanics of Time-Dependent Materials, 2010. **14**(3): p. 219-241.
19. Ge, Q., et al., *Prediction of temperature-dependent free recovery behaviors of amorphous shape memory polymers.* Soft Matter, 2012. **8**(43): p. 11098-11105.
20. Yu, K., et al., *Mechanisms of multi-shape memory effects and associated energy release in shape memory polymers.* Soft Matter, 2012. **8**(20): p. 5687-5695.
21. Engels, T.A.P., et al., *Predicting the Long-Term Mechanical Performance of Polycarbonate from Thermal History during Injection Molding.* Macromolecular Materials and Engineering, 2009. **294**(12): p. 829-838.

22. Rubinstein, M. and R.H. Colby, *Polymer physics*. 2003, New York: Oxford University Press, Oxford.
23. Yakacki, C.M., et al., *Unconstrained recovery characterization of shape-memory polymer networks for cardiovascular applications.* Biomaterials, 2007. **28**(14): p. 2255-2263.
24. Diani, J., et al., *Predicting thermal shape memory of crosslinked polymer networks from linear viscoelasticity* International Journal of Solids and Structure, 2012. **49**(5): p. 793-799.
25. Sherrod, P.H. *Nonlinear Regression Analysis Program, NLREG Version 5.0*. 2000; Available from: http://www.nlreg.com/.
26. Dorfmann, A., *Stress softening of elastomers in hydrostatic tension.* Acta Mechanica, 2003. **165**(3): p. 117-137.
27. Julie, D., F. Bruno, and G. Pierre, *A review on the Mullins effect.* European Polymer Journal, 2009. **45**(3): p. 601-612.
28. Mars, W.V. and A. Fatemi, *Observations of the Constitutive Response and Characterization of Filled Natural Rubber Under Monotonic and Cyclic Multiaxial Stress States.* Journal of Engineering Materials and Technology, 2004. **126**(1): p. 19-28.
29. Németh, I., et al. *On the modelling of amplitude and frequency-dependent properties in rubberlike solids*. in *constitutive models for rubber IV*. 2005. Balkema.
30. Mark, A.J. and F.B. Millard, *The Mullins effect in equibiaxial extension and its influence on the inflation of a balloon.* International Journal of Engineering Science, 1995. **33**(2): p. 223-245.
31. Li, J., D. Mayau, and V. Lagarrigue, *A constitutive model dealing with damage due to cavity growth and the Mullins effect in rubber like materials under triaxial loading.* Journal of the Mechanics and Physics of Solids, 2008. **56**(3): p. 953-973.
32. Bergström, J.S. and M.C. Boyce, *Constitutive modelling of the large strain time-dependent behavior of elastomers.* Journal of the Mechanics and Physics of Solids, 1998. **46**(5): p. 931-954.
33. Amin, A.F.M.S., M.S. Alam, and Y. Okui, *An improved hyperelasticity relation in modelling viscoelasticity response of natural and high damping rubbers in compression: experiments, parameter identification and numerical verification.* Mechanics of Materials, 2002. **34**(2): p. 75-95.
34. Ernst, L.J. and E.G. Septanika. *A non-Gaussian network alteration model*. in *Proceedings of the First European Conference on Constitutive Models for Rubber*. 1999.
35. Sedlan, K., *Viskoelastic Materialverhalten von Elastomerwerkstoffen: Experimentelle Untersuchung und Modellbildung. Ph.D. Dissertation*. 2000, University of Kassel.
36. Yu, K., Q. Ge, and H.J. Qi, *Effects of stretch induced softening to the free recovery behavior of shape memory polymer composites.* Polymer, 2014. **55**(23): p. 5938-5947.
37. Qi, H.J. and M.C. Boyce, *Stress-strain behavior of thermoplastic polyurethanes.* Mechanics of Materials, 2005. **37**(8): p. 817-839.

38. Blanchard, A.F. and D. Parkinson, *Breakage of Carbon-Rubber Networks by Applied Stress.* Ind. Eng. Chem., 1952. **44**(4): p. 799-812.
39. Bueche, F., *Molecular basis for the mullins effect.* Journal of Applied Polymer Science, 1960. **4**(10): p. 107-114.
40. Bueche, F., *Mullins effect and rubber-filler interaction.* Journal of Applied Polymer Science, 1961. **5**(15): p. 271-281.
41. Dannenberg, E.M., *The effects of surface chemical interactions on the properties of filler-reinforced rubbers.* Rubber Chem. Technol., 1974. **48**(1974): p. 410-444.
42. Rigbi, Z., *Reinforcement of rubber by carbon black.* Chemistry and Materials Science, 1980. **36**: p. 21-68.
43. Govindjee, S. and J. Simo, *A micro-mechanically based continuum damage model for carbon black-filled rubbers incorporating Mullins' effect.* J. Mech. Phys. Solids, 1991. **39**: p. 87-112.
44. Govindjee, S. and J. Simo, *Transition from micro-mechanics to computationally efficient phenomenology: carbon black filled rubbers incorporating Mullins effect.* J. Mech. Phys. Solids, 1992. **40**: p. 213-233.
45. Holzapfel, G.A., *Nonlinear solid mechanics: a continuum approach for engineering*. 2000, New York: Wiley, Chichester.
46. Xie, T., *Tunable polymer multi-shape memory effect.* Nature, 2010. **464**(7286): p. 267-270.
47. Yu, K., et al., *Mechanisms of multi-shape memory effects and associated energy release in shape memory polymers* Soft Matter, 2012. **8**(20): p. 5687-5695.

CHAPTER 3

A UNIFIED METHOD TO PREDICT SHAPE FIXITY AND RECOVERY OF SHAPE MEMORY POLYMERS

The performance of SMPs is typically quantified by the shape fixity, shape recovery rate and ratio etc. [1-11]. Previous experimental work revealed complicated dependency of the SM performance on thermo-temporal conditions in an SM cycle. For example, the recovery of SMPs programmed under the same conditions strongly depends on the recovery temperature and heating rate in the recovery step [4, 7-13]. On the other hand, the programming temperature has been shown to affect significantly the free recovery behavior for SMPs under the same thermo-temporal recovery conditions [14-19]. To date, because the recovery behavior of an SMP depends on the aforementioned multiple thermo-temporal input parameters, there is no clear understanding how these input parameters can affect the shape memory performance individually or in group. Such complicated dependency also hinders the development of SMP applications from the material and product design point of view. In this chapter, we will unravel the complicated dependency of SM performance on thermo-temporal conditions, and presents our unified method to predict both shape fixity and recovery of amorphous SMPs. Subsequently, this unified method is applied to reveal the underlying mechanism of another recently discovery shape memory effect, i.e. temperature memory effect (TME).

3.1 Experimental Observations on Shape Fixity and Recovery

We start our discussion by experimentally testing the influence of thermo-temporal conditions on the shape fixity and recovery. The typical shape memory cycle is still following the schematic shown in Figure 1.4a: In the programming step, the SMP is stretched to a target strain $e_{\max}$ (20%) with a constant loading rate $\dot{e}$ (0.01/s) at the programming temperature T_d, followed by a specified holding time at T_d before being cooled to the shape fixing temperature T_L (20^{o}C) at a rate of q (2.5 ℃/min). Once T_L is

reached, the specimen is held for 1 hour then the tensile force is removed. In the free recovery step, the temperature is increased to the recovery temperature T_r at the same rate of cooling, and subsequently stabilized for another 50 minutes.

Several groups of experiments were firstly conducted to impress the dependency of shape fixity and recovery on the programming and recovery conditions. In the first experimental investigation, the SMP specimens were respectively programmed at 11 different temperatures (T_d is evenly distributed from 25^{o}C to 50^{o}C) and recovered at 40^{o}C (T_r=40^{o}C). The shape fixities and the shape recovery times corresponding to the 95% shape recovery ratio ($t_{0.95}$) are plotted as a function of programming temperature in Figure 3.1a. The measured shape recovery ratio is plotted as a function of heating time in Figure 3.1b. In a typical SM cycle, a lower programming temperature has two effects: On the one hand, it results in a faster shape recovery rate. This phenomenon is referred as temperature memory effect of SMPs under free recovery condition [17, 19, 20]. On the other hand, however, it leads to a lower shape fixity, indicating that a large portion of the programmed deformation is recovered right after unloading. Such a sudden spring back at low programming temperatures would cause some instabilities for the length measurement in the adopt machine (DMA, TA Instruments, Model Q800), which subsequently results in the elevated experimental uncertainties as shown in Figure 3.1a.

The influence of recovery condition on the free shape recovery behavior of SMPs was evaluated by selecting different recovery temperatures (T_r=30 °C, 35 ℃, 40 ℃ and 50 ℃ respectively, Figure 3.1c) in the free recovery SM cycle. In these tests, the programming conditions were set identical with T_d=40 ℃ and holding time of 6×10^2s, which leads to a shape fixity of 98.7%. As shown in Figure 3.1c, the recovery rate is faster at higher recovery temperatures. Note that for recovery temperatures greater than the glass transition temperature (T_g) of SMPs (42.7 ^{o}C), the final shape recovery ratio is seen to be slightly larger than 100%. This is due to the thermal expansion for recovery temperatures greater than programming temperatures. The thermal expansion effect would be neglected in the following discussions.

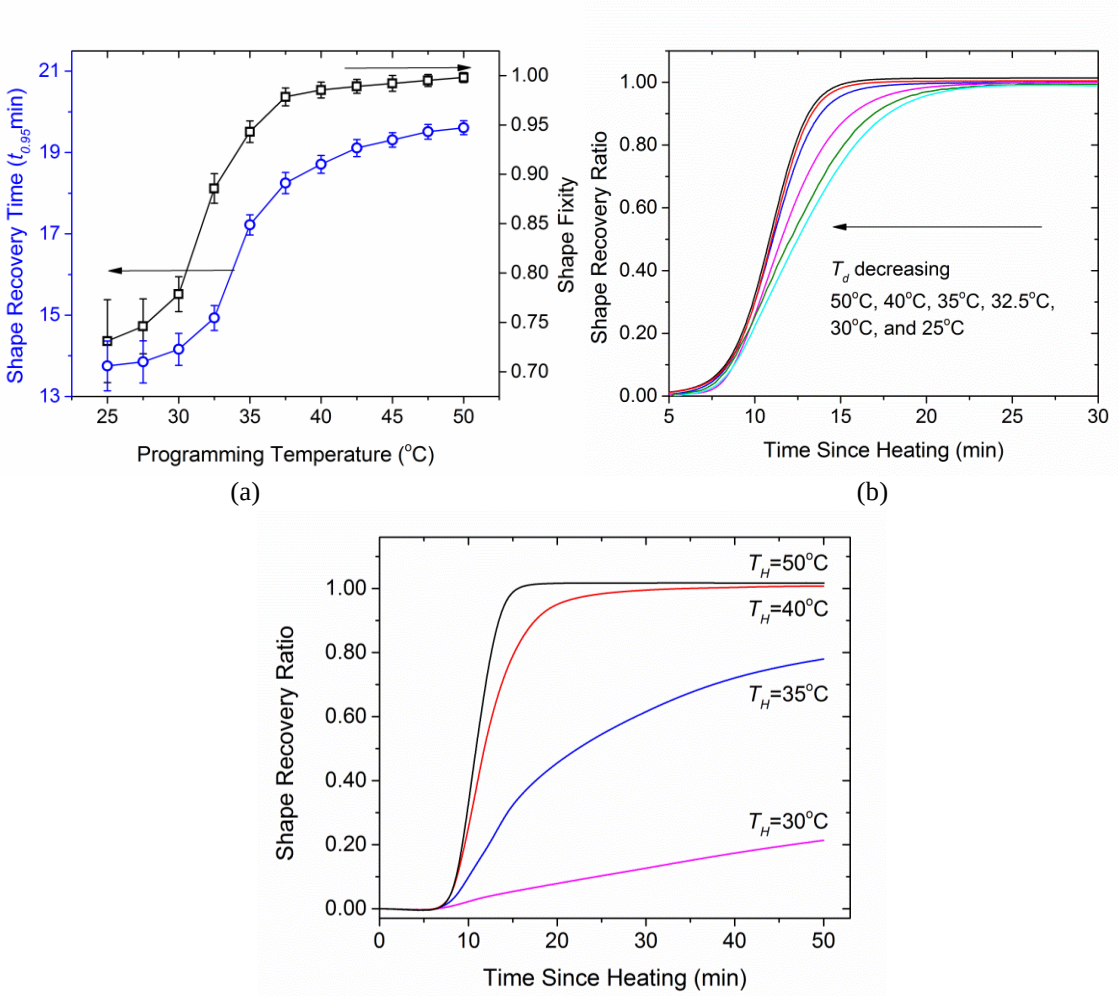

Figure 3.1. Shape fixity and shape recovery behavior of SMP programmed at different temperatures (T_d). (a) Shape fix ratio and Shape recovery time ($t_{0.95}$) as a function of programming temperature (evenly distributed from 25°C to 50°C) (b) Shape recovery ratio as a function of heating time. (c) Free shape recovery behavior of SMP under different recovery temperatures (T_r). T_r is taken as four different temperatures: 30 ℃, 35 ℃, 40 ℃ and 50 ℃ respectively.

Figure 3.2a shows that the shape fixity can also be affected by the holding time at high temperatures. In Figure 3.2a, after being held at T_d for different time periods (6×10^0 s, 6×10^2 s and 6×10^3 s), all the samples were cooled to T_L (20 °C) at the same cooling rate of 2.5 °C /min. Clearly, increasing the holding time improves the shape fixity. Therefore, combining Figure 3.1a and Figure 3.2a, to achieve a higher shape fixity, one can either increase the holding time, or increase T_d. This also inspires the postulation that different programing conditions, if designed well, could actually lead to the same shape fixity. Indeed, as indicated by the dashed line in the figure, the 90% shape fixity can be achieved

by two programming conditions, T_d=33.77°C followed by stabilization at T_d for 6×10^0 s, and T_d=29.97 °C followed by stabilization at T_d for 6×10^2s.

Since the two different programming conditions give to the same fixity, the next question is if these two programming conditions lead to two different or identical recovery performances under the same recovery conditions. Figure 3.2b shows the experimental results of the above two cases (T_d=33.77 °C with 6×10^0 s holding time, and T_d=29.97 °C with 6×10^2 s holding time) by heating to T_r (40 °C) at the heating rate of 2.5 ℃/min. The corresponding shape recovery ratio is plotted in the figure as a function of heating time. The nearly overlapped shape recovery curves indicate that the same shape fixity will lead to the same recovery profile. Therefore, when the SMPs are subjected to the same free recovery condition, the shape recovery behavior is essentially independent on the details of the programming history, but can be solely determined by the shape fixity.

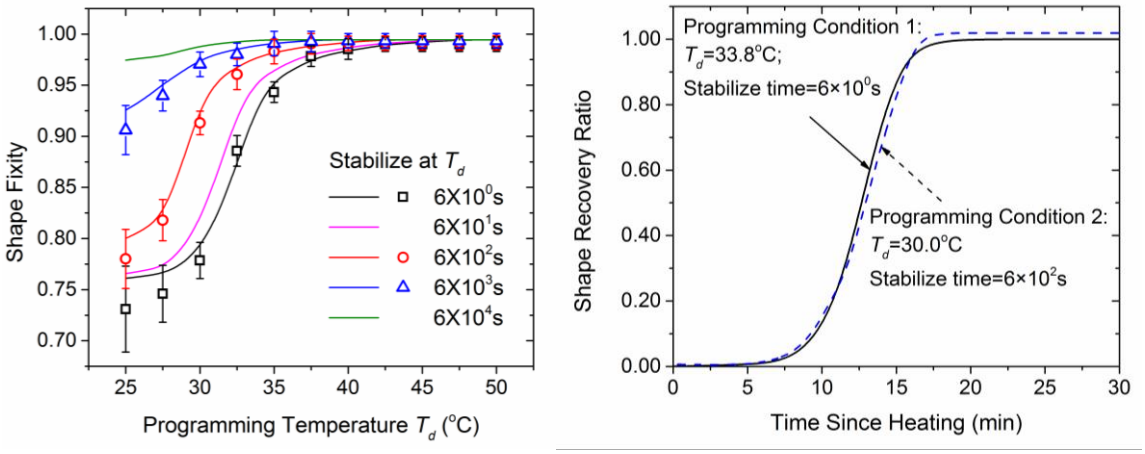

(a) (b)

Figure 3.2. (a) Shape fixity as a function of programming temperature (T_d) and holding time at T_d. Note: Dots denote the experimental results and solid lines denote simulation results, which is discussed in detail in the following section; The low temperature T_L is always 20 °C in all the experimental cases. (b) Shape recovery behavior of SMPs experienced by two programming conditions that achieve the same shape fix ratio (90%).

3.2 A Unified Parameter: Reduced Time

As shown above, the fixity can be achieved by different programming methods and determines the free recovery. It then becomes intriguing to explore if there exists a parameter that determines the fixity, and thus dictates the recovery.

To answer this question, we are still using the 1D multi-branched constitutive model as introduced in Chapter 2. It is necessary to understand why different programming methods lead to the same fixity. For the above two mentioned programming conditions that lead to the same 90% shape fixity, the stress evolutions in each branch of the multi-branch model are plotted as histogram in Figure 3.3. As shown in the figure, when the SMP material is programmed at a lower temperature (T_d=29.97°C, the second programming condition), the internal stress in each nonequilibrium branch is generally higher than that programmed at a higher temperature (T_d=33.77°C, the first programming condition), especially in branches with small relaxation times. However, since the second programming condition has a longer holding time (6×10^2s) at T_d in, the amount of stress relaxation stress is higher. Therefore, the overall effect is that two programming conditions lead to the same internal stress state before and after the sudden unloading.

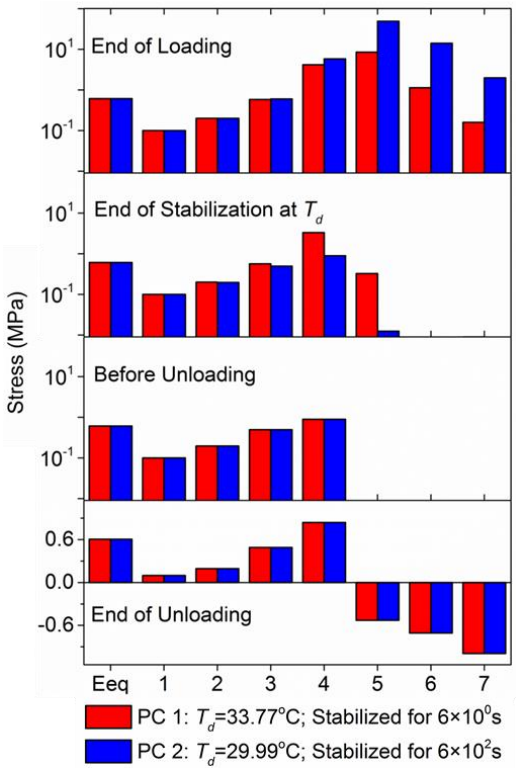

Figure 3.3. Stress evolutions in each branch of the multi-branch model during the two programming processes that achieve the same shape fixity (90%). Note: the number in the x-axis label denotes the *i-th* nonequilibrium branch

Now we may conjecture that the same shape fixity is due to the same internal stress distribution before unloading. Indeed, this is confirmed by the calculation of R_f based on

the multi-branch modeling frame. During the sudden unloading, all the dashpots could be considered as frozen, and the shape fixity R_f is calculated by the shape bouncing back of the model, which can be calculated by the mechanical equilibrium:

$$R_f = 1 - \frac{\sigma(t)}{\left(E_{eq} + \sum_{i=1}^{n} E_i\right) e_{\max}}. \tag{3-1a}$$

From Eq. 3-1a, since the denominator is a constant, it is clear the total stress before unloading dictates the shape fixity. To simplify the further analysis, we assume that the mechanical loading is instantaneous, and ignore the influence of thermal contraction on the rheological stress distribution under the constrained boundary condition[1]. Therefore, the total stress before unloading can be expressed as

$$\sigma(t) = e_{\max}\left[E_{eq} + \sum_{i=1}^{n} E_i \exp\left(-\frac{t}{\tau}\right)\right] = e_{\max} E_{relax}(t,T), \tag{3-1b}$$

where $E_{relax}(t)$ is the instantaneous relaxation modulus before unloading. Finally,

$$R_f = 1 - \frac{E_{relax}(t,T)}{E_{eq} + \sum_{i=1}^{n} E_i}. \tag{3-1c}$$

Eq. 3-1c also indicates that the instantaneous relaxation modulus before unloading determines the shape fixity of the SMP. It is well known that for thermo-rheologically simple polymers, the relaxation modulus follows the time-temperature superposition principle (TTSP), i.e.

$$E_{relax}(t,T) = E_{relax}(t_r, T_0), \tag{3-2a}$$

where $t_r = \alpha^{-1}(T)t$; $\alpha(T)$ is the shift factors in TTSP and is calculated using the method described in the Method section. Eq. 4a states that the instantaneous relaxation modulus at temperature T after time t is equal to the relaxation modulus at temperature T_0 after time t_r. For non-isothermal process,

$$t_r = \int_0^t \frac{ds}{\alpha(T)}, \tag{3-2b}$$

[1] The effect of non-instantaneous loading conditions is discussed in APPENDIX A at the end of this chapter. It is found that the influence of loading rate and thermal contraction is negligible in most SMP applications.

where t_r is the reduced time [21] and t is the physical time during the experiments. Combining Eq. 3-1c, 3-2a and 3-2b, we have

$$R_f = 1 - \frac{E_{relax}(t_r, T_0)}{E_{eq} + \sum_{i=1}^{n} E_i}. \quad (3\text{-}2c)$$

Eq. 3-2c states that the reduced time t_r measured at the reference temperature T_0 determines the shape fixity. In other words, if the two programming conditions have the same reduced programming time before unloading, they will lead to identical shape fixity. This is further confirmed by Table 3-1, which list the reduced time for the two programming conditions in Figure 3.3 using T_0=27.5 ^{o}C.

Table 3-1. The reduced programming times before unloading in the two programming conditions that achieve the same shape fix ratio (90%)

Shape Fixity	***Programming Conditions***	***Reduced Programming Time***
90%	1. T_d=33.8^{o}C; Stabilized at T_d for 6×10^0 s	1. 4.914×10^3 s
	2. T_d=30.0^{o}C; Stabilized at T_d for 6×10^2 s	2. 4.914×10^3 s

Since the relaxation modulus is a function of the reduced time, the reduced time is an effective measurement of the polymer rheological state during the programing process. As shown in Figure 3.4, three reduced times (1.0×10^3 s, 2.0×10^3 s and 3.0×10^3 s) are marked on the timing axis, and then respectively transferred back into the physical programming time according to the thermal history in the two programming conditions. The comparisons between the internal stress states reveal that the same reduced time, although corresponding to different physical times in the real programming situations, leads to the same stress distribution in each branch of the model. Such a merit of reduced time provides theoretical basis to correlate alternative programming conditions to achieve the same fixity.

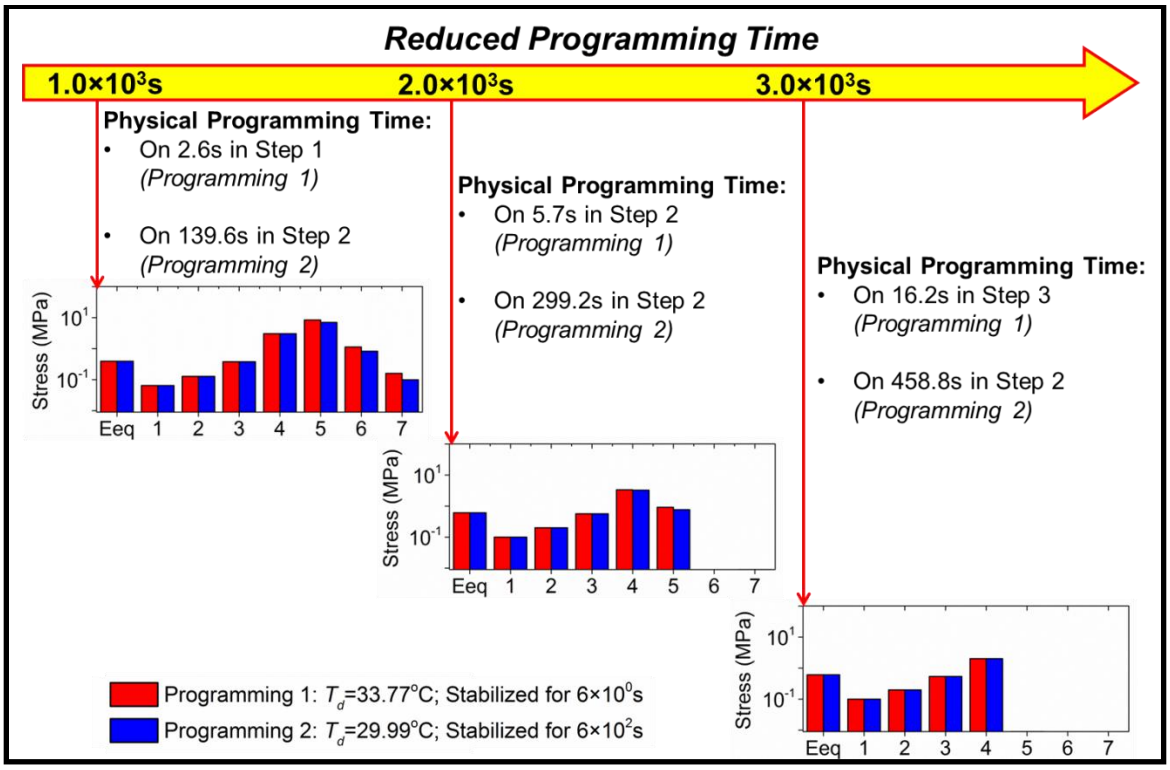

Figure 3.4. Stress status within the multi-branch model at different physical programming time but the same reduced programming time for two different programming conditions

In the following discussions, we demonstrate that the reduced time is also a unified parameter in predicting the free shape recovery of SMPs. We replot Figure 3.1c by transferring the physical time scale to the reduced time scale using Eq. 3-2 with T_0= 27.5 ^oC. As shown in Figure 3.5, the four recovery curves at different recovery temperatures rejoin to form a master free recovery curve after the time scale transfer, which indicates that the free recovery behaviors of SMPs also follow the TTSP. According to the physical meaning of Eq. 3-2b, Figure 3.5 also shows the recovery curve at T_0= 27.5 ^oC.

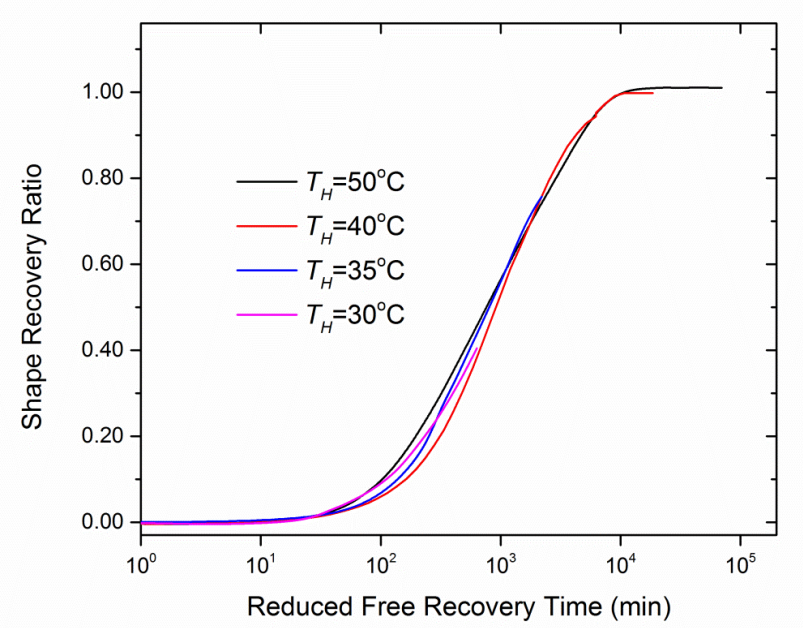

Figure 3.5. After transferring the physical free recovery time into the reduced free recovery time, the four shape recovery curves joined to form a master free recovery curve.

The existence of the master free recovery curve inspires us to develop a method to predict their temperature dependent free recovery behavior. When the shape fixity is given, the stress distribution in each branch of the model before and after unloading could be obtained, which serves as the initial condition for the following free recovery process. Then using the analytical solutions to the multi-branch model under free recovery condition, the recovery ratio curves that correspond to different shape fixities are predicted at the reference temperature (27.5°C) and shown in Figure 3.6a. With different shape fixities, the SMP specimens recover at different rates and therefore different recovery ratios for a given recovery time. Then by selecting R_f = 98.7% (the same as the above mentioned experimental results) recovery curve as the master curve, the time scale (actually represents the reduced free recovery time) is transferred back into different physical free recovery timing scales according to the specified thermal condition (heating to T_r = 30 °C, 35 ℃, 40 ℃ and 50 ℃, respectively) as illustrated in the experiments. Consequently the temperature deponent free recovery curve is predicted in Figure 3.6b. Comparisons between the simulation and experimental results presented in Figure 3.6c indicate that the prediction method successfully captures the free recovery behaviors of acrylate SMP at different recovery temperatures.

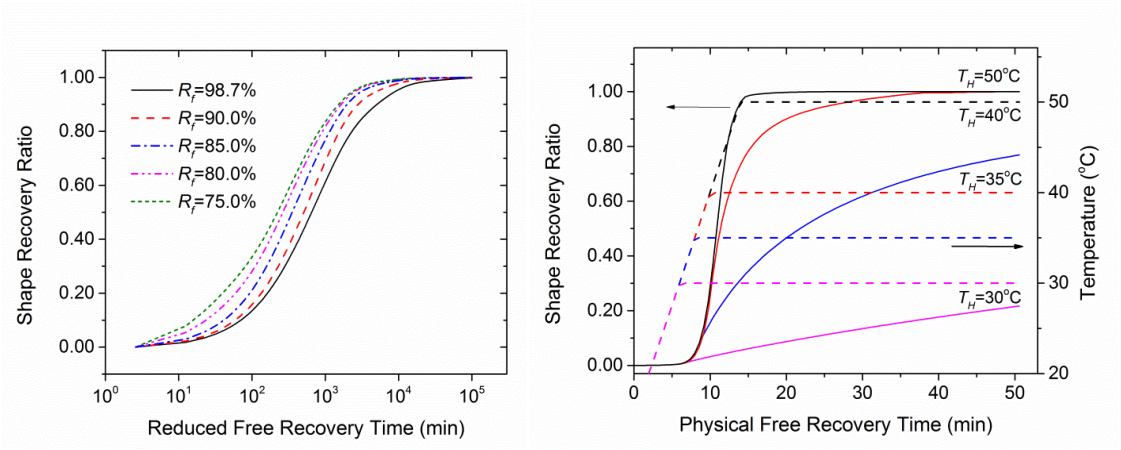

a b

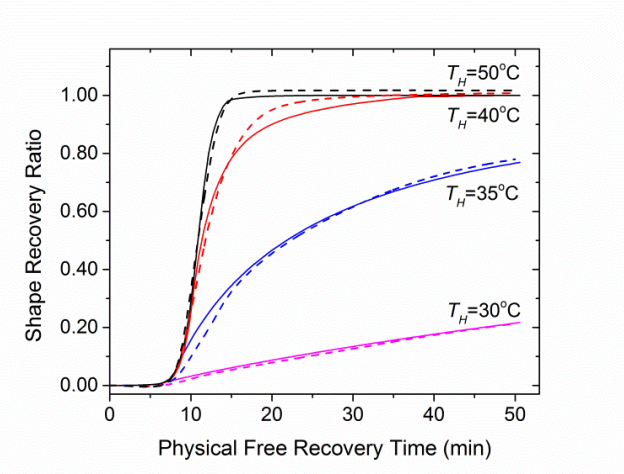

c

Figure 3.6. Prediction on the shape recovery behavior at different recovery temperatures. (a) The recovery temperature in each case is 27.5 °C while the programming temperature varies to achieve different shape fix ratio. Note: the 98.7% shape fixity represent the actual experimental results where the programming temperature is 40 °C (b) Selecting R_f= 98.7% shape recovery curve as the master curve, then transfer the reduced time back into the real physical free recovery time according to the specified thermal condition (the dash lines represent the corresponding recovery temperatures) (c) Comparisons between the simulation and experimental results. The simulation curves are denoted as dash lines

3.3 A Master Performance Map

The complicated dependence of polymer shape memory effect on the programming and free recovery conditions was unraveled by using the reduced time. Different thermo-temporal programming conditions can be measured by the reduced time at the reference temperature; the reduced time uniquely determines the shape fixity, which also uniquely determines the shape recovery in the reduced time scale. The free recovery in the

physical time scale under different thermo-temporal conditions can be obtained by inversely converting the reduced time back into the physical time. This process inspires the creation of a "shape memory performance map" (SMP-map), shown in Figure 3.7. There are three quadrants in Figure 3.7. The bottom-left quadrant shows the calculation of reduced programming time (azimuthal direction to the right) from holding time (vertical axis downward) and programming temperatures (individual curves). The top-right quadrant shows the conversion of physical recovery time (azimuthal direction to the left) from the reduced recovery time (vertical axis upward) at different temperatures (individual curves). The top-left quadrant, which represents the shape memory performance, shows the fixity (vertical axis on the left) as a function of reduced programming time (white line), and the recovery ratio (contour colors) as a function of reduced programming time and reduced recovery time.

To use the SMP-map, one starts with using the bottom-left quadrant to obtain the reduced programming time from a programming temperature and a holding time; using the top-left quadrant and the white curve, one then obtains the fixity. For a given recovery condition (with a recovery temperature and the time at that temperature), one obtains the reduced recovery time from the top-left quadrant. Then finally, using the reduced programming time and the reduced recovery time, one obtains the recovery ratio from the contour. As a demonstration, Figure 3.7 shows how to use the SMP-map to predict the shape fixity and recovery when a specified programming and free recovery condition is given. Assuming that the programming temperature T_d = 40.00 ^{o}C, holding time at T_d = 10min (600s), the reduced programming time (2.30×10^{4}min) is determined by following Path 1 in Figure 3.7b, which further pinpoints the shape fixity (98.7%) by following Path 2 in Figure 3.7a. For the subsequent free recovery step, if the intended recovery temperature T_r = 35.00^{o}C and the total heating time is 30min, the reduced recovery time is determined by Path 3 in Figure 3.7c. Using this reduced recovery time, together with the reduced programming time, one can finally obtain the recovery ratio (contour) as 74.1% (Path 4 in Figure 3.7a). It should be noted that in this demonstration case, the rest programming or recovery conditions (such as cooling rate, holding time at T_L, heating rate etc.) are the same as mentioned above. If these variables are interested for

predicting the shape fixity and recovery, Figure 3.7b and Figure 3.7c should be re-plotted accordingly.

As will be shown in the next section, the SMP-map can be readily constructed using the simple multi-branch model, whose parameters can be determined by stress relaxation experiments and a DMA test, which are standard rheological tests in polymer physics. Therefore, the SMP-map can be constructed from the standard polymer rheological experiments.

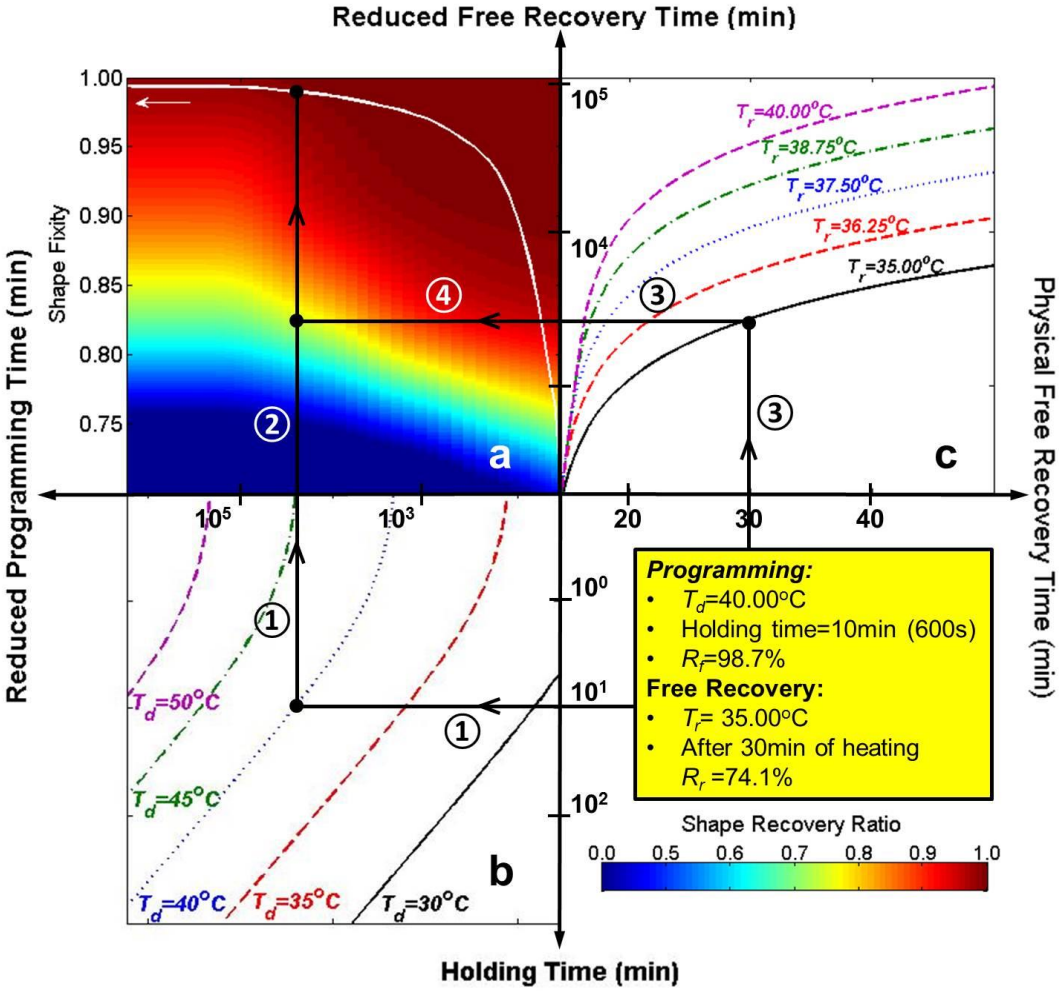

Figure 3.7. The shape memory performance map. (a) A general referential contour. (b) Reduced programming time as a function of holding time and programming temperature T_d. (c) Reduced free recovery time as a function of heating temperature T_H. Note: Other influencing factors are: Loading rate=1%/s; Cooling rate=2.5°C/min; T_L=20°C; Holding time at T_L=1hour; Heating rate=2.5°C/min.

3.4 Application in Studying the Temperature Memory Effect

A temperature memory effect (TME) refers to the ability of shape memory polymers

(SMPs) to memorize the temperature at which pre-deformation was conducted. In the past few years, this TME was experimentally demonstrated by comparing the applied programming temperature (T_d) with a characteristic recovery temperature (T_c), which corresponds to either maximum recovery stress or free recovery speed. In these well designed experiments, T_c was observed to be close to T_d, which is consistent with the intuitively understanding of 'memorization'. However, since the polymer recovery behavior has been proved to be strongly dependent on various programming and recovery details, a new question that whether T_c is always equal to T_d in any thermo-temporal conditions remains to be addressed. In this section, we will answer this question by using the concept of reduced time.

We start our discussions by firstly showing some experimental observations on the free recovery ratio and speed under different programming and recovery conditions. As a baseline SM cycle, the programming temperature T_d, the holding time t_h at T_d and the recovery heating rate q are respectively set to be 35^{o}C, 60s and 1^{o}C/min. Other experimental setup is the same as that described in Section 2.3. As comparisons, another two SM cycles were performed: one with increased programming temperature (T_d=40 ^{o}C), while the other one with decreased heating rate (q=0.1 ^{o}C/min). The shape recovery ratio and speed in these three SM cycles are respectively plotted in Figure 3.8a and Figure 3.8b as a function of recovery temperature (T_H).

As shown in Figure 3.8, both programing temperature and heating rate significantly affect the material free recovery profile: On one hand, increasing T_d from 35 ^{o}C to 40 ^{o}C will decrease the shape recovery speed under the same heating rate, and elevates the T_c from 34 ^{o}C to 38 ^{o}C. On the other hand, similar with previous study of Tobushi et al. [22], decreasing q increases the recovery speed versus recovery temperature, and consequently shift T_c to a small value. This is because a lower heating rate, which means longer heating time before reaching a given recovery temperature, would allow the SMPs to evolve more towards the equilibrium state and hence give a larger recovery strain. When the heating rate is set to be 0.1 ^{o}C/min, the T_c is seen to be decreased from 34 ^{o}C to 30 ^{o}C.

In addition to the experimental observations, simulation results based on the multi-branch model and predetermined model parameters are also plotted in Figure 3.8 as dash lines. A detailed description on the model parameters identification and simulation

procedure can be found in our previous work[23]. It could be seen that the numerical simulations adequately capture the temperature dependent shape recovery ratio and normalized recovery speed. In the following, parametric studies based on the multi-branch model will be performed to investigate the influence of programing and recovery conditions on the polymer TME.

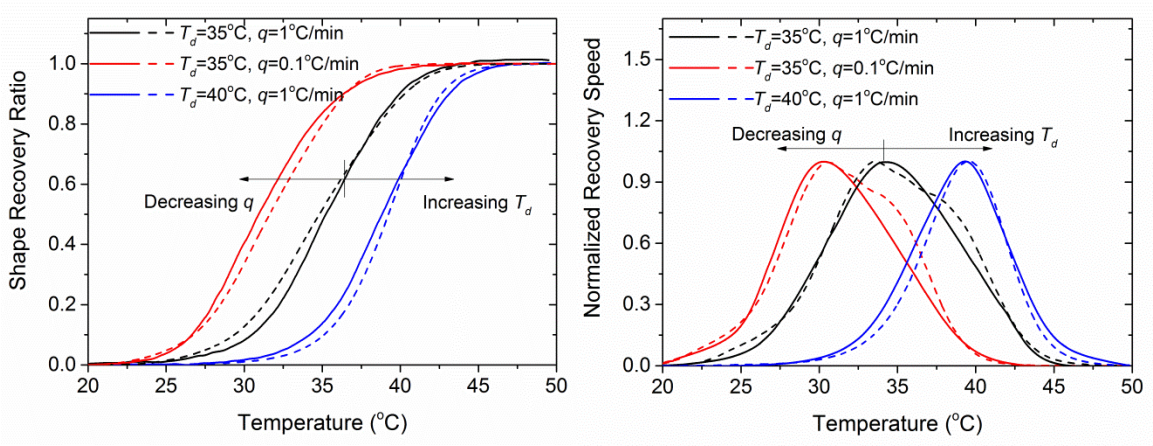

Figure 3.8. Influence of programming temperature and heating rate on the temperature dependent. (a) shape recovery ratio and (b) normalized shape recovery speed. Note: the dash line denote simulation curves by using the 1D multi-branch model.

Subsequently, parametric studies are conducted based on the 1D multi-branched model to examine the influence of both T_d and holding time t_h on the polymer free recovery profile. In Figure 3.9a, the T_d is gradually increased from 25 °C to 59 °C (2 °C of temperature interval) during the simulation, while the holding time t_h at T_d and the heating rate during the free recovery are respectively set to be 60s and 1 °C/min. Figure 3.9b shows the influence of t_h while the T_d and heating rate q are set to be 35 °C and 1 °C/min respectively in each simulation case. Figure 3.9c summarizes the recovery T_c as a function of both T_d and holding time t_h.

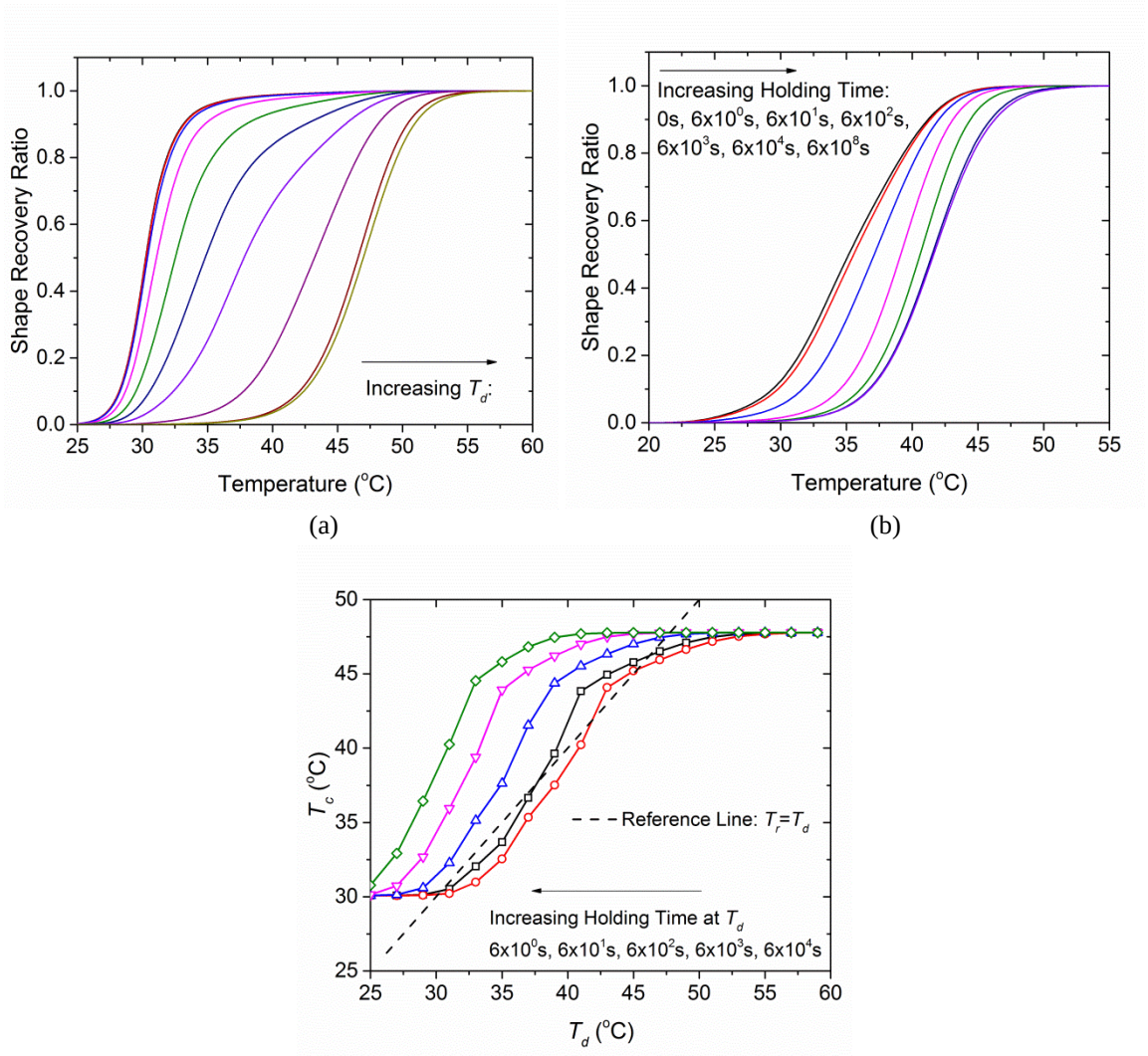

Figure 3.9. Parametric study on the influence of programing temperature and holding time. (a) Shape recovery ratio as a function of recovery temperature. (b) Shape recovery ratio with different holding times. T_d=35 °C. (b) T_c plotted as a function of both holding time t_h and T_d.

Clearly, the relation between T_c and T_d is not unique under the influence of t_h. Three main features could be found from the numerical simulations in Figure 3.9c. Firstly, within a specific temperature range, increasing programming temperature will decrease the recovery speed versus recovery temperature. T_c increases with T_d in exhibiting a roughly linear relation. This obeys the recognition of polymer TME that T_c observed during the free recovery step is close to the T_d applied at programing step. Secondly, beyond this temperature range, changing T_d dose not obviously affect the T_c. This prediction, that the TME could only be realized within a given temperature range, is consistent with the recent study of Wang et al [24]. Thirdly, a longer holding time will

increase the T_c towards a saturated level at ~ 47.5 ^{o}C. Besides, both onset and offset value of the temperature range with polymer TME observed decreases with the holding time increment.

The coupled influence of programming temperature and holding time can be explained by using the concept of reduced time (Eq. 3-2b), which uniquely determines the rheological stress state at the beginning of free recovery and consequently determines the free recovery speed. In this manner, any thermo-temporal programming conditions, such as holding time t_h after loading, cooling rates, and shape fixing temperature T_L etc., can also affect the recovery speed and the T_c by changing the reduced programming time and then consequently the rheological stress state.

For the curves in Figure 3.9c, after shifting each of them horizontally to a reference holding time t_{h0}, namely by

$$T_c(T_d, t_h) = T_c(\alpha_{th} T_d, t_{h0}), \tag{3-3a}$$

where α_{th} is the holding time dependent shift factors, a master curve can be constructed as shown in Figure 3.10a. The corresponding shift factors are plotted in Figure 3.10b as a function of holding time. A linear relation between α_{th} and t_h is then revealed in the semi-log scale. By using the nonlinear regression method, we approximate the relation as

$$\alpha_{th} = 0.85 + 0.083 \log(\frac{t_h}{t_{h0}}). \tag{3-3b}$$

Within the temperature range with clear polymer TME, Eq. 3-3 quantitatively demonstrates the packaging effect of both programming temperature and holding time on the T_c. That is, when a large holding time is applied during the polymer shape memory cycle, the corresponding shift factor will be exponentially ramped and therefore a smaller T_d should be used if an equivalent T_c is expected. Otherwise the T_c will be monotonically increased. The analysis on the effect of increasing T_d and t_h can be extended to the influence of other thermo-temporal programming conditions, such as decreasing loading rate, cooling rates, or increase the stabilization time at T_L etc.

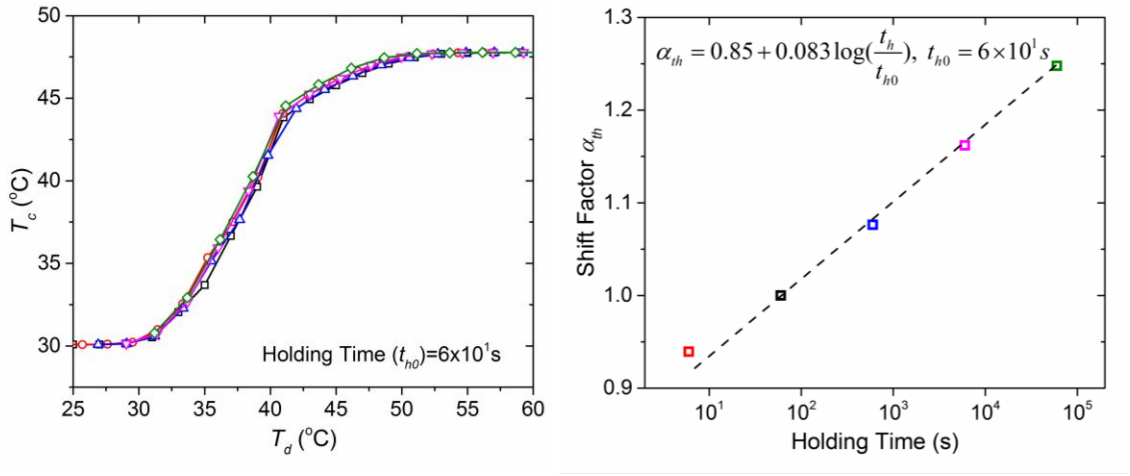

(a) **(b)**

Figure 3.10. (a) The constructed master curve of Tc. the referece holding time t_{h0}=6×10^{1}s. (b) The holding time dependent shift factors during the construction of master curve.

In addition to the programming condition, we will show in this section that the relation between T_c and T_d is also dependent on the free recovery condition. Considering a SM cycle with continuous heating method, the only parametric variable under investigation is the recovery heating rate q. Figure 3.11a shows the predicted free recovery curves with q increasing from 10^{-3} °C/min to 10^2 °C/min. All the programming procedures are set to be identical in each simulation case with T_d= 35 °C and holding time equal to 60s.

As demonstrated in our previous study [25], if the SMPs are experienced by the same programming step, their free recovery ratio is only dependent on the reduced recovery time, and a larger reduced recovery time will lead to a higher recovery ratio, namely:

$$R_r = R_r(t_r) \tag{3-4a}$$

with

$$t_r = \int_{T_L}^{T_H} \frac{dT}{q\alpha(T)}\ , \tag{3-4b}$$

where T_H is a given recovery temperature. Eq. 3-4b indicates that a larger heating rate will decrease the reduced recovery time and then consequently the recovery ratio when T_H is reached, as confirmed in Figure 3.11a. Figure 3.11b summarizes the recovery T_c as a function of both T_d and q. In addition to the revealed relation between T_c and T_d that is dependent on q, the temperature range to observe polymer TME is shown to be unchanged upon changing the heating rate.

Subsequently, by shifting each curves in Figure 3.11b vertically into to a reference heating rate (q_0=10^0 °C/min) according to

$$T_c(T_d, q) = \frac{1}{\alpha_q} T_c(T_d, q_0) \tag{3-5a}$$

where α_q is a heating rate dependent shift factor, the curves are seen to be rejoined together to form a master curve, as shown in Figure 7c. The corresponding shift factors are summarized in Figure 7d. In the semi-log scale, the shift factor is linearly decreased as the increment of heating rate, namely:

$$\alpha_q = 1 - 0.092 \log(\frac{q}{q_0}) \tag{3-5b}$$

Eq. 3-5 quantitatively approximates the influence of recovery heating rate on the T_c with two features revealed: firstly, when a larger heating rate q is applied during the polymer free recovery step, both the shift factor and corresponding T_c will be decreased. Secondly, different from the above mentioned effect of programing condition, there is no boundary heating rate condition for the influence of heating rate. Keeping on increasing q will continually elevate T_c towards the target T_H. An infinitely large value is representing an isothermal recovery condition, where the T_c is always equal to T_H regardless of the applied programming temperature. In the opposite, if no heat is applied during the recovery step, namely q=0, a thermally simple SMP can still recover into the original shape, even though this process may take for several years [25, 26]. Under this condition, T_c is equal to the shape fixing temperature T_L.

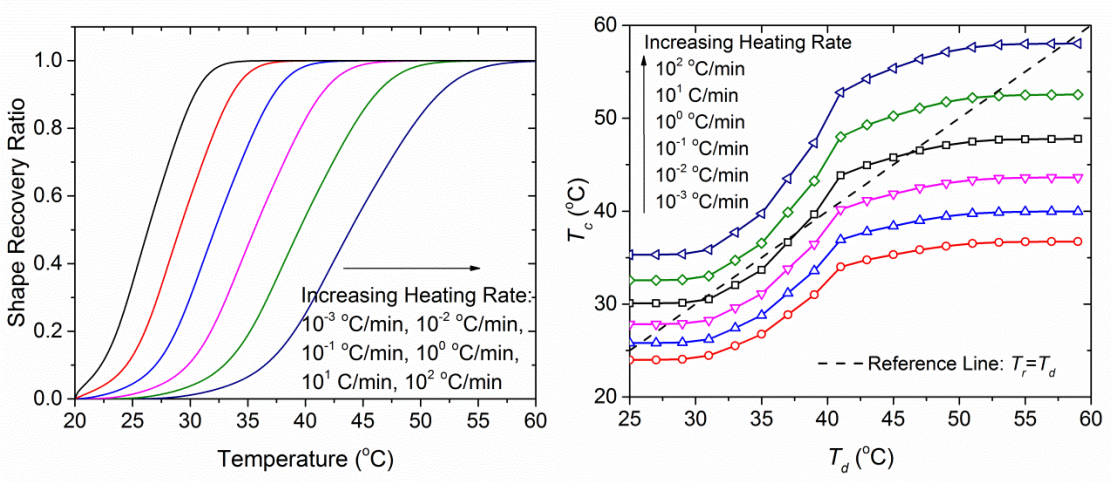

(a) **(b)**

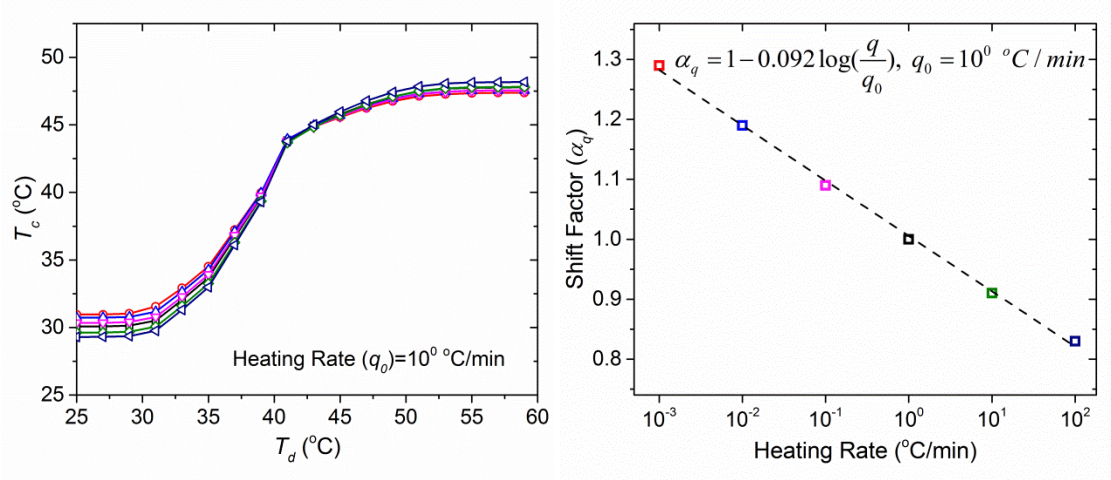

(c) **(d)**

Figure 3.11. Influence of both Td and heating rate q on the free recovery profiles and Tc of SMPs. (a) The predicted free recovery curves with different heating rates. T_d=35 °C and holding time equals to 6s. (b) T_c plotted as a function of both T_d and q. (c) The constructed master curve of T_c. The referece heating rate q_0=10^0 °C/min. (d) The heating rate dependent shift factors during the construction of master curve.

3.5 Conclusion

In this chapter, we firstly presented a unified method to predict the shape memory performance of thermo-rheologically simple SMPs under different thermo-temporal conditions. The fundamental conclusion is that the influence of programming conditions to free recovery can be unified by a reduced programming time that uniquely determines shape fixity, which consequently uniquely determines the shape recovery with a reduced recovery time. By using the time–temperature superposition principle, shape recoveries under different thermo-temporal conditions can be extracted from the shape recovery under the reduced recovery time. The developed prediction method is independent on the model details.

Based on the unified modeling approach, we studied the polymer temperature memory effect (TME) in a free shape memory cycle, where the temperature T_c at which a maximum shape recovery rate is observed is shown to be close to the applied programming temperature (T_d). However, our study demonstrates that such a memorization on T_d is not unique. Any other thermo-temporal conditions that determine the reduced programming or recovery time will affect the recovery T_c. For example, during the programming step, increasing holding time plays the same role as increasing

T_d in assisting the stress relaxation within the polymer material, and then consequently reduces the recovery speed versus temperature and increase T_c. In the recovery step, decreasing the heating rate will lead a longer recovery time, which allows the SMPs evolve more toward to the equilibrium state. In this manner, the recovery T_c is decreased. The polymer TME indeed represents a synergistic effect of both programming and recovery conditions on the material free recovery behavior. In addition, we also explained why the polymer TME could only be observed within a given temperature range. While this temperature range can be influenced by the programing history, it is essentially independent on the applied recovery condition.

Based on the studies in this chapter, we can gain a deeper understanding of how the programming and recovery conditions will affect the free recovery behavior of SMPs synergistically, which consequently provides a facile strategy to optimize the shape memory performance of SMPs by adjusting their thermomechanical working conditions, instead of developing new polymer systems. Such a strategy offers huge convenience for engineering SMPs in the industry, especially in the fields of medicine, aeronautics and astronautics, where a long period of performance verification and official approval is typically expected.

Appendix A: Influence of Loading Rate and Thermal Expansion

By using the constitutive relations mentioned above, we analyze the influence of loading rate and thermal expansion during programming on the prediction of polymer shape fixity. Under the programming temperature T_d, if the loading process is instantaneous, the stress in each nonequilibrium branch at the end of holding step is:

$$\sigma_i = E_i e_m \exp(-t_0/\tau_i), \tag{A1a}$$

where t_0 is the holding time, and τ_i is the temperature dependent relaxation time in each branch. However, when loading rate is a concern, the stress at the end of holding step is calculated as:

$$\sigma_i' = E_i e_m \exp(-t_0/\tau_i)\left[\frac{\exp(t_1/\tau_i)-1}{t_1/\tau_i}\right], \tag{A1b}$$

where t_1 is the loading time, and the total time for loading and holding steps are still t_0.

A comparison between Eq. A1a and Eq. A1b implies that under a finite loading rate, the stress in each nonequilibrium branch at the end of holding step is larger than that from instantaneous loading condition. Such a stress increment $\Delta\sigma_i^0 = \sigma_i' - \sigma_i$ could be estimated by using Taylor expansion:

$$\Delta\sigma_i^0 = E_i e_m \exp(-t_0/\tau_i)\left[\frac{1}{2}\left(\frac{t_1}{\tau_i}\right) + \frac{1}{6}\left(\frac{t_1}{\tau_i}\right)^2\right]. \tag{A2}$$

During the cooling step, while the external stretch is sustained, this stress increment would be further deceased due to the stress relaxation:

$$\Delta\sigma_i = \Delta\sigma_i^0 \exp(-\Gamma_i), \tag{A3}$$

where the additional exponential item $\exp(-\Gamma_i)$ quantifies the relaxation degree, which dependents on the specified thermal condition during the cooling step.

When the loading rate is under consideration, Eq. A3 actually describes the stress increment at the end of cooling, which also equals to the stress increment before unloading. Since previous discussions revealed that the shape fixity is dependent on the rheological stress distribution within the multi-branch model before unloading, this stress increment in each branch would reduce the predicted shape fixed by ΔR_f as it will lead to additional spring back deformation during the unloading process. The shape fixity under the consideration of loading rate is written as:

$$R_f = R_f^0 - \Delta R_f, \tag{A4}$$

with

$$R_f^0 = 1 - \frac{E_0 + \sum_{i=1}^{n} E_i \exp(-t_0/\tau_i)\exp(-\Gamma_i)}{\sum_{i=1}^{n} E_i}, \tag{A5a}$$

to describe the shape fixity under instantaneous loading and with

$$\Delta R_f = \frac{\sum_{i=1}^{n} E_i \exp(-t_0/\tau_i)\left[\frac{1}{2}\left(\frac{t_1}{\tau_i}\right) + \frac{1}{6}\left(\frac{t_1}{\tau_i}\right)^2\right]\exp(-\Gamma_i)}{\sum_{i=1}^{n} E_i}, \tag{A5b}$$

to describe the decrease of shape fixity under the loading time of t_1.

In seeking the maximum decrease in shape fixity under the influence of loading rate, we further consider the following extreme condition: the loading time t_1 equals to t_0, and after the loading and holding process at T_d, the SMP material is immediately cooled down to the low temperature T_L, and then proceed to the unloading process. In this manner, the viscous flow in the nonequilibrium branch is negligible which renders the exponential item $\exp(-\Gamma_i)$ equals to 1. Therefore, Eq. A5b gives the maximum change in shape fixity, which under this extreme condition is expressed as:

$$\Delta R_f = \frac{\sum_{i=1}^{n} E_i B_i\left(t_0, \tau_i\right)}{\sum_{i=1}^{n} E_i}, \tag{A6a}$$

$$B_i\left(t_0, \tau_i\right) = E_i \exp(-t_0/\tau_i)\left[\frac{1}{2}\left(\frac{t_0}{\tau_i}\right) + \frac{1}{6}\left(\frac{t_0}{\tau_i}\right)^2\right]. \tag{A6b}$$

In Eq.A6b, B_i has the maxima 0.25 when $t_0 \approx 1.3\tau_i$. Note that the (i-1)-*th* branch has τ_{i-1}=0.1τ_i, B_{i-1} has maxima is 0.059; for the (i+1)-*th* branch with τ_{i+1}=10τ_i , B_{i+1} has the maxima of 8×10^{-5}. Therefore, for a given loading time t_0, the term that contributes to S21b dominantly is the term that has the relaxation time is close to t_0, namely $\tau_i \sim t_0$; the rest of the terms in Eq. A6b can be neglected. The maximum of ΔR_f could then be estimated by considering only one branch in the numerator in Eq. A6 with the largest elastic modulus:

$$\Delta R_f \approx \frac{0.25E_1}{\sum_{i=1}^{n} E_i}. \tag{A7}$$

For the studied acrylate SMP, E_1=618.45MPa and $\sum_{i=1}^{n} E_i$=1394MPa . Therefore $\Delta R_f = 0.11$ indicates that the influence of loading rate will lead to a decrease in shape fixity of 0.11 for maximum.

It should be noted that such a decrease in shape fixity serves as upper bound, which is in general much larger than under the normal loading conditions. In a typical SM cycle, the programming temperature is usually around or above the glass transition temperature.

For example, at 35°C, the relaxation time in the first nonequilibrium branch is ~1.2×10^{-2} s, which is further decreased to ~7.6×10^{-5} s at 45 °C. Obviously, the loading time in practical applications would be highly above these values, which significantly reduces the ΔR_f as expressed in Eq.A6. In addition, after the loading step, a holding process is usually followed for a given time, and then the SMP material is cooled at a specified cooling rate. All of these tends to further decrease ΔR_f and hence the concerned influence of loading rate. We quantitatively define the prediction error of shape fixity under the influence of loading rate as:

$$\Delta e_r = \frac{R_f^0 - R_f}{R_f^0} \times 100\% . \tag{A8}$$

Fig.A1 visualizes the error as a function of loading time (from 0.6s to 600s) and programming temperature (from 25°C to 50°C). Here in the figure, the total time for loading and holding step is kept as 600s, and other simulation procedures are the same as those mentioned in the main text. It is seen that noticeable prediction error occurs when the programming temperature is relatively low (below 30 °C) and the loading time is large (~600s) with the maximum error under 6%. For the rest majority of loading condition, the error is less than ~1%.

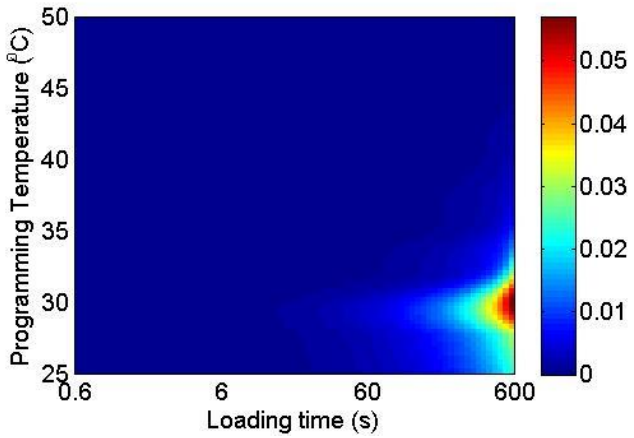

Figure A1: The prediction error of shape fixity at different programming temperatures under the influence of loading rate.

3.6 References

1. Tobushi, H., T. Hashimoto, and N. Ito, *Shape fixty and shape recovery in a film of shape memory polymer of polyurethane series.* Journal of Intelligent Material Systems and Structures, 1998. **9**: p. 127-136.

2. Tobushi, H., et al., *Shape fixity and shape recovery of polyurethane-shape memory polymer foam.* Trans Mater Res Soc Jpn, 2001. **26**: p. 351-354.
3. Ge, Q., et al., *Mechanisms of Triple-Shape Polymeric Composites Featuring Dual Thermal Transitions.* Soft Matter, 2013. available online.
4. Ge, Q., et al., *Prediction of Temperature Dependent Free Recovery Behaviors of Shape Memory Polymers.* Soft Matter, 2012. **8**: p. 11098–11105.
5. Yu, K., et al., *Design considerations for shape memory polymer composites with magnetic particles.* Journal of Composite Materials, 2013. **47**(1): p. 51-63.
6. Yu, K., et al., *Mechanisms of multi-shape memory effects and associated energy release in shape memory polymers.* Soft Matter, 2012. **8**(20): p. 5687-5695.
7. Ge, Q., et al., *Thermomechanical behavior of shape memory elastomeric composites.* Journal of the Mechanics and Physics of Solids, 2011. **60**(1): p. 67-83.
8. Westbrook, K.K., et al., *A 3D finite deformation constitutive model for amorphous shape memory polymers: A multi-branch modeling approach for nonequilibrium relaxation processes.* Mechanics of Materials, 2011. **43**(12): p. 853-869.
9. Castro, F., et al., *Time and Temperature Dependent Recovery of Epoxy-Based Shape Memory Polymers.* Journal of Engineering Materials and Technology-Transactions of the Asme, 2011. **133**(2).
10. Castro, F., et al., *Effects of thermal rates on the thermomechanical behaviors of amorphous shape memory polymers.* Mechanics of Time-Dependent Materials, 2010. **14**(3): p. 219-241.
11. Qi, H.J., et al., *Finite deformation thermo-mechanical behavior of thermally induced shape memory polymers.* Journal of the Mechanics and Physics of Solids, 2008. **56**(5): p. 1730-1751.
12. Westbrook, K.K., et al., *Improved testing system for thermomechanical experiments on polymers using uniaxial compression equipment.* Polymer Testing, 2010. **29**(4): p. 503-512.
13. Nguyen, T.D., et al., *A thermoviscoelastic model for amorphous shape memory polymers: Incorporating structural and stress relaxation.* Journal of the Mechanics and Physics of Solids, 2008. **56**(9): p. 2792-2814.
14. Yakacki, C.M., et al., *Unconstrained recovery characterization of shape-memory polymer networks for cardiovascular applications.* Biomaterials, 2007. **28**(14): p. 2255-2263.
15. Cui, J., K. Kratz, and A. Lendlein, *Adjusting shape-memory properties of amorphous polyether urethanes and radio-opaque composites thereof by variation of physical parameters during programming.* Smart Materials & Structures, 2010. **19**(6).
16. Wong, Y.S. and S.S. Venkatraman, *Recovery as a measure of oriented crystalline structure in poly(L-lactide) used as shape memory polymer.* Acta Materialia, 2010. **58**(1): p. 49-58.
17. Xie, T., K.A. Page, and S.A. Eastman, *Strain-Based Temperature Memory Effect for Nafion and Its Molecular Origins.* Advanced Functional Materials, 2011. **21**(11): p. 2057-2066.
18. Xie, T., *Tunable polymer multi-shape memory effect.* Nature, 2010. **464**(7286): p. 267-270.

19. Miaudet, P., et al., *Shape and temperature memory of nanocomposites with broadened glass transition.* Science, 2007. **318**(5854): p. 1294-1296.
20. Kratz, K., et al., *Temperature-Memory Polymer Networks with Crystallizable Controlling Units.* Advanced Materials, 2011. **23**(35): p. 4058-+.
21. Scherer, G.W., *Relaxation in Glass and Composites*. 1992, Malabar, Florida: Krieger publishing company.
22. Tobushi, H., et al., *Thermomechanical constitutive model of shape memory polymer.* Mechanics of Materials, 2001. **33**(10): p. 545-554.
23. Yu, K. and H.J. Qi, *Temperature memory effect in amorphous shape memory polymers.* Soft Matter, 2014. **10**(47): p. 9423-9432.
24. Wang, Y.R., et al., *Relation between temperature memory effect and multiple-shape memory behaviors based on polymer networks.* Rsc Advances, 2014. **4**(39): p. 20364-20370.
25. Yu, K., G. Qi, and H.J. Qi, *Reduced time as a unified parameter determining fixity and free recovery of shape memory polymers.* Nature communications, 2014. **5**: p. 3066.
26. Ge, Q., et al., *Prediction of temperature-dependent free recovery behaviors of amorphous shape memory polymers.* Soft Matter, 2012. **8**(43): p. 11098-11105.

CHAPTER 4

THREE-DIMENSIONAL FINITE DEFORMATION CONSTITUTIVE MODELING FOR SHAPE MEMORY POLYMERS

In the aforementioned studies about shape memory polymers (SMPs), the constitutive relations are based on the linear viscoelasticity. In this chapter, these constitutive relations will be extended to three-dimensional (3D) finite deformation relations. The extended constitutive model is essentially comprehensive and can be applied to capture some general features of amorphous network polymers in addition to the shape memory behavior, such as nonlinear thermal expansion, non-linear deformation of rubbery polymer, yielding and post-yielding softening behavior of glassy polymers. By incorporating these constitutive relations with the finite element method (FEM), we are able to study the thermomechanical and shape recovery properties of SMP composites under the coupling effect of non-uniform temperature filed and stress field.

4.1 Constitutive Relations

We firstly present the three-dimensional (3D) constitutive model. More details of this modeling frame can be found in Westbrook et al [1]. Figure 4.1 shows the 1D rheological representation of the applied model. A thermal expansion component is arranged in series with the multi-branched model. The equilibrium branch is a hyperelastic spring to represent the equilibrium behavior of SMPs. For the nonequilibrium branches, *m* branches are used to represent the relaxation behavior of the glassy mode, and the remaining *n* nonequilibrium branches are used to represent the relaxation processes in the rubbery state. As is mentioned in Chapter 2, in the *ith* $(1 \le i \le m+n)$ nonequilibrium branch, the initial modulus of the springs is denoted as E^i and the relaxation time of the dashpot is τ^i ($1 \le i \le m$ represents the glassy branch and $m+1 \le i \le m+n$ represents the rubbery branch).

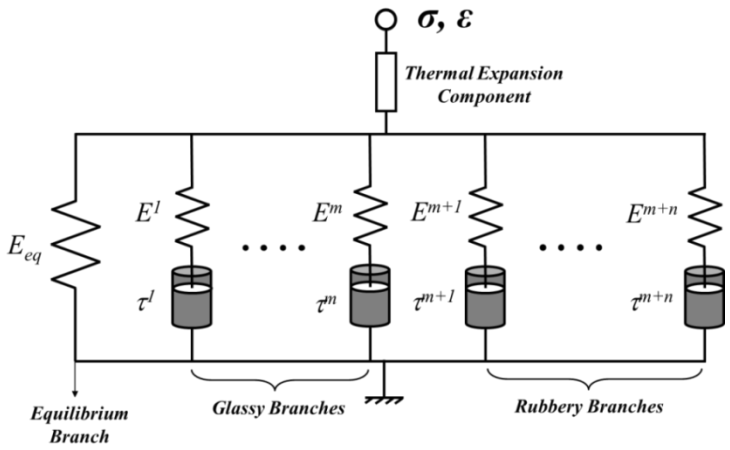

Figure 4.1. 1D rheological representation for the 3D finite deformation constitutive model

As demonstrated by Holzapfel [2], the total deformation gradient of the model $\mathbf{F}$ can be decomposed as:

$$\mathbf{F} = \mathbf{F}_M \mathbf{F}_T , \tag{4-1}$$

where $\mathbf{F}_M$ is the mechanical deformation gradient and $\mathbf{F}_T$ is the thermal deformation gradient.

The total Cauchy stress of the model $\boldsymbol{\sigma}$ is

$$\boldsymbol{\sigma} = \boldsymbol{\sigma}_{eq} + \sum_{i=1}^{m+n} \boldsymbol{\sigma}^i , \tag{4-2}$$

where $\boldsymbol{\sigma}_{eq}$ and $\boldsymbol{\sigma}^i$ are the Cauchy stresses in the equilibrium and the *ith* $(1 \le i \le m+n)$ nonequilibrium branches, respectively.

4.1.1 Thermal Expansion

The thermal expansion or contraction of the constructed thermal component in the model is assumed to be isotropic, i.e.

$$\mathbf{F}_T = J_T \mathbf{I} , \tag{4-3}$$

where $\mathbf{I}$ is the second order unit tensor. J_T is the volume change due to thermal expansion/contraction and is defined as:

$$J_T = \frac{V(T,t)}{V_0} = \left[1 + 3\alpha_r \left(T - T_0\right)\right]\left(1 + \delta\right), \tag{4-4}$$

where $V(T,t)$ is the volume at time *t* and temperature *T*. V_0 is the reference volume at the reference temperature T_0. α_r is the linear coefficient of thermal expansion (CTE) in the rubbery state and δ characterizes the deviation of volume from equilibrium volume [3-5]and

$$\delta = \frac{V(T,t)}{V_{eq}(T)} - 1,\ V_{eq}(T) = \left[1 + 3\alpha_r (T - T_0)\right] V_0, \tag{4-5}$$

where δ is calculated by the well-known KAHR 33-parameter[6].

4.1.2 Equilibrium Branch

The Cauchy stress tensor in the equilibrium branch uses Arruda-Boyce eight chain model[7], i.e.

$$\boldsymbol{\sigma}_{\text{eq}} = \frac{nk_B T}{3J_{\text{M}}} \frac{\sqrt{N}}{\lambda_{chain}} \mathcal{L}^{-1}\left(\frac{\lambda_{chain}}{\sqrt{N}}\right) \overline{\mathbf{B}}' + K\left(J_{\text{M}} - 1\right)\mathbf{I}, \tag{4-6a}$$

$$\overline{\mathbf{B}}' = \overline{\mathbf{B}} - 1/3\,\text{tr}\left(\overline{\mathbf{B}}\right)\mathbf{I},\ \overline{\mathbf{B}} = \overline{\mathbf{F}_{\text{M}}}\,\overline{\mathbf{F}_{\text{M}}}^{\text{T}},\ \overline{\mathbf{F}_{\text{M}}} = J_{\text{M}}^{-1/3}\mathbf{F}_{\text{M}}, \tag{4-6b}$$

$$\lambda_{chain} = \sqrt{tr\left(\overline{\mathbf{B}}\right)/3},\ \mathcal{L}(\beta) = \coth\beta - 1/\beta. \tag{4-6c}$$

where *n* is the crosslinking density, k_B is Boltzmann's constant, *T* is the temperature, N is the number of Kuhn segments between two crosslink sites (and/or strong physical entanglements). The temperature dependent shear modulus $\mu_r(T)$ of the elastomer in the equilibrium state (which is an indication of entropic elasticity) is given by nk_BT. *K* is the bulk modulus and is typically orders of magnitude larger than μ_r to ensure material incompressibility.

4.1.3 Nonequilibrium Branches

Although in Figure 4.1 we distinguished the non-equilibrium branches by glassy branches and rubbery branches, we attempted a unified viscous flow rule for all these branches. The difference between the glassy and rubber branches then comes from their definition of flow resistance, or more specifically, the relaxation time. For the rubbery branches, the relaxation time is a function of temperatures only; for the glassy branches, the relaxation time is a function of temperatures as well as stresses, which give to the

yielding behavior. For the *i-th* nonequilibrium branch ($1 \le i \le m+n$), the deformation gradient can be further decomposed into an elastic part and a viscous part

$$\mathbf{F}_M^i = \mathbf{F}_e^i \mathbf{F}_v^i, \tag{4-7}$$

where $\mathbf{F}_v^i$ is a relaxed configuration obtained by elastically unloading by $\mathbf{F}_e^i$. The Cauchy stress can be calculated using $\mathbf{F}_e^i$,

$$\boldsymbol{\sigma}^i = \frac{1}{J_e^i}\left[\mathbf{L}_e^i(T) : \mathbf{E}_e^i\right], \text{ for } 1 \le i \le m+n \tag{4-8a}$$

$$J_e^i = \det\left(\mathbf{F}_e^i\right),\ \mathbf{E}_e^i = \ln \mathbf{V}_e^i,\ \mathbf{V}_e^i = \mathbf{F}_e^i \mathbf{R}_e^{iT}, \tag{4-8b}$$

and $\mathbf{L}_e^i(T)$ is the fourth order isotropic elasticity tensor in the *i-th* nonequilibrium branch ($1 \le i \le m+n$), which is taken to be temperature independent in general, i.e.

$$\mathbf{L}_e^i(T) = 2G^i\left(\mathbf{I} - \frac{1}{3}\mathbf{I}\otimes\mathbf{I}\right) + K^i \mathbf{I}\otimes\mathbf{I}, \text{ for } 1 \le i \le m+n \tag{4-9}$$

where $\mathbf{I}$ is the fourth order identity tensor, G^i and K^i are shear and bulk moduli for each nonequilibrium branch ($1 \le i \le m+n$), respectively.

For the rubbery nonequilibrium branches ($1 \le i \le m$), it is assumed that all the rubbery branches have the same shear modulus, i.e.

$$G^i(T) = n_R k_B T \ \text{ for } 1 \le i \le m, \tag{4-10}$$

where n_R is the crosslinking density [8]. Since the bulk modulus is used to enforce a nearly incompressible condition, $K^i(T)$ is chosen to be independent of temperatures and be equal to *K* in the equilibrium branch (Eq. 4-6).

For the glassy nonequilibrium branches ($m+1 \le i \le m+n$), the shear modulus is taken to be independent of temperatures, i.e.

$$G^i(T) = \mu_g \ \text{ for } \ m+1 \le i \le m+n, \tag{4-11a}$$

and $K^i(T)$ is calculated through $G^i(T)$ using the Poisson ratio $v^i = v_g$,

$$K^i(T) = \frac{2(1+v_g)}{3(1-2v_g)}\mu_g \ \text{ for } \ m+1 \le i \le m+n, \tag{4-11b}$$

The elastic modulus in each nonequilibrium branch is calculated as

$$E^i(T) = \frac{G^i(T)}{2(1+\nu^i)} \text{ for } 1 \le i \le m+n. \tag{4-12}$$

In the rubbery branches, the temperature dependent relaxation times are calculated according to the thermorheological simplicity principle [8] (Eq. 2-2). For the glassy branches ($1 \le i \le m$), considering the stress induced yield-type behavior at a temperature below T_g, the relaxation time is taken to be a function of temperatures as well as stresses and can be evaluated by an Eyring type of function[9], i.e.

$$\tau^i\left(T, \overline{M^i}\right) = \tau_0^i \alpha_T(T) \exp\left(-\frac{\Delta G^i}{k_B T}\frac{\overline{M^i}}{s^i}\right), \text{ for } 1 \le i \le m, \tag{4-13a}$$

$$\mathbf{M}^i = J_e^i \mathbf{C}_e^i \left(\mathbf{F}_e^i\right)^{-1} \boldsymbol{\sigma}^i \left(\mathbf{F}_e^i\right)^{-T}, \ \overline{M^i} = \left[\frac{1}{2}\left(\mathbf{M}^i\right)' : \left(\mathbf{M}^i\right)'\right]^{1/2}, \tag{4-13b}$$

where, ΔG^i is the activation energy, s^i is the athermal shear strength representing the resistance to the viscoplastic shear deformation in the material, $\mathbf{M}^i$ is Mandel stress, and $\overline{M^i}$ is the equivalent shear stress.

In order to adequately account for the experimentally observed softening effects, the evolution rule for *s* is defined as

$$\dot{s}^i = h_0^i\left(1 - s^i / s_s^i\right)\dot{\gamma}_v^i \tag{4-14}$$

with $s^i = s_0^i$ when $\gamma_v^i = 0$, and s_0^i is the initial value of the athermal shear strength, s_s^i is the saturation value, h_0^i is a prefactor, $\dot{\gamma}_v^i$ is the viscous flow in glassy branches and is defined as $\dot{\gamma}_v^i = \overline{M^i}\left(G^i(T)\tau^i\left(T, \overline{M^i}\right)\right)^{-1}$ ($1 \le i \le m$). For the case when $s_0^i > s_s^i$, Eq. 4-14 represents an evolution rule that characterizes the experimentally observed softening behavior of the material.

4.2 Material Parameters Identification

In the followings, we will present the material parameters identification method for the 3D finite deformation model. The material we selected is a Veriflex E thermos-sensitive SMP, which is a commercially available thermosetting polymer. In the 3D finite deformation constitutive model, the material parameters for TTSP and elastic modulus

and relaxation time in each nonequilibrium branch can be determined following the procedure in Second 2.3. The rest parameters include parameters for the thermal expansion, Kuhn segment in the equilibrium branch and the softening parameters in glass branches, which will be introduced in the followings. A detail description can be found in our previous work[10].

4.2.1 Non-linear thermal expansion

The thermal expansion measurement was conducted by using the same tensile setup within the DMA machine. The temperature in the DMA chamber was set to 140 ℃ for 30 minutes to reach thermal equilibrium. To measure the change in the specimen's length during thermal expansion or contraction, a constant and relatively small tensile force of 1×10^{-3} N was applied and maintained by the top grip during the entire experiment. The temperature was decreased from 140 ℃ to 0 ℃ at a rate of 1 ℃/min. After reaching 0 ℃, the temperature was then increased to 140 ℃ at the same rate. This thermal cycle was repeated three times until the experimental curves tended to be stable and only the data from the last cooling step was reported. Figure 4.2 shows the experimental results of the CTE measurement for the temperature range from 0 ℃ to 140 ℃. As shown in the figure, the linear regressions at temperatures above and below T_g were taken to be the respective rubbery and glassy linear CTE values. Here the rubbery linear CTE value was determined to be $_r$ = 2.893x10^{-4}/℃. The structural relaxation parameters were found by fitting the CTE measurement curve through a simulation where a small force as applied to the top surface of the specimen and the temperature was decreased. The detailed parameters identification strategy could be found in Westbrook [1]. The remaining parameters were obtained to be θ = 0.43/℃, x = 0.4 and τ_V = 6.5x10^{-3} s.

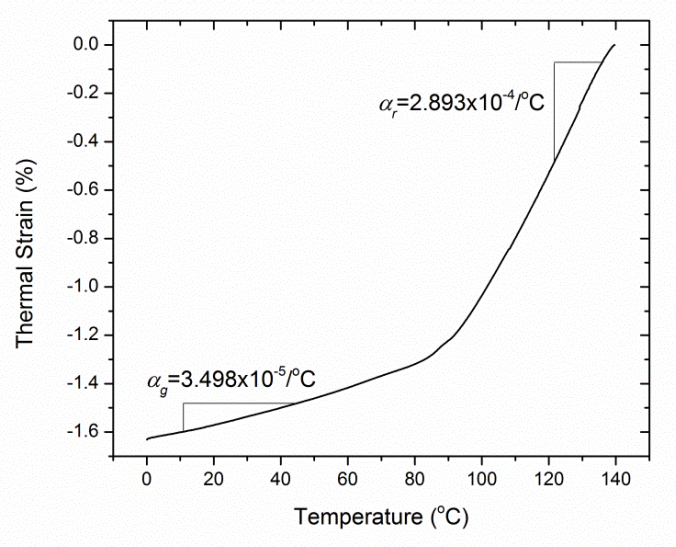

Figure 4.2. Experimental results from the thermal expansion experiments (CTE).

4.2.2 Softening parameters and the Kuhn segment number

To identify the yielding parameters in the glassy branches at different temperatures (25°C, 60°C, 90°C, 100°C 110°C and 130°C), experimental data from McClung et al [11] was used. Details about experimental setup and procedure can be found in McClung. Figure 4.3 shows the stress-strain behavior of the Veriflex E epoxy SMP under various temperatures (plotted as solid lines). The experimental results show that the SMP mechanical response highly depends on the strain rate. Besides, it displays a typical hyperelastic behavior in the rubbery region above T_g and typical glassy behavior below T_g. For temperatures below T_g with increasing strain, a yield point is exhibited followed by a post-yield softening behavior.

The stress-strain curves at temperatures below the glassy transition temperature were used to determine the softening parameters in the glassy branches of the model. Before this, the unsoften stress relaxation times in each glassy branch at these three temperatures (25 °C, 60 °C and 90 °C) were calculated identified by using NLREG and are listed in Table 2. Here, we assume that if the relaxation time is below 0.5s, the corresponding glassy branch contributes insignificantly to the stress-strain behavior. Therefore, the parameters in that branch cannot not be fit. For example, as is shown, at the temperature of 90°C, only the 11th and 12th glassy branches have relaxation times larger than 0.5s. Therefore, only the associated softening parameters in these two branches could be determined by fitting the experimental stress-strain curves in Figure 4.3c. For the

temperature of 60°C, branches from 6th to 12th contribute to the stress-strain curves shown in Figure 4.3b. While keeping the softening parameters unchanged in the 11th and 12th glassy branches, the rest ones (in branches from 6th to 10th) are determined. Similarly, parameters in the 1st to 5th glassy branches are determined by using the experimental curves in Figure 4.3a.

In addition to the softening parameters, the Kuhn segment number of the equilibrium branch N is also identified by using the stress-strain curves in the rubbery region (100 °C, 110 °C and 130 °C). For polymeric materials that in the rubbery state, as the stretch ratio approaches a limiting value $\lambda_c^{\lim}$, the macromolecules are so extended that can no longer accommodate large deformation by rotation[12]. The stress increases dramatically and strain stiffening occurs. From non-Gaussian chain statistics, this limiting stretch ratio $\lambda_c^{\lim}$ is connected to the number of Kuhn segments in the equilibrium branch by $\lambda_c^{\lim} = \sqrt{N}$. From Figure 4.3e and Figure 4.3f, it is observed that this limiting true strain is around 0.9, and hence the Kuhn segment number of the equilibrium branch is determined to be $N = 6.9$.

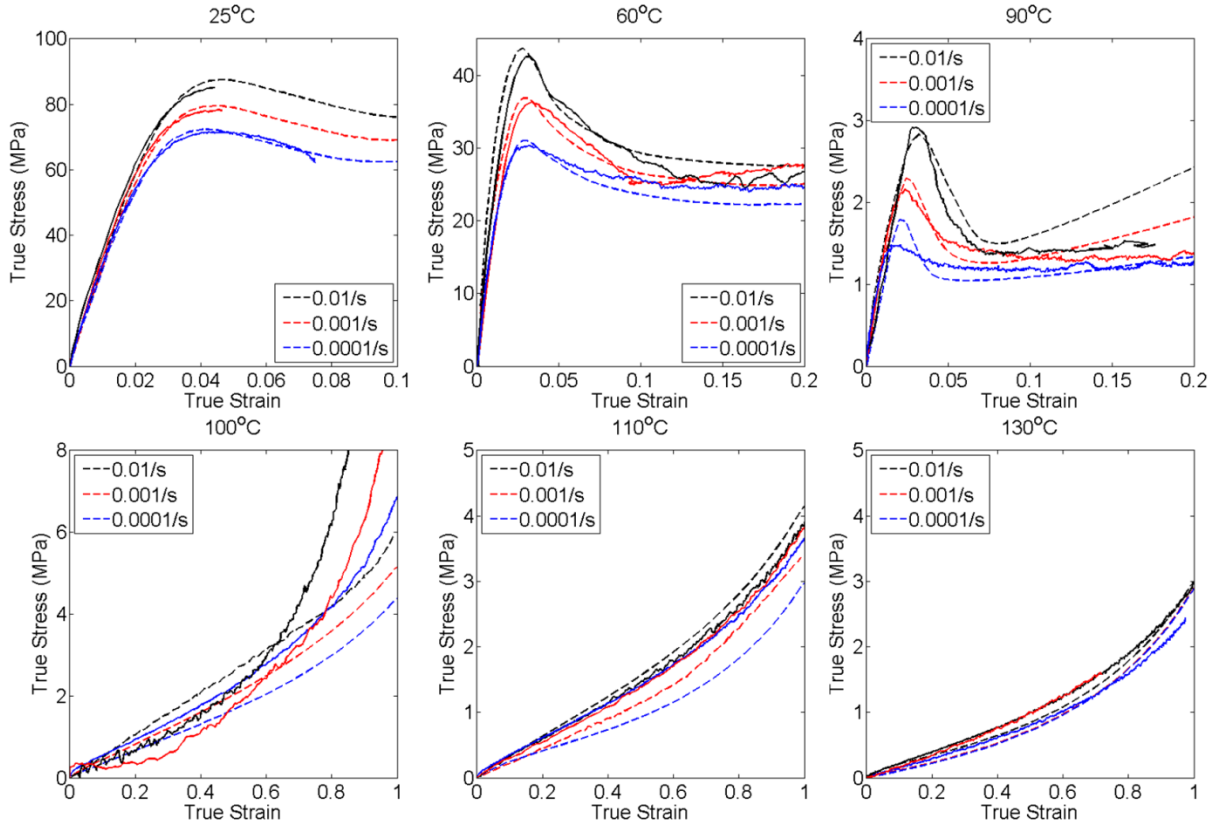

Figure 4.3. Stress-strain behavior of Veriflex E epoxy SMP at different temperatures. (a) 25^{o}C, (b) 60^{o}C, (c) 90^{o}C, (d) 100^{o}C, (e) 110^{o}C and (f) 130^{o}C. Note: Finite simulations are denoted as dash lines and the experimental data is copied from McClung et al[11].

4.3 Applications in the Studying of SMP Composites

In this section, the aforementioned constitutive relations will be incorporated into finite element method (FEM) simulations to investigate the coupling effect of non-uniform temperature filed and stress field on the shape recovery of SMPs and their composite. The constitutive relations are implemented as a user material subroutine (UMAT), and the simulations are performed in the finite element software package ABAQUS (Simulia, Providence, RI). The thermomechanical and shape memory properties of two types of SMP composites will be presented, which is respectively reinforced by magnetic particles and internal microvascular.

4.3.1 Magnetic particles reinforced SMP composites

Recently, efforts have been made to improve the heating rate and shape recovery rate of SMPs by using magnetic particles [13-17]. Magnetic particles in nanometer-size or micrometer-size have been embedded into SMPs to achieve a fast and remote heating of the SMPs after they are exposed to an electromagnetic field. The particles serve as internal mini-antennas to transform the electromagnetic energy to Joule heat through magnetic field induced inductive heating of magnetic particles [17]. This approach offers indispensable advantages for shape recovery of SMPs. For example, heating the material could be achieved remotely. The heating rate of the SMP structures could also be significantly increased since the materials are volumetrically heated and subsequently leaded to a fast actuation. Besides, the inclusions of particles allow for medical imaging techniques, such as fluoroscopy or computed tomography scans, to detect the implanted device without additional surgeries for proper device placement and function [13, 18].

For the FEM simulation of magnetic particle reinforced SMP, it is assumed that the magnetic particles are uniformly distributed within the SMP matrix. A representative volume element (RVE) is then constructed in a 3D setting as shown in Figure 4.4a, where *d* is the diameter of the filler and *2a* is the RVE edge length as shown. Meanwhile, for the convenient of reference in the following discussions, point A is marked on the 3D RVE at one of the farthest points from the magnetic particle heating surface.

The magnetic particles volume fraction ϕ_{3D} can be derived according to the RVE geometry as:

$$\phi_{3D} = \frac{\pi d^3}{48a^3}. \tag{4-15}$$

In the following parametric studies, the magnetic particle diameter is varied over many decades, and the corresponding RVE size under a specified particle volume fraction is calculated according to Eq. 4-15.

Considering that the structure of the 3D RVE under analysis is symmetric, it is therefore feasible to analyze only one eighth of the RVE, with proper thermal and mechanical boundary conditions applied on the sectional surfaces during the modeling. A representative finite element mesh for the 3D RVE is shown in Figure 4.4b for a 1% volume fraction and a filler diameter of 1 *mm*.

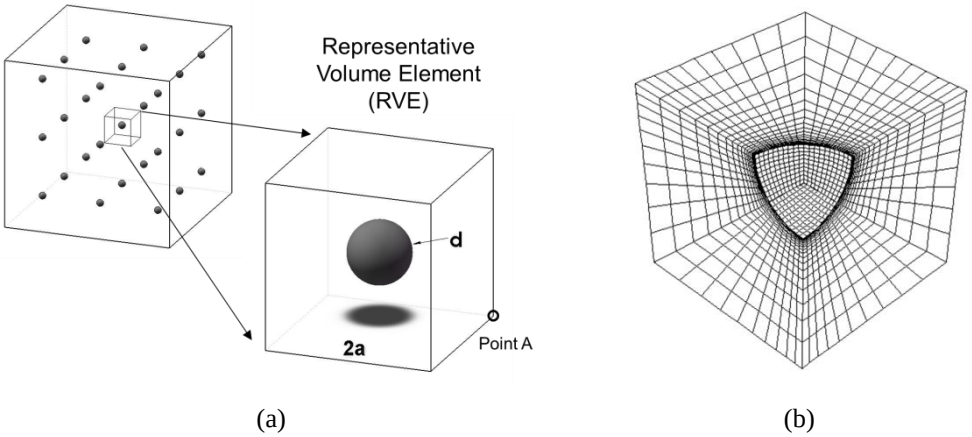

(a) (b)

Figure 4.4. a) The 3D representative volume element (RVE) for a magnetic particles reinforced SMP composite. Note: Point A represents one of the farthest points from the magnetic particle heating surface on the 3D RVE. (b) Finite element model mesh for the 3D RVE for a filler volume fraction of 1% and a filler diameter of 1 *m*m.

The finite deformation analysis of the 3D RVE is coupled with heat transfer by using couple heat-displacement analysis in ABAQUS. A detailed description on the model parameters, simulation procedure and element selection can be found in our previous work[19]. In our study, the modeling of magnetic particle is not considered to simplify the analysis, and the particle heating effect, as represented by temperature boundary condition, is applied directly on the curved surface of 3D RVE.

The total time for the shape recovery of a SMP magnetic particle composite is determined by the times for temperature rise in particles to the targeted temperature, for heat transfer from the particles to the SMP, and for the SMP matrix to recovery. In this study, the focus will be on the heat transfer and matrix recovery. Therefore, unless otherwise mentioned, we assume that the particles can be heated to the targeted temperatures instantaneously. In the finite element model, this was achieved by ramping the temperature of the nodes on the intersurface between magnetic particle and SMP matrix to the target recovery temperature (50^{o}C) in 0.1 milliseconds in the recovery step.

As a representative case, the particle volume fraction is selected as 1% and the particle diameter is 400 *mm*. During the programming process, the loading rate and the cooling rate were set as 0.01/s and 1.67 ^{o}C/min respectively, while the total compressive strain was 0.2. The time for a full shape recovery is taken to be when the strain recovery ratio reaches 95%.

Figure 4.5 shows the Mises stress distribution within the 3D RVE during the shape memory cycle, where the maximal and minimal limits of the contours are fixed for the convenient of comparison. As expected, the maxima of Mises stress is always located on the interface between the particle and SMP matrix. It is also noted that within the first 7.2s of the particle heating, no noticeable strain recovery is observed. The phenomenon could also be reflected in Figure 4.6, where the temperature is collected on point A on the 3D RVE. During this time period, heat transfer within the material dominates the shape recovery process, and significant shape recovery behavior would not be triggered only after the average temperature of SMP matrix is ramped above a critical value. Detailed study on the onset temperature of shape recovery will be presented in the following section. When the thermal transmission within the 3D RVE is basically finished, the shape recovery in the SMP material is triggered, with the Mises stress decreasing gradually. At t=14.7s, the strain recovery ratio reaches 95%. And after 20s, the permanent shape of the 3D RVE is totally recovered.

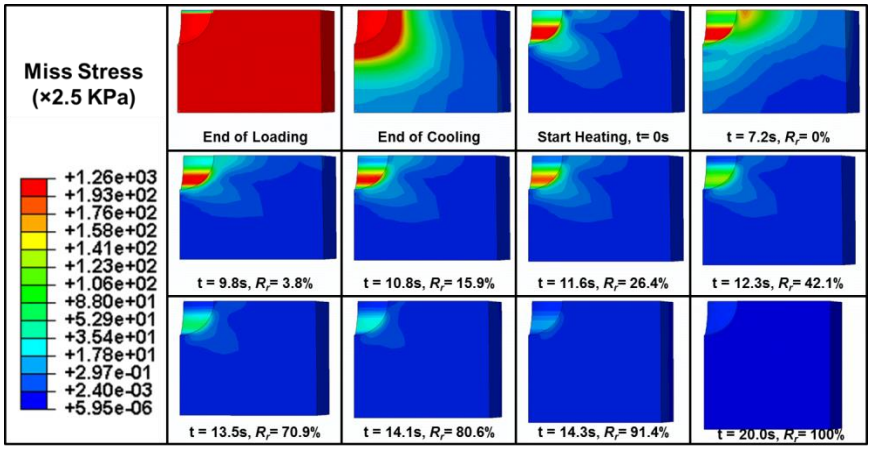

Figure 4.5. Mises stress distribution within the 3D RVE during the finite element analysis

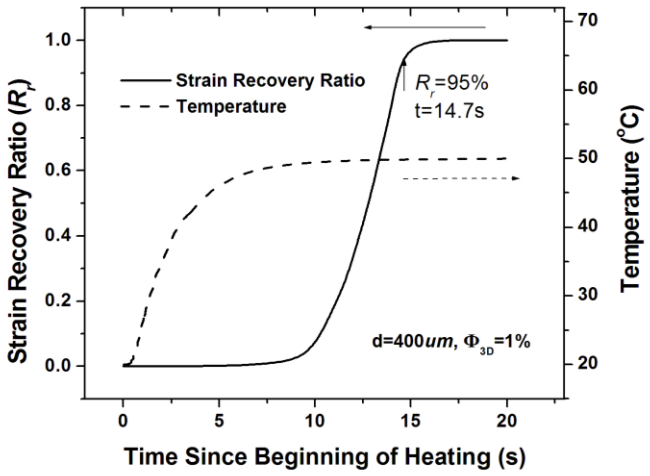

Figure 4.6. The strain recovery ratio and temperature of the 3D RVE during the free recovery process. Note: temperature data is collected on point A on the 3D RVE

The temperature distributions within the 3D RVE are plotted as contours in Figure 4.7. Within the first 7.2s since the beginning of particle heating, thermal energy is transferred to from the particle surface to the outer boundaries of RVE. The temperature decreases along the thermal conductive pathways. Since the modulus of SMP is very sensitive to temperatures, the material near the outer surface has a much higher modulus than the material inside and therefore confines the material inside. This confinement has two encasing effects. First, shape recovery does not occur until the temperature on the outer surface of the RVE is high such that the deformation of the material on the outer surface starts to recovery. Therefore, the shape recovery rate is dominated by the recovery of the material at the RVE boundaries. Second, the volume expansion of the material inside the RVE is hindered, leading to a high hydraulic pressure developed

around the particle-matrix interface. This phenomenon could be visualized in Figure 4.8 where the hydraulic pressure evolution is described on the curved surface of 3D RVE during the free recovery process. Finally, when the shape recovery process is finished, the internal hydraulic pressure is completely released.

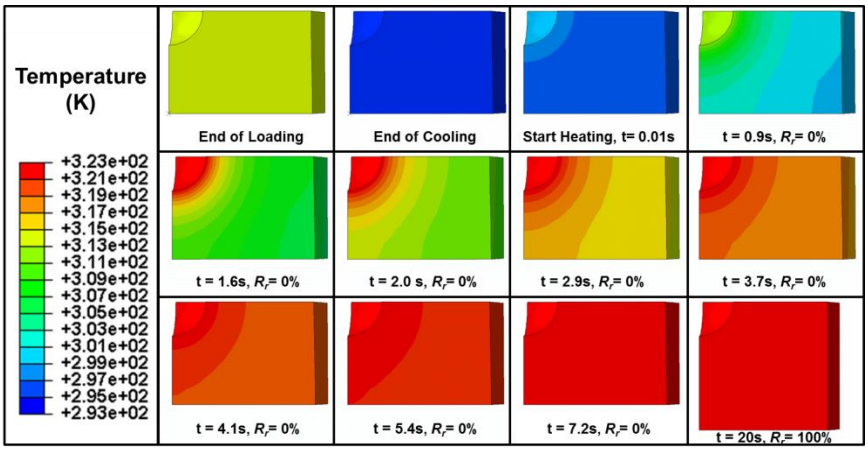

Figure 4.7. Temperature distribution within the 3D RVE during the finite element analysis.

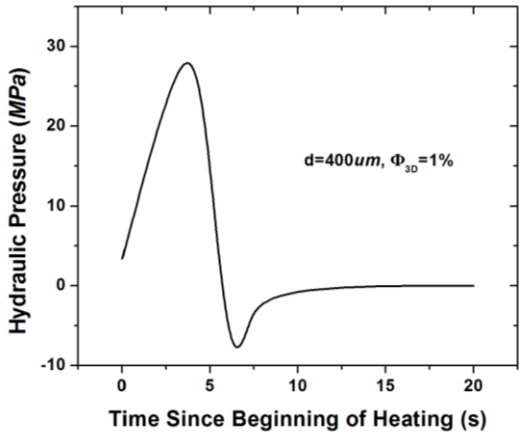

Figure 4.8. Hydraulic pressure evolution on the curved surface of 3D RVE during the particle heating process

Under the instantaneous particle heating condition and four particle volume fractions (0.001%, 0.1 %, 1 % and 10%) loaded, Figure 4.9 demonstrates the effects of changing the particle diameter on the shape recovery time of the SMP composites. As shown in the figure, for each curve with different particle heating temperature and volume fraction, a critical diameter is observed, below which the time for full recovery is independent of the particle diameter. The critical diameters for the 0.001%, 0.1 %, 1 % and 10% volume fractions are approximately 0.15mm, 1.7 mm, 7 mm and 80 mm for recoveries at 50 ℃,

and 0.8mm, 13 mm, 40 mm and 200 mm for recoveries at 40℃, respectively. The existence of the critical particle diameters could be well explained by the previous discussions, and is considered to represent a threshold of recovery from one dominated by heat transfer to one dominated by material intrinsic recovery. At a specified particle volume fraction, the 3D RVE size would be decreased along with the decrease of particle diameter, and thus the shape recovery time is effectively reduced as a result of the reduction of pathway length for heat transfer. Below the critical filler size, the size of the 3D RVE becomes unimportant as heating can occur almost instantaneously and therefore from heating efficiency and material recovery points of view, it is unnecessary to further reduce the particle diameter. Even though small sized particles could be easily suspended in solution than large particles, and hence might be preferred during the polymer composite synthesis, excessively reducing the particle diameter, especially into ones of nanometers, would oppositely lead to particle aggregates due to the strong attractive Van Der Waal force among them. Therefore, it should be avoided to facilitate a uniform dispersion of the reinforcement particles within the polymer matrix.

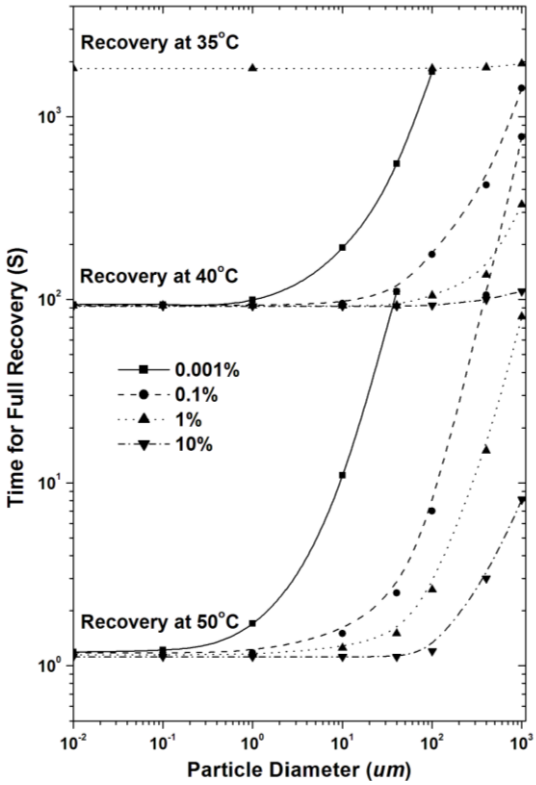

Figure 4.9. Prediction of critical particle diameters by showing effect of particle size on shape recovery time of the SMP composites

4.3.2 Microvascular reinforced SMP composites

Recently, a microvascular embedded SMP composite was designed and implemented by Phillips et al.[20], where internal microvascular channels and flowing heat exchange fluid were used as an energy transport mechanism to thermally activate and deactivate the SMP matrix. By using this method, rapid heating and cooling of the SMP material was achieved. The highest temperature was controlled by the fluid inlet temperature, and local overheating was therefore avoided.

In the experiments of Phillips *et al*. [20], stainless steel tubes (OD=203*um*; ID=102*um*) were selected as internal microvascular passages. During the experiments, compressed 110^{o}C hot water was injected into ten internal microvascular passages at 25 ml/min total (2.5 ml/min for each passage or ~5100mm/s) to thermally actuate the SMP matrix. Primary 3D fluid-structure (FS) simulation (see APPENDIX B at the end of this chapter for details) revealed that under such a high flow rate of the hot water, the temperatures on the inlet and outlet surfaces of the microvascular system can be synchronized within 0.3s up to 105.8^{o}C and then ramp slowly towards the target heating temperature (110^{o}C). Since a full 3D FS simulation that couples shape change with heat transfer is extremely time consuming in ABAQUS, a 2D model is used in this study for simplification. During the thermal actuation of the SMP composite, the temperature of the tube surface is linearly ramped to the target temperature in 0.3s to represent the fast heating effect from the internal microvascular system. The 2D geometry of the microvascular composite system is demonstrated in Figure 4.10b, it is assumed that the stainless steel tubes are uniformly distributed within the SMP matrix, where the tube spacing is *L* and the composite thickness is *B*. The finite element meshing results is shown in Figure 4.10c.

Since the structure of the SMP composite under analysis is symmetric, it is feasible to analyze only a half-size periodic model, with proper thermal and mechanical boundary conditions applied on the sectional surfaces. In the experiments, the upper composite surface is open to the ambient, while the bottom surface rests on a fiberglass insulation sheet. Therefore, the "natural convection" condition is applied to the top surface in the model. The exchange of heat on the surface is dependent on both the polymer surface

temperature T and ambient temperature T_0 : $q = h(T - T_0)$, where q is the heat flux per unit area across the surface, h is the heat transfer coefficient. The insulating condition is applied to the other surfaces of the model. Relevant physical properties of the stainless steel microvasculature are listed in Table 4-1. Four reference points (Figure 4.10c) are marked on the model surfaces for the following studies.

In the representative simulation case, the tube spacing L is set to be 3.6mm, while the overall thickness B is 1.71mm, which are the same as those in the referenced experiments [20]. During the SM cycle, the half-size periodic model is first stretched by 20% at 110°C. After the temporary shape is fixed at 25°C, hot fluid is delivered at 110°C (2.5 ml/min per passage) to activate the SMP composite for free shape recovery. Other simulation procedure and setup can be found in our previous work[21].

Table 4-1. Physical properties of the 316 stainless steel microvascular tubes

Density (kg/m^3)	Elastic Modulus (GPa)	Thermal Expansion Coefficient (μm/m/℃)	Thermal Conductivity (W/m.K)	Specific Heat (J/kg.K)
7850	193	15.9	16.3	500

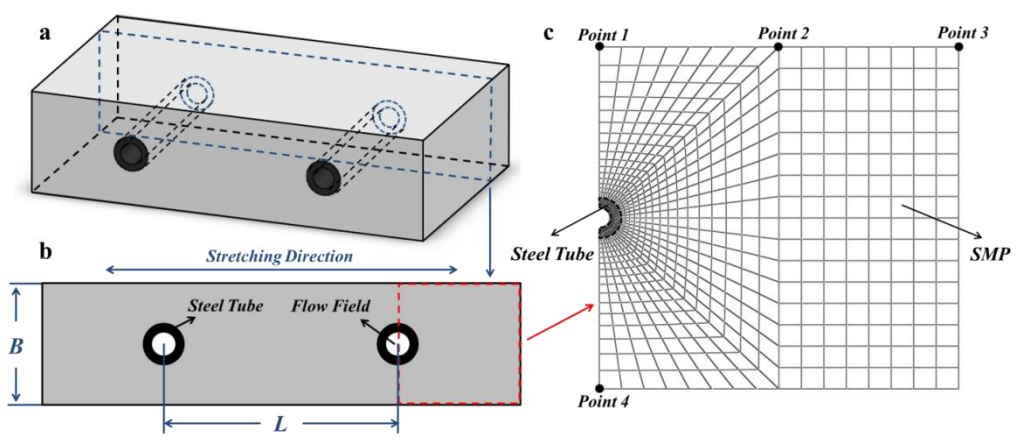

Figure 4.10. Modeling method of the SMP composite in ABAQUS. (a) A representative microvascular SMP composite in the 3D setting. (b) A cross-sectional view of the 3D model. (c) The finite element meshing result with temperature reference points.

In Figure 4.11, the simulated shape recovery ratio of the SMP composite in the stretching direction and the temperature evolution on Point 1 are respectively plotted and compared with the experimental data. It should be noted that the temperature on Point 1 is actually the maximum temperature on the top surface of the SMP composite. The finite element simulation results matched the experimental observations, indicating that by

using the 3D finite element model, together with predetermined model parameters, the thermal conduction, temperature evolution and the overall material shape recovery behavior are successfully reproduced.

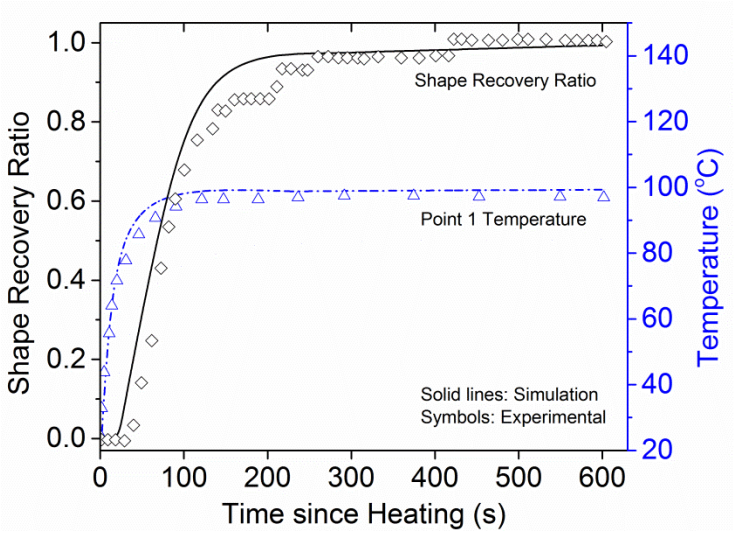

Figure 4.11. Comparisons between the simulation and experiments. The shape recovery ratio is captured on Point 3 in the stretching direction

Figure 4.12 shows the temperature distribution within the half-size periodic model during the SM cycle. It can be seen that the free shape recovery behavior of the SMP composite is successively dominated by two thermomechanical processes: the initial thermal conduction and thermally induced shape recovery. After the hot fluid is injected into the microvascular channels, thermal energy is gradually transferred from the tube surface to the outside of the half-size periodic model, and the SMP material near the tube surface would firstly reach T_g and then recover. However, such a recovery would be restricted by the outer surface of the composite material with higher modulus until about 10-20s when the surface temperature becomes high enough to allow for recovery. After that, shape recovery is successively initiated along the stretching direction of the SMP composite. Figure 4.13 further shows the temperature evolution of Points 1-3 on the top surface of the model as a function of heating time, as well as the corresponding shape recovery ratios in the thickness direction and in the stretching direction (R_r). It is seen that after about 20s, the temperature of Point 1 is ramped to 72^{o}C and Point 1 starts to recover in both stretching and vertical directions. Additionally, noticeable shape recoveries on Point 2 and 3 are also shown to start when the local temperature reaches around 72^{o}C. The two underlying mechanisms, which are the thermal conduction and the

material intrinsic shape recovery that successively dominate the entire thermal process, are similar to our previous studies on magnetic particle reinforced SMP composites [19].

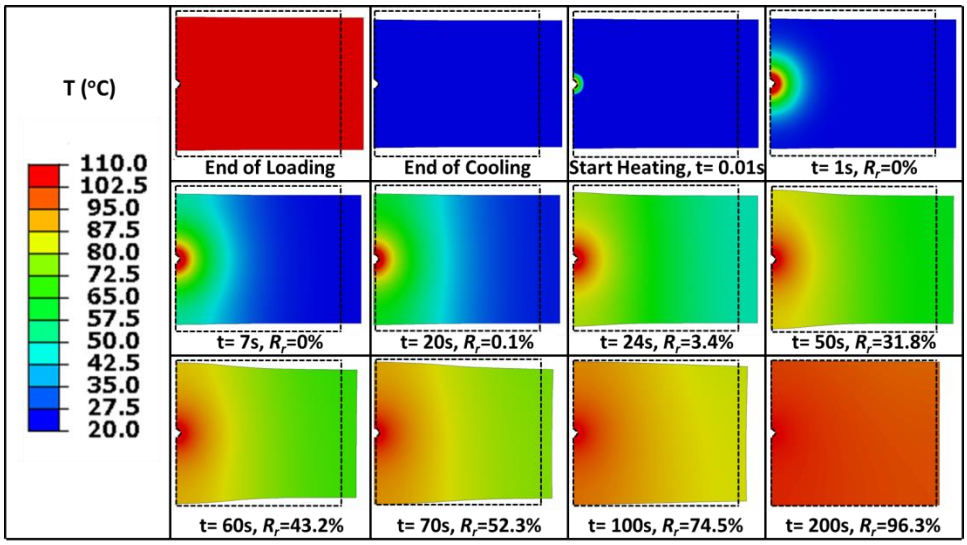

Figure 4.12. Temperature distribution within the half-size periodic model during the shape memory cycle. Note: the dash boxes indicate the initial size of the periodic model without defamation.

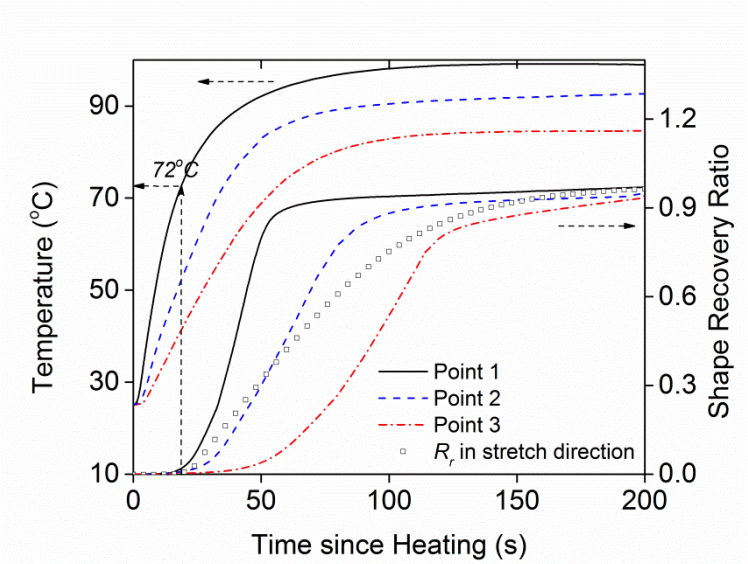

Figure 4.13. Evolution of temperature and shape recovery ratio on Point 1, Point 2 and Point 3 respectively, as well as the shape recovery ratio of the model in the stretching direction (R_r). Note: the shape recovery ratios on Point 1, Point 2 and Point 3 are collected in the thickness direction.

To achieve an optimized structure of the microvascular SMP composites, the tube arrangement is an important design parameter because it will influence the density of the composite materials as well as the system complexity. Figure 4.14 demonstrates the effects of changing the composite thickness and tube spacing on the material density and

total shape recovery time of the SMP composites. Here, the density of the composite material is calculated based on the volume fraction and density of the SMP and stainless steel microvasculature, respectively. As shown in the figure, a critical space is observed for each curve with different composite thickness, below which the time for full recovery is independent of the tube spacing. The critical tube spacing for thicknesses of $1/2B_0$ (0.855mm), B_0 (1.71mm) and $2B_0$ (3.42mm) are approximately 16mm, 8mm and 4mm, respectively. The existence of the critical tube spacing could be well explained by the previous discussions and represents a threshold for the recovery mechanism from one dominated by heat transfer from the tube surface to Point 1 to one dominated by the successive shape recovery of the SMP composite along the straining direction. When the tube spacing is above the corresponding critical values, reducing the composite thickness and tube spacing is meaningful as it will significantly reduce the total shape recovery time without greatly affecting the material density. However, when below the critical tube spacing, the shape recovery in the straining direction can occur almost instantaneously. Therefore from thermal efficiency and material recovery points of view, it is unnecessary to further reduce the tube spacing. Excessively reducing the tube spacing would lead to a tight arrangement of the microvasculature inside of the SMP matrix and subsequently increases the density of the SMP composite, which is unwanted in many engineering applications, such as aerospace and aeronautics. Besides, it will also increase the system complexity even if other light weighted microvascular are substituted as the reinforcement. In a practical application of such SMP composites embedded with microvasculature, the optimized design should combine the considerations on material loading capacity, composite weight requirement, system complexity and material thermal responsiveness.

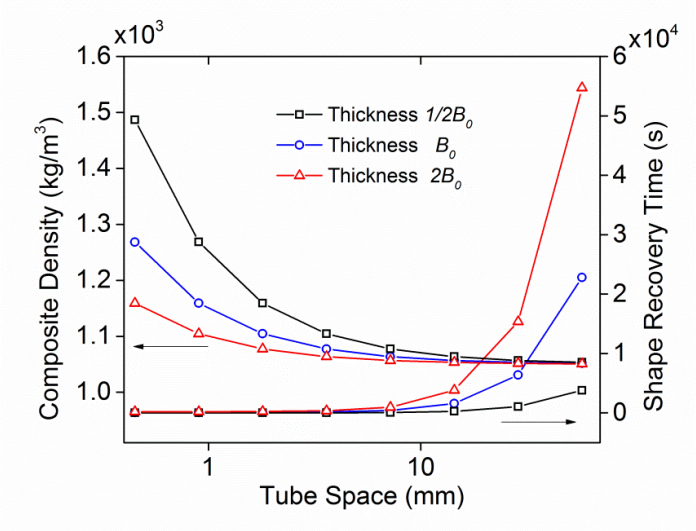

Figure 4.14. Density and total shape recovery times of the SMP composite under different tube spaces and composite thickness.

For the SMP composite considered in this study, the asymmetric boundary conditions on the top and bottom surfaces lead to an optimal tube arrangement within the SMP matrix that might also affect the thermal response of the system by changing the internal conductive pathways. Previous discussions revealed that shape recovery in the SMP composite will not initiate until the temperature on the outer surface exceeds the required minimum. Therefore, the temperature evolution on the composite surface plays a critical role in determining the total shape recovery time. Figure 4.15a shows the changes of temperature on points 1 and 4 as a function of microvascular heating time. The composite thickness is increased from 1/4 B_0 to 20 B_0 while the rest model dimensions and simulation parameters are the same as the representative case. Because the top surface of the SMP composite is exposed to the ambient while the remaining surfaces are thermally insulated, the temperature variation on the top surface is seen to be delayed due to the heat convection, and such a delay is intensified when the composite thickness is increased. The local heat lost also leads to an equilibrium temperature that is lower than the target heating temperature (110^{o}C). These two effects can impair the shape recovery speed of the SMP composite. To optimize the tube arrangement, an intrinsic conjecture is that the tubes should be arranged closer to the top surface. A parametric study is conducted accordingly where the tube position is gradually shifted in the thickness direction towards the top surface. The associated shape recovery time $t_{0.95}$ is plotted in

Figure 4.15b as a function of tube location for different composite thicknesses ($1/2B_0$, B_0, $4B_0$, $10B_0$ and $20B_0$). Each data point is normalized by the initial value ($t^0_{0.95}$, tube depth=0.5B) to assist the visualization.

As shown in the figure, when the location of tube center is gradually moved towards the top surface, an optimized tube location is revealed with the minimized shape recovery time on each curve. For the ½ B_0 case, the optimized location is located at ½ B. The variation of the shape recovery time could be explained as follows. Initially moving the tube upward will increase the temperature ramp rate and final equilibrium temperature on the top surface, which accelerates the activation of the entire cross-section and subsequently increases the overall shape recovery speed. After the optimized tube location is reached, further moving the tube will delay the temperature ramping on the bottom surface. An optimized location requires a balance between these two competitions, namely a synchronous temperature variation as well as higher equilibrium temperature on both top and bottom surfaces. Besides, Figure 4.15b also shows that the optimization effect from adjusting the tube location is more obvious when the composite thickness is high. If the composite thickness is only $1/2B_0$, changing the tube depth is unnecessary because the temperature variations on top and bottom surfaces are almost synchronous (see Figure 4.15a). However for the case of $20B_0$ thickness, the shape recovery speed is improved by 29% when the tube depth is rearranged from 0.5B to 0.379B.

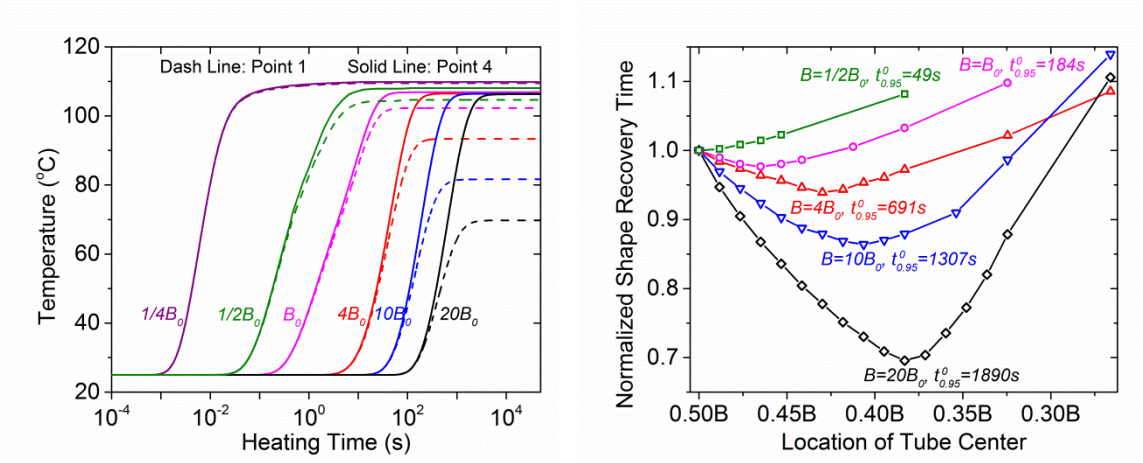

Figure 4.15. (a) Temperature variation on Points 1 and 4 as a function heating time and composite thickness. (b) Normalized shape recovery time plot as a function of location of tube center

(measure from the top surface) and composite thickness. Note: for each curve, the data points are normalized by the initial value, namely the shape recovery time when the tube depth is 0.5B

4.4 Conclusion

In this chapter, we firstly extended the 1D thermoviscoelastic constitutive relations into a 3D finite deformation constitutive model, which can be used to capture the general thermomechanical properties of amorphous polymers in addition to the shape memory behavior, such as nonlinear thermal expansion, non-linear deformation of rubbery polymer, yielding and post-yielding softening behavior of glassy polymers. A protocol to determine the complete set of model parameters is also introduced and deemed effective in predicting the SMP thermomechanical behavior.

Based on the 3D finite deformation model, finite element method (FEM) simulation was conducted to characterize the coupling effect of non-uniform temperature filed and stress field on the shape recovery of SMPs composite. Two types of SMP composites were investigated, which is respectively reinforced by magnetic particles and internal microvascular. Computationally studies revealed similar thermomechanical and shape memory properties in these two composite systems, namely the initial thermal conduction and thermally induced shape recovery successively dominate the total shape recovery process. Besides, parametric studies revealed some considerations should be followed in the practical designs of the composite materials.

Specifically, for the magnetic SMP composites, reducing particle sizes or increase volume fractions can promote faster recovery rate. However, it was found that for a given target recovery temperature and a given particle volume fraction, there exists a critical particle size. For particle smaller than this critical size, the recovery time is dominated by the material intrinsic recovery time and is therefore independent of particle size. Similarly, for a given particle size and target recovery temperature, there exists a critical volume fraction. Above this volume fraction, further increasing volume fraction does not improve the heating efficiency. For the microvascular reinforced SMP composite, a critical tube spacing was demonstrated for a given composite thickness, below which further decreasing the tube spacing is unnecessary for the improvement of the shape-recovery rate and increases the composite density. In addition, the tube location within

the SMP matrix should also be adjusted appropriately according to the thermal boundary conditions where thicker composites have an optimal tube placement closer to the non-insulated surface. The results in this chapter provide a meaningful guidance for further designs and applications of the composite materials that rely on internal heating source to volumetrically heat up the matrix SMP.

Appendix B: 3D Fluid-Structure (FS) Simulation on the Microvascular SMP Composite

Here, to simulate the real thermal conduction behavior within the microvascular reinforced SMP composite, a 3D dimensional model accompanied with full fluid-structure (FS) analysis capability is constructed in ABAQUS. The geometry of the composite system is illustrated in Fig. B1, where the composite width is set to be 146mm. Other dimensions are the same as that in the 2D model discussed in the main text of Chapter 4. For simplification, only one eighth of the periodic unit is modeled. The ambient temperature is set as 25^{o}C. Two reference paths (Path 1-2) that have the same length as the microvascular are marked on the model for further denotation. Path 1 is actually located on the out surface of the microvascular, and Path 2 is within the SMP matrix. During the simulation, hot fluid at 110^{o}C is injected into the tube at 25ml/min.

The temperature evolution on Path 1 and Path 2 within the first 6s since hot fluid is injected is shown in Fig. B2. Since the flowing distance per second (~5000mm) is quite large in comparison with the tube length (146mm), temperature on Path 1 ramps very fast, and within 0.3s, the temperature variation on the entire path tends to be synchronous. While for Path 2, the temperature is gradually increased due to the thermal conduction, but the variation along the path is nearly synchronous from the very beginning of heating. Considering the timing scale for the total thermal conduction and shape recovery process of the SMP composite (up to hundreds of seconds), it is reasonable to disregard the difference in temperature evolution on the inlet and outlet surfaces of the 3D model, and use a 2D model in Chapter 4 for simplification.

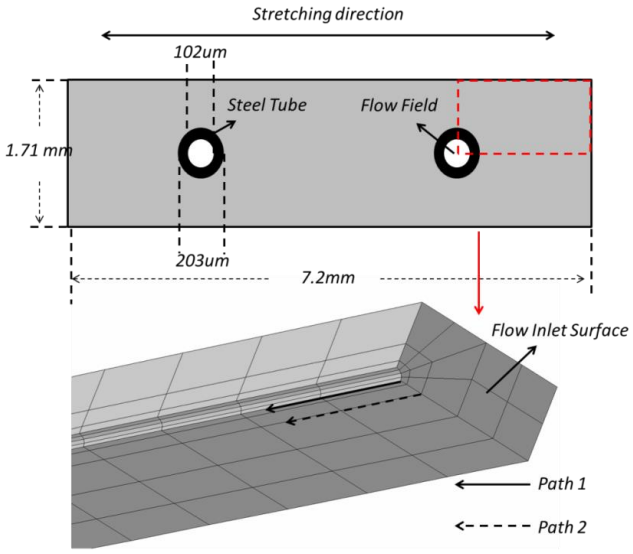

Figure B1. Modeling method in ABAQUS in the 3D setting. Top view illustrates the dimension of a representative microvascular SMP composite. Bottom view shows the finite element model mesh result

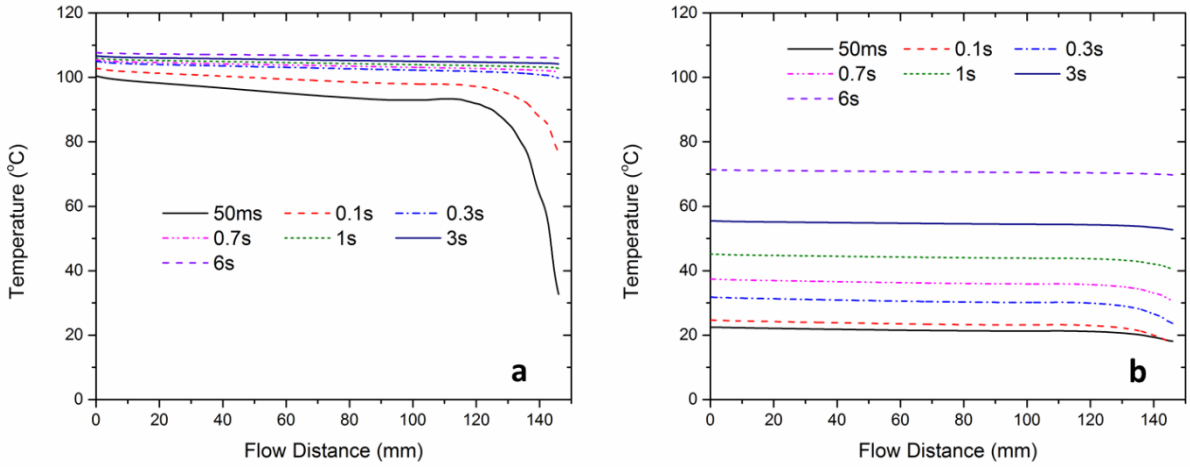

Figure B2. Temperature evolution on (a) Path 1 and (b) Path 2 within the first 6s since hot fluid is injected into the microvascular.

4.5 References

1. Westbrook, K.K., et al., *A 3D finite deformation constitutive model for amorphous shape memory polymers: A multi-branch modeling approach for nonequilibrium relaxation processes.* Mechanics of Materials, 2011. **43**(12): p. 853-869.
2. Holzapfel, G.A., *Nonlinear solid mechanics: a continuum approach for engineering*. 2000, New York: Wiley, Chichester.
3. Tool, A.Q., *Relation between Inelastic Deformability and Thermal Expansion of Glass in Its Annealing Range.* Journal of the American Ceramic Society, 1946. **29**(9): p. 240-253.

4. Tool, A.Q., *Effect of Heat-Treatment on the Density and Constitution of High-Silica Glasses of the Borosilicate Type.* Journal of the American Ceramic Society, 1948. **31**(7): p. 177-186.
5. Tool, A.Q. and C.G. Eichlin, *Variations caused in the heating curves of glass by heat treatment.* Journal of the American Ceramic Society, 1931. **14**(4): p. 276-308.
6. Kovacs, A.J., et al., *Isobaric volume and enthalpy recovery of glasses. II. A transparent multiparameter theory.* Journal of Polymer Science, Polymer Physics Edition, 1979. **17**(7): p. 1097-1062.
7. Arruda, E.M. and M.C. Boyce, *A 3-Dimensional Constitutive Model for the Large Stretch Behavior of Rubber Elastic-Materials.* Journal of the Mechanics and Physics of Solids, 1993. **41**(2): p. 389-412.
8. Rubinstein, M. and R.H. Colby, *Polymer physics*. 2003, New York: Oxford University Press, Oxford.
9. Treloar, L.R.G., *The physics of rubber elasticity*. 2d ed. Monographs on the physics and chemistry of materials. 1958, Oxford: Clarendon Press. 342 p.
10. Yu, K., et al., *A thermomechanical constitutive model for an epoxy based shape memory polymer and its parameter identifications.* Mechanics of Time-Dependent Materials, 2014. **18**(2): p. 453-474.
11. McClung, A., G. Tandon, and J.W. Baur, *Deformation rate-, hold time-, and cycle-dependent shape-memory performance of Veriflex-E resin.* Mechanics of Time-Dependent Materials, 2013. Available online.
12. Qi, H.J., K. Joyce, and M.C. Boyce, *Durometer hardness and the stress-strain behavior of elastomeric materials.* Rubber Chemistry and Technology, 2003. **76**(2): p. 419-435.
13. Buckley, P.R., et al., *Inductively heated shape memory polymer for the magnetic actuation of medical devices.* Ieee Transactions on Biomedical Engineering, 2006. **53**(10): p. 2075-2083.
14. Mohr, R., et al., *Initiation of shape-memory effect by inductive heating of magnetic nanoparticles in thermoplastic polymers.* Proceedings of the National Academy of Sciences of the United States of America, 2006. **103**(10): p. 3540-3545.
15. Razzaq, M.Y., et al., *Thermal, electrical and magnetic studies of magnetite filled polyurethane shape memory polymers.* Materials Science and Engineering a-Structural Materials Properties Microstructure and Processing, 2007. **444**(1-2): p. 227-235.
16. Nikitin, L.V., et al., *Magnetodeformational effect and effect of shape memory in magnetoelastics.* Journal of Magnetism and Magnetic Materials, 2004. **272**: p. 2072-2073.
17. Weigel, T., R. Mohr, and A. Lendlein, *Investigation of parameters to achieve temperatures required to initiate the shape-memory effect of magnetic nanocomposites by inductive heating.* Smart Materials & Structures, 2009. **18**(2).
18. Yakacki, C.M., et al., *Shape-Memory Polymer Networks with Fe3O4 Nanoparticles for Remote Activation.* Journal of Applied Polymer Science, 2009. **112**(5): p. 3166-3176.
19. Yu, K., et al., *Design considerations for shape memory polymer composites with magnetic particles.* Journal of Composite Materials, 2013. **47**(1): p. 51-63.

20. Phillips, D.M. and J.W. Baur, *A microvascular method for thermal activation and deactivation of shape memory polymers.* Journal of Intelligent Material Systems and Structures, 2013. **24**(10): p. 1233-1244.
21. Yu k., et al., *Analysis of shape-memory polymer composites with embedded microvascular system for fast thermal response.* Journal of Composite Materials, 2014. DOI: 10.1177/0021998314540194 (availabe online).

CHAPTER 5

COVALENT ADAPTIVE NETWORKS WITH BOND EXCHANGE REACTIONS

Historically, thermosetting polymers with covalent crosslinks have been known as permanent, infusible and insoluble networks [1]. These polymers are ideal for various structure and composite material applications ranging from aircraft and automotive components to surface coatings and adhesives; however, their reprocessability are limited by the permanently crosslinked structure [2], which increasingly becomes an environmental concern as recycling or reusing them are either very challenge or very cost ineffective.

This historical picture of thermosetting polymers has been changed by recent advances in covalent chemistry, where specific functional groups capable of reversible chemical reactions are integrated into the polymer chains [3-16]. These functional groups can break and reform the thermosetting network, and consequently render it adaptiveness upon stimuli. Various chemical reactions can be utilized to achieve the bond exchanging and network adaptiveness. For example, the well-established Diels-Alder reaction [17-20] between diene and dienophile groups can be thermally triggered, and displace the thermosetting polymer from equilibrium toward deploymerization upon heating. Recently, Montarnal et al [5] developed adaptive epoxy thermoset based on transesterfication exchange reactions at high temperature, which enables the topology rearrangement of network and avoids impairing the network integrity. Other covalent adaptive reactions in this realm include amino carbonyl reaction [21-23], siloxane equilibration [3], and photo-sensitive radicals to initiate exchange reaction and malleability in thermosets [24-26].

Existing methods to achieve an CAN generally provide merits in combining the malleability of bulk material with the surface welding effect when desired polymer parts are brought into contact, leading to the self-healing [7, 18, 22, 24, 27], reprocessing and recycling of thermosetting polymers [5, 27-29]. In this chapter, we firstly examine the

malleability, reprocessing and recycling capability of such CAN, while the interfacial mechanics during welding effect will be introduced in the next chapter.

5.1 Material

In our study, the CAN with exchangeable bonds was prepared following the method used by Montarnal and coworkers[5], where the thermally induced BERs are based on the transesterfication exchange reactions. The reason for us to select this polymer system is that it provides unique advantages for the practical engineering applications: During the transesterfication reactions, the polymer viscosity is gradually changed versus temperature following an Arrhenius law during the operation, and hence the network integrity is maintained. In addition, since no additional monomers or termination reactions are introduced into the system, the numbers of links and average functionality of polymer chains is unchanged.

In Montarnal's work [5], two types of such CANs (i.e. the soft and hard networks) were prepared by using different monomers, namely the diglycidyl ether of bisphenol (DGEBA) and glutaric anhydride. Here we follow the same synthesis procedure. In addition, we also change the stoichiometry by mixing these two monomers at different ratios to examine its influence on the material thermomechanical properties and BER kinetics.

The monomers DGEBA, glutaric anhydride and the metal catalyst ($Zn(Ac)_2$) were ordered from Sigma Aldrich (St. Louis, MO, USA) and used as received without further purification. The mixture of fatty acid monomers (Pripol 1040) was kindly provided by Uniqema Inc (Paterson, NJ, USA). Detailed chemical structures of each used reagent are shown in Figure 1. Five groups of epoxy polymer were prepared in this study. The ratio of epoxy group and metal catalyst are unchanged in each epoxy network (1:0.05), while the fatty acid and glutaric anhydride are mixed with different ratios. The stoichiometry of the five epoxy polymers is listed in Table 5-1. The total amount of the carboxylic acid and acyl groups in these two monomers is equal to the stoichiometry of epoxy group.

All the epoxy materials with different composition were prepared following the same procedure. In Step 1, the catalyst was mixed with fatty acids and glutaric anhydride with specified ratios in a round-bottom flask and stirred at 130 ℃ until homogeneous mixing

was achieved. In Step 2, DGEBA in solid state was heated up to 130 ℃ until totally melted, and then manually stirred with the solvent in Step 1 at 130 ℃ until the mixture became homogeneous and translucent. In Step 3 the mixture in step 2 was poured into a PTFE mold, and covered with a PTFE lid, and placed in an oven under a 500 g weight for 6 h at 130 ℃. Figure 5.1 also depicts the repeating unit of the chemical reactants within the thermoset network, where the fatty acid linker and glutaric anhydride linkers respectively are the reaction derivatives from epoxy/fatty acid reaction and epoxy/glutaric anhydride reaction.

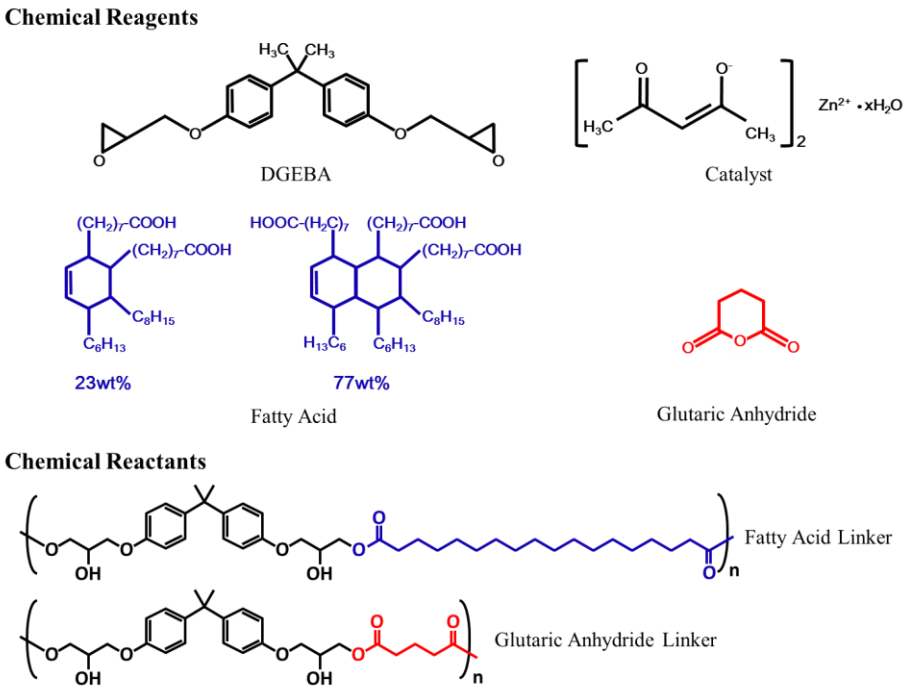

Figure 5.1. Schematic view of the chemical reagents used in this study, as well as the reactant repeating unit after synthesis.

Table 5-1. Stoichiometry (normalized mole content) of each composition

	Epoxy group (in DGEBA)	Catalyst ($Zn(Ac)_2$)	Acid group (in fatty acid)	Acyl group (in glutaric anhydride)	T_g
Epoxy 1	1	0.05	1	0	30.3 °C
Epoxy 2	1	0.05	0.5	0.5	38.4 °C
Epoxy 3	1	0.05	0.4	0.6	43.3 °C
Epoxy 4	1	0.05	0.2	0.8	55.7 °C
Epoxy 5	1	0.05	0	1	63.0 °C

5.2 Glass Transition Behavior

The glass transition and stress relaxation behavior of the prepared epoxy thermosetting networks were tested on the DMA tester (Model Q800, TA Instruments, New Castle, DE, USA). For the test of glass transition behavior, polymer sheets with the dimension of 10mm × 5mm × 1mm were tested on the tensile mode. During the experiment, the strain was oscillated at a frequency of 1 Hz with a peak-to-peak amplitude of 0.1% while the temperature was decreased from 100 ℃ to -10 ℃ at a rate of 1 ℃/min. Once the temperature reached -10 ℃, it was maintained for 30 minutes and then increased to 120 ℃ at the same rate. This procedure was repeated multiple times and the data from the last cooling step is reported. Figure 5.2 compares the DMA testing results and the glass transition behavior of the five epoxy thermosets. Figure 5.2a shows that as the ratio of anhydride hard linkers increases from 0 to 1, the T_g increases from 30.3 ^{o}C to 63.0 ^{o}C. Additionally, the tan δ curve becomes wider but decreases in height. Figure 5.2b plots the storage modulus curves of each sample as a function of temperature. The material glass modulus (initial modulus on each curve) and rubbery modulus (final modulus on each curve) are observed to increase with more glutaric anhydride linkers incorporated. These material properties, together with the tested T_g, are summarized in Figure 5.2c.

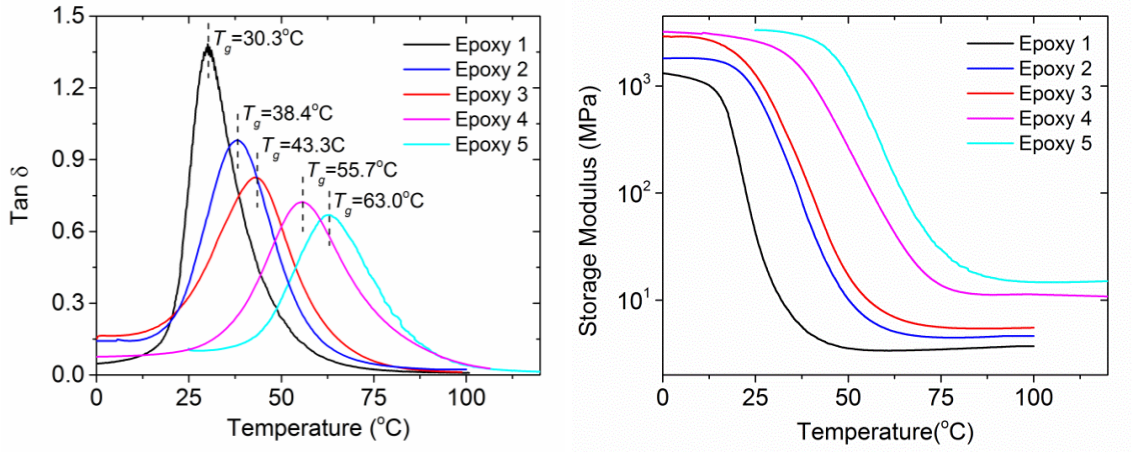

(a) (b)

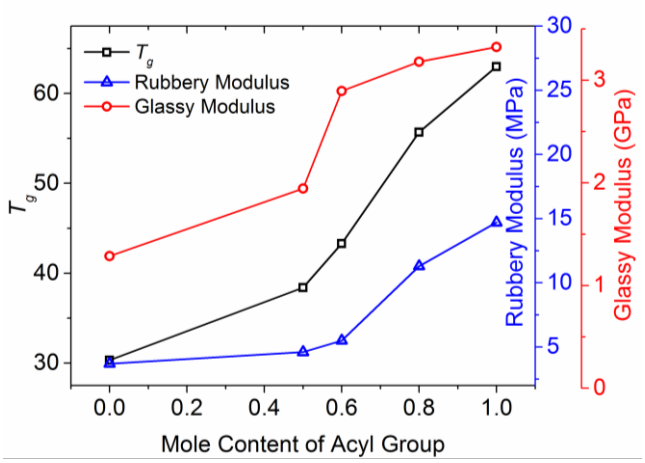

(c)

Figure 5.2. Comparisons of glass transition behavior of the five epoxy samples. (a) Tan δ curves as a function of temperature. The T_g is taken to be the temperature corresponding to the peak value. (b) Storage Modulus curves as a function of temperature (c) Comparison of T_g, rubbery modulus and glassy modulus as a function of mole content of glutaric anhydride linkers. Note: the glassy modulus is taken to be the initial value on the storage modulus curves as shown in Figure 3b

5.3 Stress Relaxation Behavior

For the test of time and temperature dependent stress relaxation of the epoxy-acid thermosets, samples with the same dimensions mentioned above were first preloaded by a 1×10^{-3} N force to ensure straightness. After reaching the testing temperature, it was allowed 30 min for the thermal equilibrium. The specimen was then stretched by 1% on the DMA machine and the deformation was maintained during the test. The decrease of stress was recorded and the stress relaxation modulus was calculated.

The stress relaxation in the CANs is attributed to the internal BERs. In Chapter 1, we have introduced the basic concept of the general exchange reactions in CANs (Figure 1.5). Here, we restate the working mechanism of BERs based on the thermally induced transesterfication reactions between the hydrogel and ester group, which is applied in the epoxy thermosetting networks. As shown in Figure 5.3, in an exchange reaction, an active group connected to a dangling polymer chain moves around and adds to an existing bond. This will form an intermediate structure, and subsequently reduce to a new bond and a new active group. The collective effect of such exchange reactions is to rearrange the topology of the network structure while preserving the bond density. When

mechanical stress is exerted on the network, the network topology rearrangement allows gradual relaxation of the stress.

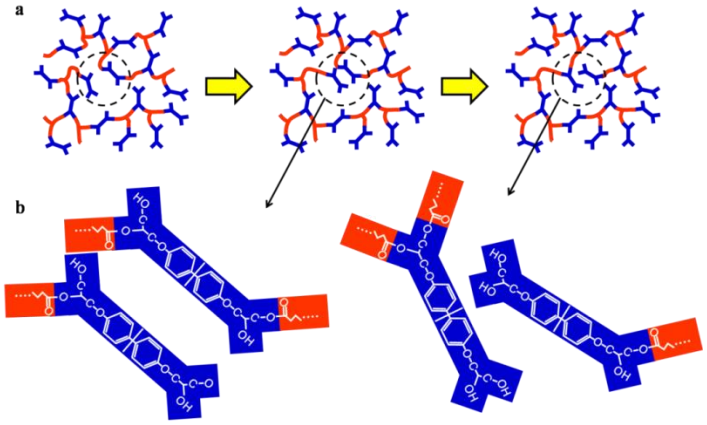

Figure 5.3. Schematic of the bond exchange reaction. (a) from left to right: before exchange, intermediate state and after exchange. (b) Structure change of the active groups during a bond exchange reaction.

To characterize the temperature dependent stress relaxation behavior, we start from the epoxy network without Glutaric Anhydride content, or the soft network that was previously studied by Montarnal et al. [5]. The solid lines in Figure 5.4 depict the relaxation test results of the soft epoxy material at 6 different temperatures (80 ^{o}C, 120 ^{o}C, 140 ^{o}C, 160 ^{o}C, 180 ^{o}C and 200 ^{o}C). The relaxation modulus is normalized and plotted on a double logarithmic scale. It is seen that the BERs release the internal stress at a faster rate when the temperature is higher. For example, at 180 ^{o}C, the BER rate is sufficiently increased and the normalized relaxation modulus decreases from 1 to 0.15 within 30 min, indicating an 85% drop of the internal stress. Comparison between Figure 5.2a and Figure 5.4 also reveals that the typical temperature required for BERs is significantly higher than glass transition temperature. As shown in Figure 5.2a, the glass transition is essentially complete at 80 ^{o}C, while the BERs are so sluggish (solid lines in Figure 5.4) that the material essentially behaves like elastomer without much stress relaxation.

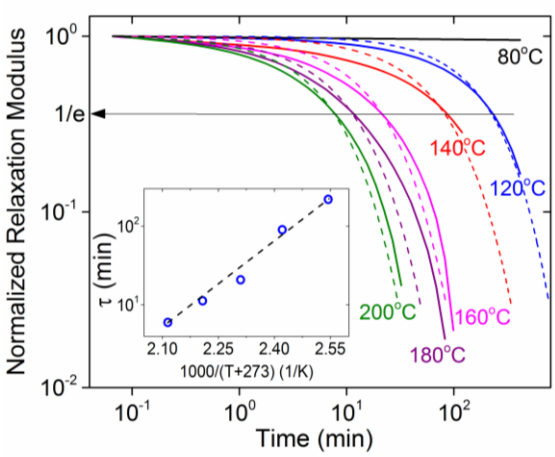

Figure 5.4. The temperature dependent stress relaxation behavior of the epoxy soft network. Solid lines denote experimental results and dash lines show the prediction. The inset view shows the linear relationship between τ and 1000/T

The stress relaxation behavior of CANs can be characterized according to the BER kinetics. Now we revisit Figure 5.3a in detail. Assuming that the exchangeable bonds exist on the backbone of a stretched macromolecule chain, a BER reaction will break the originally stressed chain, and results in a new chain in stress-free state, which consequently leads to the drop of internal stress. If there are N chains in a unit volume, the rate of BER, namely the rate of chains breakage, can be expressed as [4, 30]:

$$r = -\dot{N} = k \exp\left[-\frac{E_a}{R(T+273)}\right] N, \tag{5-1}$$

where T is the temperature in Celsius, k is a kinetic coefficient ($k > 0$), R is the gas constant with $R = 8.31446 J/Kmol$, and E_a is the activation energy.

In a time increment dt, the internal stress can be expressed as the summation of force in all the polymer chains within the unit volume, namely $\sigma = \sum_{i=1}^{N} f_i$, where f_i is the forces in each individual chain. Since the BER will break stressed chains, the drop of stress during the time interval could be correlated to the decreasing of stressed polymer chains within the unit volume: $\Delta\sigma = \frac{\dot{N}dt}{N}\sigma$. Substituting Eq. 1 into this expression, we have:

$$\frac{d\sigma}{\sigma} = -k \exp\left[-\frac{E_a}{R(T+273)}\right] dt, \tag{5-2}$$

which gives:

$$\sigma = \sigma_0 \exp(-\frac{t}{\tau}), \tag{5-3a}$$

and

$$\tau = \frac{1}{k} \exp\left[\frac{E_a}{R(T+273)}\right], \tag{5-3b}$$

where σ_0 is the initial stress before relaxation.

Eq. 5-3a also indicates that during the stress relaxation tests, the normalized relaxation modulus $\bar{E}(t)$ as plotted in Figure 5.4 can be characterized by the following classic exponential function:

$$\bar{E}(t) = \exp(-\frac{t}{\tau}), \tag{5-4}$$

where the relaxation time τ is corresponding to the time when normalized relaxation modulus declines to 1/e (~36.8%), and can be measured from the experimental relaxation curves. It is seen $\ln t$ is in a linear relationship with $1/(T+273)$ (see the inset view of Figure 5.4), which can be further verified by our derived expression of relaxation time as shown in Eq. 5-3b. By using the determined relaxation times, we can effectively capture the time and temperature dependent relaxation behavior of the epoxy polymer by using Eq. 5-4 (dash lines in Figure 5.4).

Subsequently, by shifting the stress relaxation curves in Figure 5.4 horizontally to a reference temperature T_r (160 ^{o}C), we found that the curves can be superposed and a master curve was constructed (see Figure 5.5a) with an extended timing scale, which also reflects the relaxation behavior of the epoxy thermoset at the reference temperature (160 ^{o}C). The existence of the master relaxation curve implies that the kinetics of the BER induced stress relaxation follows the well-known temperature-time superposition principles (TTSP), i.e.

$$\bar{E}(t,T) = \bar{E}(\alpha_T t, T_r) . \tag{5-5}$$

Here, α_T is a scalar factor multiplied to the time axis when shift the relaxation curves, and are plotted in Figure 5.5b as a function of temperature.

Combing Eq.5-3b, Eq. 5-4 and Eq. 5-5, we can derive the expression of shift factor α_T as:

$$\alpha_T = \exp\left[\frac{E_a}{R}\left(\frac{1}{T+273}-\frac{1}{T_r+273}\right)\right], \tag{5-6}$$

which is essentially the ratio between the temperature dependent relaxation time and the relaxation time at the reference temperature T_r. Eqs. 5-3 and 5-6 also indicate an Arrhenius-type dependence of the BER kinetics on temperature. In other word, the kinetics of BERs demonstrates a weaker dependence on temperature as compared to the stronger dependence of relaxation behaviors at temperatures above glass transition where the dependence follows Williams-Landel-Ferry (WLF) equation [31, 32]. This observation is consistent with what was reported by Montarnal et al., [5], where the kinetics was characterized by viscosity. By further examination of Eq. 5-6, we found that in the semi-log scale, the energy barrier could be determined by the slope of the shift factor curve. As shown in Figure 5.5b, by measuring the curve slope (8200*K*), the energy barrier E_a is calculated to be 68.18 *kJ/mol*, and the pre-exponential factor *k* equals $2.17\times10^5 s^{-1}$ at the reference temperature of 160 °C.

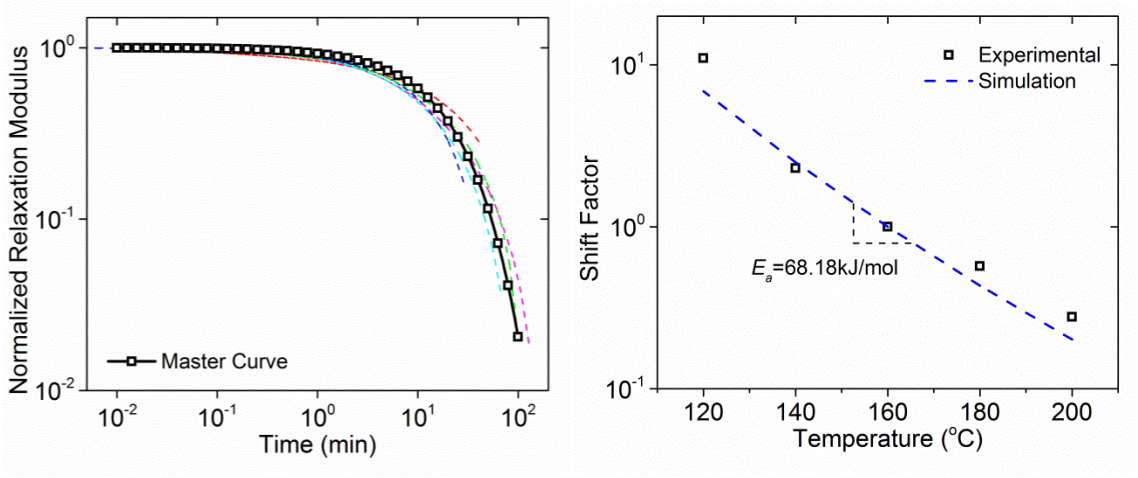

(a) (b)

Figure 5.5. (a) A master curve is constructed at the reference temperature of 160 °C. (b) Shift factors plotted as a function of temperature. Simulation curve are obtained based on Eq. 5-6. The slope determines the energy barrier for BERs.

After characterizing the stress relaxation in the Epoxy 1 thermosetting polymer, we were interested in how the BER induced stress relaxation ability can be affected by material stoichiometry. By using the same stress relaxation tests, the time and

temperature dependent relaxation curves of samples Epoxy 2-5 are shown in Figure 5.6. It is observed that the BERs still render the thermosetting polymers malleability at different temperatures. Similar to the sample Epoxy 1, the Arrhenius type stress relaxation behavior enables us to construct master curves for each epoxy sample.

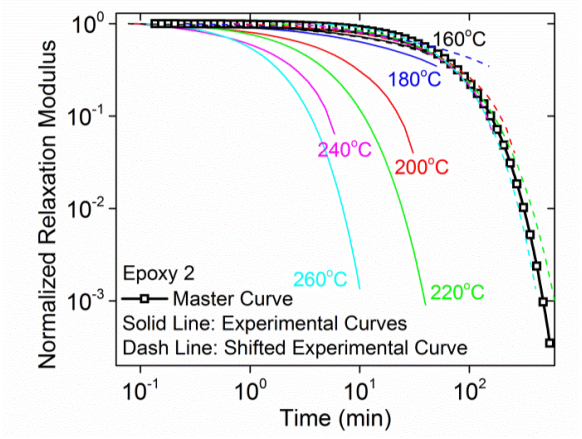

(a)

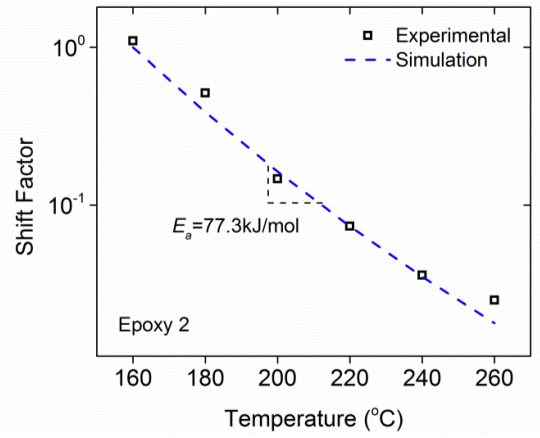

(b)

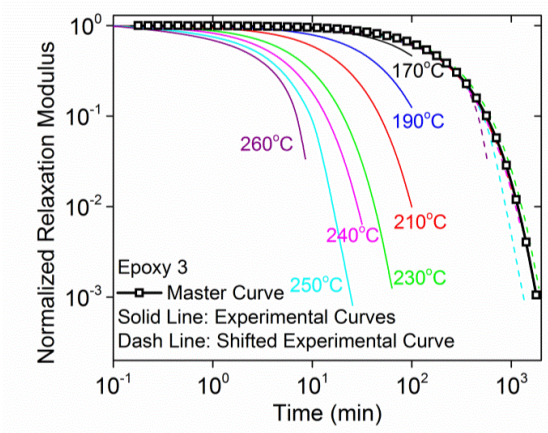

(c)

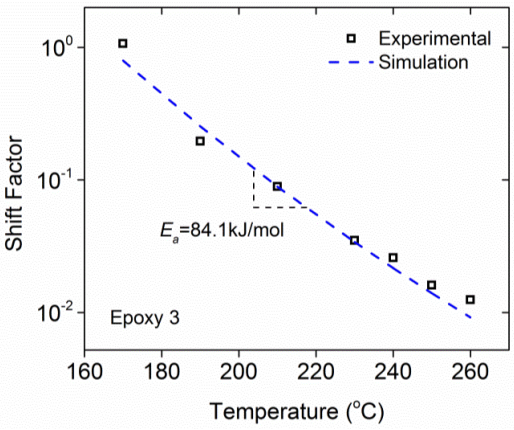

(d)

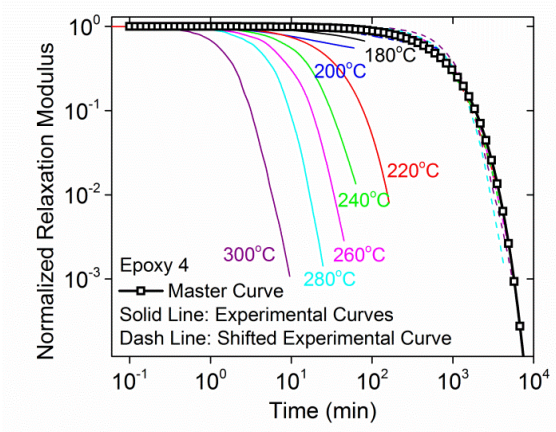

(e)

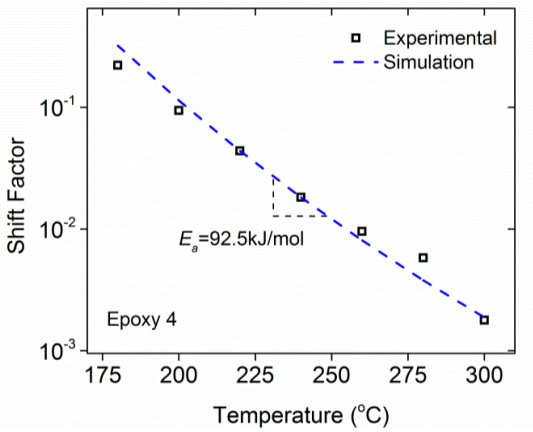

(f)

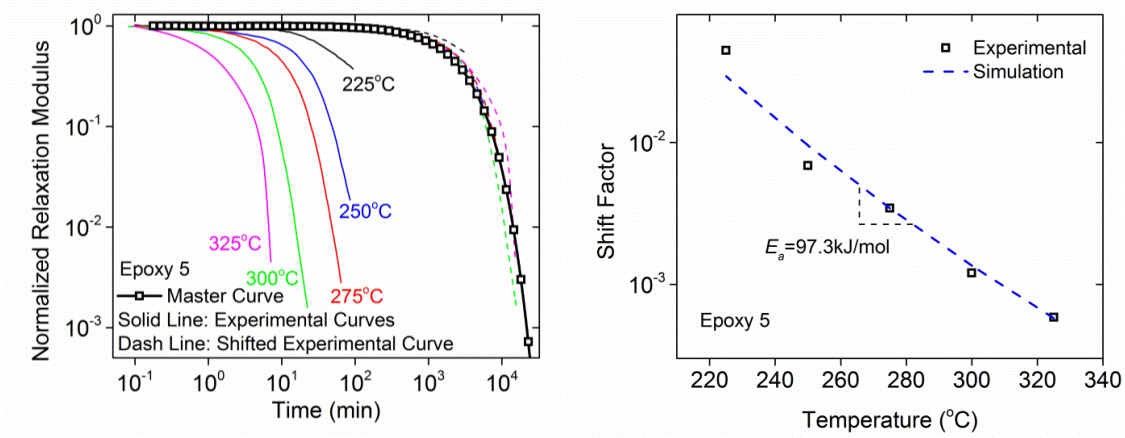

(g) (h)

Figure 5.6. The stress relaxation curves, master relxation curves and associated shift factors plots of (a) Epoxy 2, (b) Epoxy 3, (c) Epoxy 4 and (d) Epoxy 5. The stress relaxation behavior of Epoxy 1 is shown in Figure 1

To facilitate the comparisons, the reference temperature was uniformly set to 160 ^{o}C, and the predicted master curves are plotted in Figure 5.8a, which shows that as we increase the glutaric anhydride linker in the epoxy network, the characteristic relaxation time at the reference temperature is increased. For example, compared with the sample Epoxy 1 with a relaxation time of 20.9 min at 160 ^{o}C, the relaxation time of Epoxy 5 is predicted to be 3456min (~2.5 day). The increased relaxation times also indicate increased activation temperatures for BERs in the epoxy samples.

The Arrhenius type temperature dependence of the shift factors in each epoxy sample is plotted in Figure 5.8b. Since the curve's slope determines the activation energy barrier for BERs, the gradual increase in the slopes of the curves indicates that the energy barrier for BERs also increases. This is because within the thermosetting network, the length and flexibility of fatty acid linkers are typically higher than that of the glutaric anhydride liners (Figure 5.7a). At a given temperature, the polymer chain mobility of epoxy with higher content of hard anhydride segments is lower, which reduces the possibility of polymer chains moving around to seek available site for bond exchanges (Figure 5.7b). Based on the calculated energy barriers, together with the relaxation times at the reference temperature as shown in the Figure 5.8a, one can calculate the extrapolated relaxation time of each sample at different temperatures.

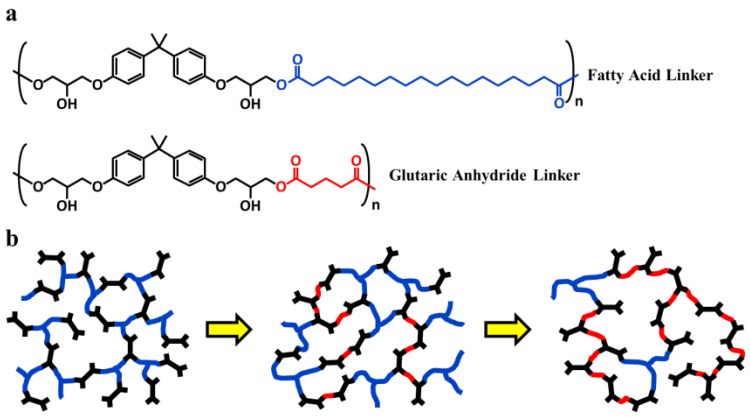

Figure 5.7. Topological illustration of the epoxy network with different composition. (a) Schematic view of the repeating unit of the glutaric anhydride and C18 dicarboxylic acid. (b) Topological illustration of the epoxy network as gradually increasing the proportion of glutaric anhydride.

For the convenience of comparison between the stress relaxation abilities of each sample, we further define a characteristic temperature T_c where the internal BER induced relaxation time is 10min. Since the required temperature for BERs is typically higher than the glass transition temperature, the difference between them, namely T_c-T_g actually quantifies how much additional energy is needed for the BERs after the glass transition is finished. This difference, along with the measured energy barrier for each epoxy sample, is plotted in Figure 5.8c as a function of the associated T_g. Linear relationship is found for both the energy barrier and T_c-T_g. The *least square* method generalized the following empirical formula, with 95% confidence bound for the fitting factors:

$$E_a = 0.87T_g + 43.5, \tag{5-7a}$$

$$T_c - T_g = 2.1T_g + 87.9. \tag{5-7b}$$

Note in the above two equations, the unit for temperatures is ^{o}C. The result in Eq. 5-7 indicates that if the epoxy polymer possesses a higher T_g, the difference between the T_g and the temperature to achieve comparable BER rate is larger. It qualitatively correlates the glass transition behavior and internal BERs of the epoxy thermosets, which would subsequently assist the design of such polymer materials according to specific requirements of practical engineering applications.

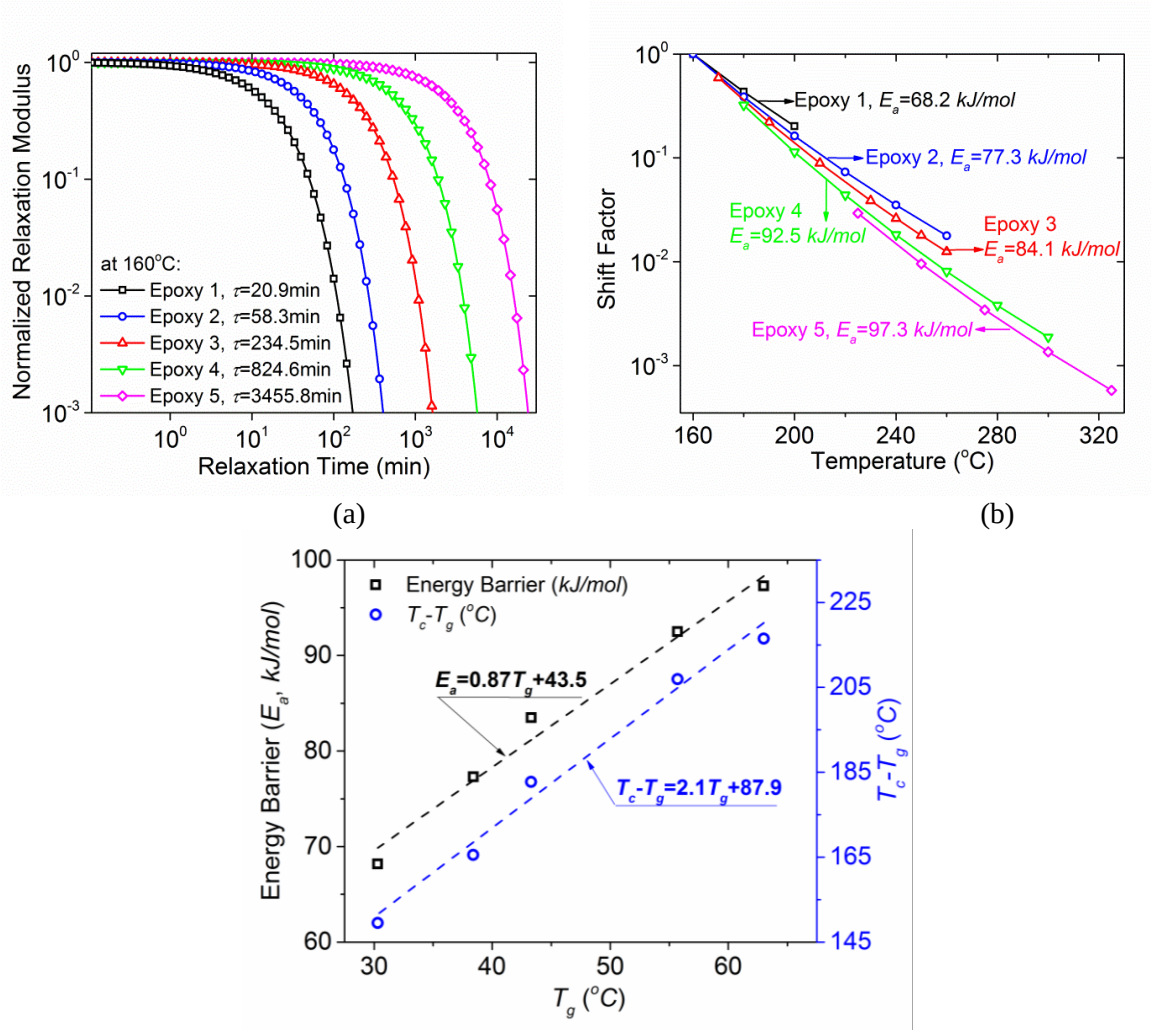

Figure 5.8. (a) The master relaxation curves in each epoxy sample. The reference temperature is uniformly chosen to be 160 °C. (b) The Arrhenius type shift factors plotted as a function of temperature. The energy barriers for the BERs in each epoxy sample are calculated based on the curve slopes. (c) Plot of the energy barrier for BERs and the difference between T_c and T_g as a function T_g.

5.4 Reprocessing, Recycling and Repairing Capability based on Surface Welding

In this section, we experimentally study the reprocessing and recycling ability of epoxy CANs in a pulverous state. Due to the large surface area and small size of polymer particles, their handling, transportation, and storage can offer convenience in comparison with traditional polymer scrap in bulk form, which can promote their incorporation into industrial applications in thermoset recycling, structure rehabilitations and component rework.

Figure 5.9 shows schematically the overall procedure of recycling and reprocessing. The bulk polymer is first pulverized into powders, which are then compacted into a mold by applying a pressure. The compacted powders are then heated to weld them into a bulk polymer. This process is repeated several times and the bulk polymer is evaluated for its mechanical properties after each processing. The details are described below.

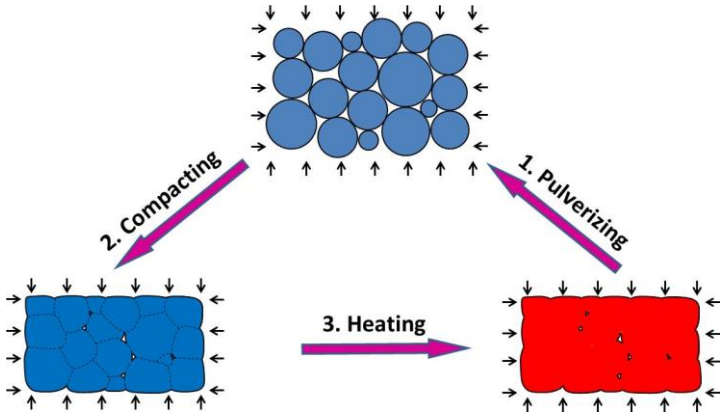

Figure 5.9. The schematic graphs for a typical reprocessing and recycling routine.

During the experiments, the bulk sample was manually abraded by a sandpaper to render the pulverous state. The isolated polymer particles were observed by using an optical microscope and shown in Figure 5.10a. From the microscopic morphology, it is seen the particles are irregularly shaped in profile. The particle size and the distribution were analyzed using software Imagine J. As shown in Figure 5.10b, the outline of each polymer particle was extracted. The particle diameter is taken to be the diameter of the circle with equal area of each corresponding particle profile. The analysis result is shown in the inset view of Figure 5.10b. It is seen that the diameter of most particles (over 77%) are distributed within 25μm - 120μm.

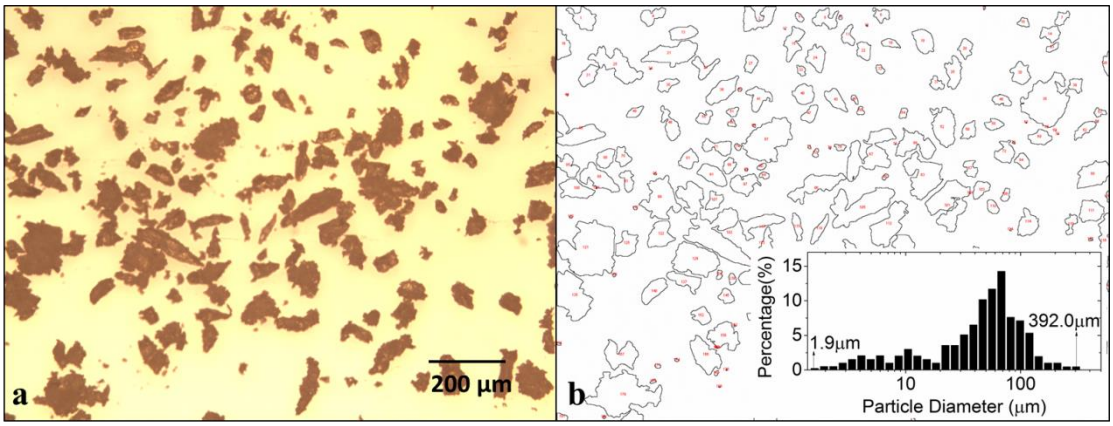

Figure 5.10. Analysis of particle sizes. (a) Microscopic observation of the isolated polymer particles. (b) Particle size and distribution analysis in Imagine J.

An aluminum punch mold was machined on lathe. The designed aluminum punch mold is shown in Figure 5.11a, where three hollow slots were machined in the platen to improve the thermal convective properties and temperature distribution during the heating. After filling the polymer powders into the mold (Figure 5.11b), it was then transferred into a customized thermal chamber for heating, while the applied pressure is controlled by a universal material testing machine (MTS, Model Insight 10, Eden Prairie, MN, USA). The temperature in the thermal chamber manufactured by Thermcraft (Model LBO, Winston Salem, NC, USA) is controlled with a Eurotherm controller (Model Euro 2404, N. Chesterfield, VA, USA) where a built-in electrical heater with a fan and an externally attached tank of liquid nitrogen provide the heat and cooling. In the work of Leibler et al[27]., a 1 MPa in pressure was introduced to promote the surface welding effect. Indeed, for a polymer in the elastic state, such a pressure would not noticeably affect the thermodynamics and reactions of polymer chains until it reaches to an extremely high value (in GPa ranges) when the free volume of single polymer chain is collapsed [33-35]. In our study, the applied pressure is also chosen to be small enough (90 KPa in maximum) to avoid affecting the transesterification reactions.

Figure 5.11. Experimental setup for the reprocessing and recycling test of thermosetting polymer. (a) Aluminum punch mold. (b) Polymer Powder is placed into the mold. (c) The heating is conducted in a customized thermal chamber with pressure applied via the MTS machine.

5.4.1 Reprocessing ability

A fresh bulk thermoset sample is shown in Figure 5.12a for comparison, while Figure 5.12b shows the appearance of the polymer from the pulverous state to the finished bulk state in a typical case with a 45KPa pressure. We limit ourselves to a constant temperature (180^{o}C) during the operation, and record the heating time immediately after the sample is placed in an oven at 180^{o}C. Due to the BER, the polymer powder starts surface welding and self-assembly. At 10min (middle figure of Figure 5.12b), isolated pulverous polymer tends to be in a compacted and consolidated form. Further heating of the sample under pressure for 30min renders an essentially complete welding effect where the sample appears transparent and resembles the fresh sample (shown in the right figure of Figure 5.12b), indicating that the interfaces among particles have disappeared.

The time and pressure dependent welding effect of the pulverous thermosetting polymer was quantified by the ultimate stretch (the stretch at the break) and initial elastic modulus (measured over the initial 15% stretch) of the reprocessed samples. The uniaxial tension test was conducted on a DMA machine at room temperature (23^{o}C). The loading rate was chosen to be a small value (5 %/min for all tests) to minimize viscoelastic effects. The bulk thermosetting polymer was reprocessed with different pressures (0KPa, 2KPa,

10KPa, 45KPa and 90KPa, respectively) applied during the heating process. The stress-strain behavior of the thermoset samples reprocessed at 45KPa is shown in Figure 5.12c. A fresh polymer sample was also tested after being heated at 180^{o}C for 1 h to normalize the comparison. For the pulverous sample heated for 10 min at 180^{o}C, we observed a relatively low initial elastic modulus of 2.2MPa. The sample fails quickly with an ultimate stretch of ~49.3%. With an increase of heating time, both the elastic modulus and ultimate stretch are improved in the reprocessed thermoset samples. With 30 min heating, the initial modulus and the ultimate stretch are 2.9MPa and 111.6%, respectively (or 76.7% and 77.9% of those in the referential fresh sample, respectively). Such an increase in the material stretch ability is due to the gradually welded interfaces and increased connections among the polymer particles, as shown in the microscopic observations in Figure 5.12d. Before the pulverous thermoset is totally welded, numerous voids (the dark regions in Figure 6d with 10min and 20min of heating) exist within the matrix, which can propagate cracks under external loads and compromise stretch ability. At 30min, the polymer powder is seen to be remolded into a coherent solid essentially resembling the fresh sample. The stress-strain curves in Figure 5.12c also reveal that the welding process is largely completed within 30min when 45KPa pressure is applied. From 30min to 1h, the ultimate stretch of the reprocessed sample is increased by ~7%. The inset in Figure 5.12c also shows the case when there is no pressured applied. The incompact polymer powder can only be partially welded, as evidenced by the very limited stretchability of less than 20% with an initial modulus around 1 MPa, even after being heated for 2h.

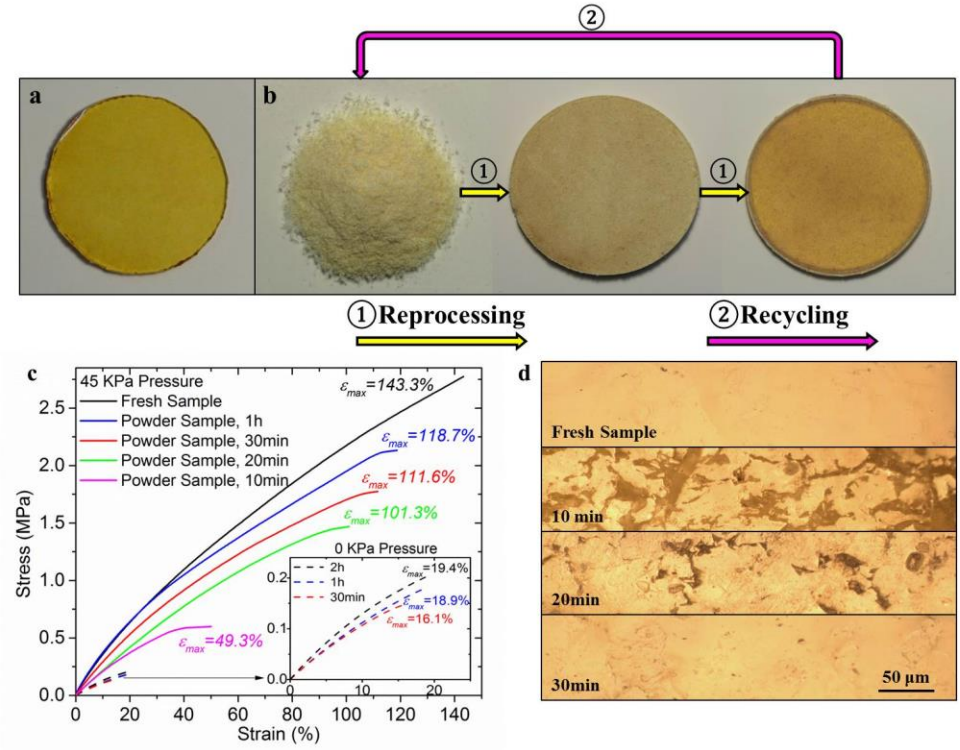

Figure 5.12. The typical reprocessing and recycling routine for the thermosetting polymer and the stress-strain behavior after different reprocessing times. (a) A fresh bulk thermosetting polymer. (b) the typical reprocessing and recycling routine (180^{o}C in temperature and 45KPa in pressure). From left to right: pulverous polymer after milling, polymer powder after being heated for 10 min and 30min respectively. (c) Stress-strain curves of the reprocessed sample after being heated for different time and with 45 KPa pressure applied. Note: the fresh sample is also heated at 180 ^{o}C for 1h to normalize the comparison. Inset view: Stress-strain curves of powder sample without pressure applied. (d) Surface morphology of both fresh sample and powder samples at different heating time.

The ultimate stretch and elastic modulus of the reprocessed samples under different reprocessing pressure and time are summarized in Figure 5.13a-d, respectively. Generally, both increasing pressure and increasing heating time can improve the final properties of the reprocessed samples. First, both ultimate stretch and elastic modulus of the reprocessed samples can achieve the levels of fresh samples, with a clear trend where increasing either heating time or pressure can accelerate this process. Second, increasing pressure is more effective in recovering the elastic modulus than in recovering the ultimate stretch. For example, at 90KPa, the elastic modulus reaches the fresh sample level within ~20-30min (Figure 5.13b&d); but within the same time period, the ultimate stretch only reaches 120% stretch, which is ~80% of that of the fresh samples (Figure 5.13a&c). Third, the elongated heating time can recover both the ultimate stretch and the

elastic modulus to the fresh sample levels, as long as the pressure is larger than a critical value. For example, even with 2KPa pressure, both ultimate stretch and elastic modulus almost achieve the fresh sample levels if heating at 720min (6h). Certainly, from the manufacturing point of view, heating for 720min is not energy efficient; increasing the pressure can shorten the heating time and thus help the design of an optimized reprocessing procedure, which deserves future studies.

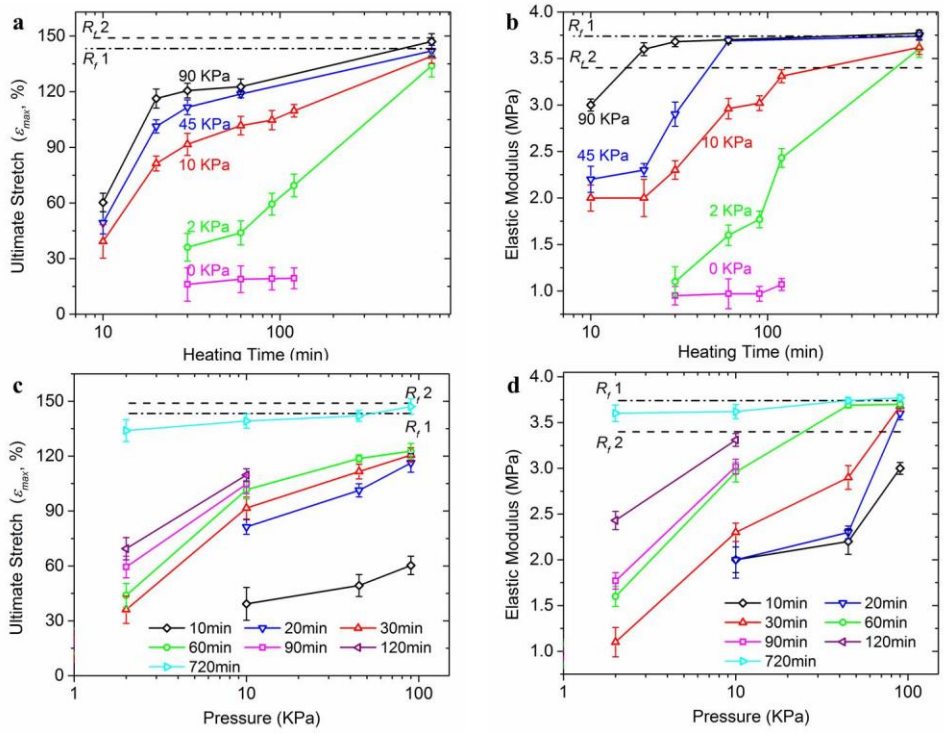

Figure 5.13. The time and pressure dependent ultimate stretch and initial modulus of the reprocessed thermosetting polymer (a) Ultimate stretch (maximum strain before fracture) plot of the reprocessed sample as a function of heating time. (b) Initial elastic modulus (within the first 15% stretch) as a function of heating time. (c) Ultimate stretch as a function of applied pressure. (d) Initial elastic modulus as a function of applied pressure. Note: R_f1 denotes the referencial property of a fresh bulk sample after being heating at 180 ^{o}C, while R_f 2 denotes that of the fresh sample without any heat treatment.

5.4.2 Recycling ability

Since the polymer chains in the thermoset are only exchanged but not consumed during the recycling operation, several cycles might be achieved. A set of aluminum molds with digital-shape grooves was designed to test the recycling ability of the thermosetting polymer. During the experiments, each reprocessed sample was pulverized into powder by using the same grade of sandpaper, and then recycled to the next generation of the object. With the same temperature (180^{o}C) and pressure (45 KPa)

applied, all the pulverous thermosets were heated for 30 min. The manufactured sample in each cycle is shown in Figure 5.14a, where the digit numbers indicate recycling generation. It is seen that pulverous thermosetting polymer possesses a good recycling ability in exhibiting transparent samples in different shapes. The glass transition temperature becomes slightly higher at 35.7^{o}C after the 4th generation of reprocessing, as compared to 30.1^{o}C of the fresh sample (Figure 5.14b). Besides, the rubber modulus (as seen in the storage modulus curve after 60 ^{o}C) is decreased after the 4th reprocessing. This is because during the pulverization of the polymer material, some permanently cross-linked strands of the polymer network are broken on the fracture surfaces [34] and can not be recovered during the subsequent healing process, which leads to a decreased crosslinking density and modulus in the rubber state. The stress-strain curves are shown in Figure 5.14c. It is remarkable to note that even after four times of reprocessing that sample still can achieve an ultimate stretch of 91.8% stretch. Figure 5.14d shows the evolution of the ultimate stretch and elastic modulus as a function of the number of recycling. Another set of recycling test are also presented in the figure where the heating time in each cycle is 2h. It is clear that although the properties of recycled material decay over the number of recycling, they stay in a reasonably good range. Also, the amount of decay decreases as the number of recycling increases, indicating more cycles of recycling is possible. In addition, the elongated heating time will improve the properties of recycled material significantly. As shown in Figure 5.14c, a 6 hour heating of the 4th generation sample leads to the ultimate stretch of 137.7%, which is comparable to that of the fresh sample without recycling history.

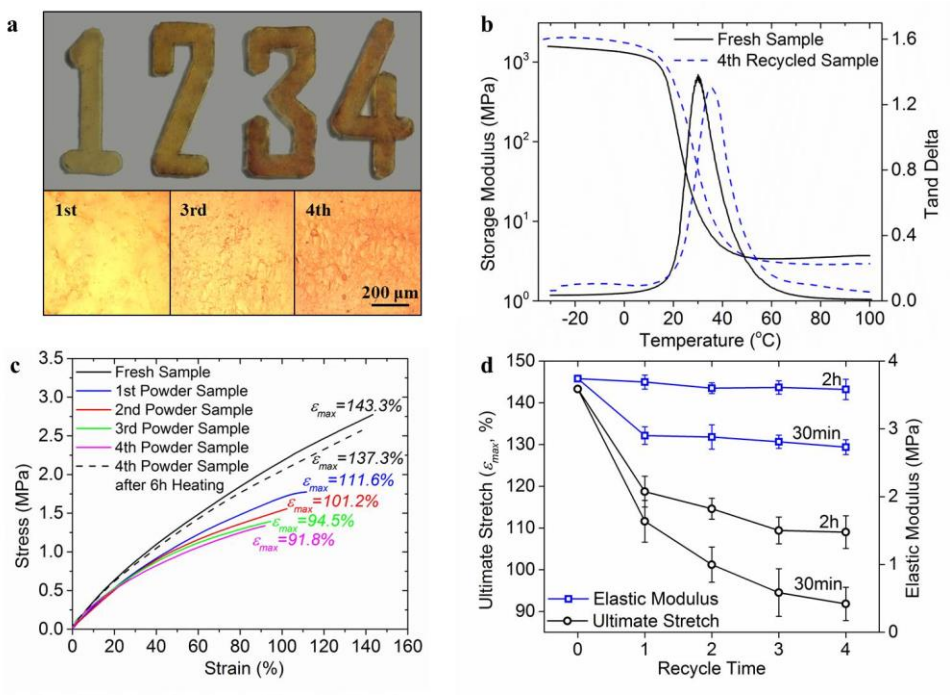

Figure 5.14. The recycling ability of the thermosetting polymer. (a) Top view: Sample manufactured by using polymer powder after being recycled for multiple times. Digit numbers indicate the recycle generation. Bottom view: the surface roughness observation on the 1st, 3rd and 4th recycled samples. (b). Stress-strain behavior of the polymer powder sample after being recycled for different times. The heating time is 30 min in each cycle. (c) Glass transtion behavior of the fresh sample and sample recycled for four times. (d) Ultimate stretch and initial elastic modulus plots as a function of recycle generations. Two sets of experiment are presented in the figure where the heating time in each reprocessing cycle is 30 min and 2 h respectively.

5.4.3 Repair bulk polymers by using the powder medium

In most engineering applications, the structural thermosetting polymers are susceptible to damage in the form of cracks, fractures and abrasions. Isolated interfaces might not be easily brought into contact again for welding. Structural patching using a bulk polymer is also not practical as it will potentially change the dimensions of polymer components. In view of these facts, the use of a pulverous thermoset as a repair medium is potentially a better choice. We therefore extended our study on the reprocessing and recycling ability of thermosetting polymers to this particular engineering application, namely utilizing polymer powder to reconnect the bulk material. As shown in Figure 5.15a, two strips of the bulk thermosetting polymer were placed on a glass slide, with alarge gap in between. Then the gap was filled with the polymer powder and sandwiched between two glass slides (Figure 5.15b).Utilizing the standard heating condition (30min at 180^{o}C with a pressure of 45 KPa), the two polymer pieces were reconnected as shown

in Figure 5.15c. The sample was further trimmed into a rectangular shape (Figure 5.15d) for tension tests.

The welding procedure mentioned above was also repeated with thermoset powder with recycling history (up to four generations), while the bulk polymer strips were always fresh samples. The stress-strain curves are then plotted in Figure 5.15e. It is seen that except for the 4th recycled powder healed sample, the initial elastic moduli of the other three samples are typically close to the fresh sample, while the ultimate stretch is lower than that of the reprocessed samples studied above. All the failures in the tested samples are located on the welded interface between the bulk polymer and the powder assembles. By using the powder that has been reprocessed four times, the ultimate stretch is decreased to 76.5% stretch. We conducted another set of experiments with 2h of heating time in each operation, and the mechanical properties are summarized in Figure 5.15f for comparison. Since the polymer materials were sandwiched between glass slides with pressure, increasing heating time would not significantly improve the material's stress-bearing ability, which is limited by in-plane pressure during the operation, and subsequently the interface strength between the bulk polymer and powder assembly.

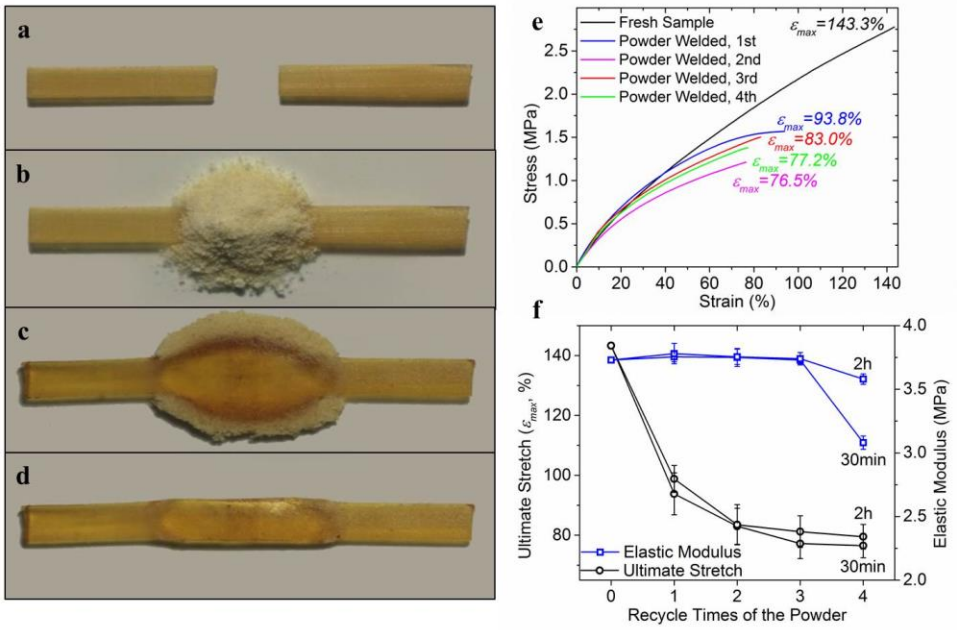

Figure 5.15. Welding isolated bulk thermoset strip by using the pulverous polymer. (a) Two separated pieces of the thermosetting polymer are placed on a glass slide. (b) The gap is filled with the polymer powder. (c) The separated thermosetting polymer is healed and assembled together after being heated at 180°C for 30min (45 KPa in pressure). (d) The sample is further trimmed into rectangular shape for tension test. (e) The stress-strain curves of the welded sample

by using polymer powder recycled for different times. The heating time is 30 min in each test. (f) Ultimate stretch and initial elastic modulus plots as a function of recycle times of the applied polymer powder. Two sets of experiment are presented in the figure where the heating time in each test is 30 min and 2 h respectively.

5.5 Conclusion

In this chapter, we experimentally tested two fundamental features of CANs with thermally induced bond exchange reactions (BERs), namely the BER induced stress relaxation and surface welding effect enabled reprocessing and recycling ability.

For the stress relaxation behavior, we synthesized epoxy thermoset polymers with different glass transition temperatures (T_g) by changing the stoichiometric ratios among monomers. The tunable T_g can be attributed to the alternation in polymer chain mobility and network flexibility. By using the standard stress relaxation tests, all the epoxy samples were shown to be able to effectively release the internal stress and rendered the thermoset polymers to be malleable, but the rate of stress relaxation is affected by the material composition. Based on the kinetics of BERs, we derived the detailed expression of the temperature dependent stress relaxation time. It is shown that the material relaxation behavior is following the Arrhenius type time-temperature superposition (TTSP). A master relaxation curve was consequently constructed, which further revealed the energy barrier for the BERs and enabled us to predict the relaxation time of each epoxy polymer at different temperatures. Finally, we experimentally correlated the glass transition behavior and internal BERs of the epoxy thermoset polymers. That is, when we gradually elevate T_g, the thermal energy required to achieve the same stress relaxation rate is linearly ramped.

For the surface welding effect enabled reprocessing and recycling ability, we demonstrated that after being grinded into a pulverous state of micrometer size particles and recycled multiple times, the thermoset polymer with exchangeable bonds could be assembled again into a coherent solid with mechanical properties comparable to the fresh bulk polymer. Considering the efficient and robust welding effect among polymer particles, as well as the maintained merits of thermoset polymer as stress-bearing materials during the healing operation, this strategy is suitable for repair of polymer

structures in service, as well as reprocessing and recycling of thermoset waste in engineering applications.

5.6 References

1. Ferry, J.D., *Viscoelastic properties of polymers.* John Wiley & Sons., 1980.
2. Billmeyer, F.W., *Textbook of Polymer Science; 3rd ed.* Wiley: New York, 1984.
3. Zheng, P.W. and T.J. McCarthy, *A Surprise from 1954: Siloxane Equilibration Is a Simple, Robust, and Obvious Polymer Self-Healing Mechanism.* Journal of the American Chemical Society, 2012. **134**(4): p. 2024-2027.
4. Capelot, M., et al., *Catalytic Control of the Vitrimer Glass Transition.* Acs Macro Letters, 2012. **1**(7): p. 789-792.
5. Montarnal, D., et al., *Silica-Like Malleable Materials from Permanent Organic Networks.* Science, 2011. **334**(6058): p. 965-968.
6. Kloxin, C.J., et al., *Covalent Adaptable Networks (CANS): A Unique Paradigm in Cross-Linked Polymers.* Macromolecules, 2010. **43**(6): p. 2643-2653.
7. Canadell, J., H. Goossens, and B. Klumperman, *Self-Healing Materials Based on Disulfide Links.* Macromolecules, 2011. **44**(8): p. 2536-2541.
8. Ghosh, B. and M.W. Urban, *Induced self-repairing oxetane-substituted chitosan polyurethane networks.* Abstracts of Papers of the American Chemical Society, 2009. **238**.
9. Ghosh, B. and M.W. Urban, *Self-Repairing Oxetane-Substituted Chitosan Polyurethane Networks.* Science, 2009. **323**(5920): p. 1458-1460.
10. Higaki, Y., H. Otsuka, and A. Takahara, *A thermodynamic polymer cross-linking system based on radically exchangeable covalent bonds.* Macromolecules, 2006. **39**(6): p. 2121-2125.
11. Maeda, T., H. Otsuka, and A. Takahara, *Dynamic covalent polymers: Reorganizable polymers with dynamic covalent bonds.* Progress in Polymer Science, 2009. **34**(7): p. 581-604.
12. Park, H.Y., et al., *Stress Relaxation by Addition-Fragmentation Chain Transfer in Highly Cross-Linked Thiol-Yne Networks.* Macromolecules, 2010. **43**(24): p. 10188-10190.
13. Rowan, S.J., et al., *Dynamic covalent chemistry.* Angewandte Chemie-International Edition, 2002. **41**(6): p. 898-952.
14. Scott, T.F., et al., *Photoinduced plasticity in cross-linked polymers.* Science, 2005. **308**(5728): p. 1615-1617.
15. Wojtecki, R.J., M.A. Meador, and S.J. Rowan, *Using the dynamic bond to access macroscopically responsive structurally dynamic polymers.* Nature Materials, 2011. **10**(1): p. 14-27.
16. Taynton, P., et al., *Heat- or Water-Driven Malleability in a Highly Recyclable Covalent Network Polymer.* Advanced Materials, 2014. **26**(23): p. 3938-3942.
17. Chen, X.X., et al., *A thermally re-mendable cross-linked polymeric material.* Science, 2002. **295**(5560): p. 1698-1702.

18. Zhang, Y., A.A. Broekhuis, and F. Picchioni, *Thermally Self-Healing Polymeric Materials: The Next Step to Recycling Thermoset Polymers?* Macromolecules, 2009. **42**(6): p. 1906-1912.
19. Reutenauer, P., et al., *Room Temperature Dynamic Polymers Based on Diels–Alder Chemistry.* Chemistry – A European Journal, 2009. **15**(8): p. 1893-1900.
20. Adzima, B.J., et al., *Rheological and Chemical Analysis of Reverse Gelation in a Covalently Cross-Linked Diels−Alder Polymer Network.* Macromolecules, 2008. **41**(23): p. 9112-9117.
21. Lehn, J.M., *Dynamers: Dynamic Molecular and Supramolecular Polymers.* Australian Journal of Chemistry, 2010. **63**(4): p. 611-623.
22. Deng, G.H., et al., *Covalent Cross-Linked Polymer Gels with Reversible Sol-Gel Transition and Self-Healing Properties.* Macromolecules, 2010. **43**(3): p. 1191-1194.
23. Skene, W.G. and J.M.P. Lehn, *Dynamers: Polyacylhydrazone reversible covalent polymers, component exchange, and constitutional diversity.* Proceedings of the National Academy of Sciences of the United States of America, 2004. **101**(22): p. 8270-8275.
24. Amamoto, Y., et al., *Repeatable Photoinduced Self-Healing of Covalently Cross-Linked Polymers through Reshuffling of Trithiocarbonate Units.* Angewandte Chemie, 2011. **123**(7): p. 1698-1701.
25. Nicolay, R., et al., *Responsive Gels Based on a Dynamic Covalent Trithiocarbonate Cross-Linker.* Macromolecules, 2010. **43**(9): p. 4355-4361.
26. Scott, T.F., R.B. Draughon, and C.N. Bowman, *Actuation in crosslinked polymers via photoinduced stress relaxation.* Advanced Materials, 2006. **18**(16): p. 2128-+.
27. Capelot, M., et al., *Metal-Catalyzed Transesterification for Healing and Assembling of Thermosets.* Journal of the American Chemical Society, 2012. **134**(18): p. 7664-7667.
28. Yu, K., et al., *Influence of stoichiometry on the glass transition and bond exchange reactions in epoxy thermoset polymers.* Rsc Advances, 2014. **4**(89): p. 48682-48690.
29. Yu, K., et al., *Reprocessing and recycling of thermosetting polymers based on bond exchange reactions.* Rsc Advances, 2014. **4**(20): p. 10108-10117.
30. Long, R., H.J. Qi, and M.L. Dunn, *Modeling the mechanics of covalently-adaptable polymer networks with temperature-dependent bond exchange reactions.* Soft Matter, 2013. **9**(15): p. 4083 - 4096.
31. Rubinstein, M. and R.H. Colby, *Polymer physics*. 2003, New York: Oxford University Press, Oxford.
32. Williams, M.L., R.F. Landel, and J.D. Ferry, *Temperature Dependence of Relaxation Mechanisms in Amorphous Polymers and Other Glass-Forming Liquids.* Physical Review, 1955. **98**(5): p. 1549-1549.
33. Benjamin, A.S., et al., *Acoustic properties of Kel F-800 copolymer up to 85 GPa.* Journal of Chemical Physics, 2012. **137**(1).
34. Stevens, L.L., et al., *Brillouin-scattering determination of the acoustic properties and their pressure dependence for three polymeric elastomers.* Journal of Chemical Physics, 2007. **127**(10).

35. Dreger, Z.A., et al., *Effect of high pressure on acoustic properties of several polymers: Use of impulsive stimulated light scattering method.* Journal of Applied Physics, 2011. **109**(8).

CHAPTER 6

INTERFACIAL MECHANICS OF COVALENT ADAPTIVE NETWORKS

The aforementioned reprocessing, recycling and repairing ability of covalent adaptive networks (CANs) are based on the surface welding effect, which is resulted from the thermally induced BERs. However, as we mentioned in Chapter 1, most previous modeling works for the surface welding effect are based on the molecular theory [1] or molecular dynamics (MD) simulation [2], where molecular parameters are unavoidable and hard to be determined by using the standard polymer testing methods. Continuum mechanics models typically possess concise and straightforward modeling frames for engineers, but for the interfacial mechanics of CANs, to the best of our knowledge, little work has been conducted before.

In this chapter, we developed a theoretical model to study the surface welding effect of CANs with thermally induced BERs. The developed lattice model is inspired by the classic random walk theory of polymer chains with the kinetics of BERs to describe diffusion of polymer chains within the CANs, as well as the accumulation of polymer chains on the interface with real contact. Only two parameters are needed in the lattice model, namely the energy barrier for the chemical reaction and a factor of the reaction rate. Both two factors could be easily measured through relaxation tests on bulk materials.

6.1 Experimental and Results

The material we used in this study is still the epoxy CAN reported by Montarnal and coworkers[3], namely the Epoxy 1 thermoset studied in Chapter 5.

6.1.1 Scanning electron microscope observations of welded surface

To examine the interface morphology of the welded epoxy thermoset, a fresh sample was firstly cut into half by using a razor at the room temperature, and then squeezed together for welding on a universal material testing machine (MTS, Model Insight 10, Eden Prairie, MN, USA) with different temperature and pressure applied (see the left

figure in Figure 6.1). The temperature in the thermal chamber manufactured by Thermcraft (Model LBO, Winston Salem, NC, USA) is controlled with a Eurotherm controller (Model Euro 2404, N. Chesterfield, VA, USA). After the welding, the interface morphology of the epoxy thermoset was observed by using a Scanning Electron Microscope (SEM, Model Phenom Pro, PhenomWorld, Netherlands). Before the SEM, the sample was coated with a thin gold film on a Sputter Coater (Mode 108 Auto, Cressington Scientific Instruments Ltd., Watford, UK). The thickness of the gold film is around 100nm. Figure 6.1 shows the interfacial morphology of epoxy samples after being welded for 20min at 180 ^{o}C (40 KPa applied). It is seen that the two epoxy samples are reconnected in the micro-scale with most interface disappears. However, due to the surface roughness, the contact cannot be achieved everywhere on the interface. The typical size of the interfacial void is 10μm - 30μm in width and 50μm - 200μm in length.

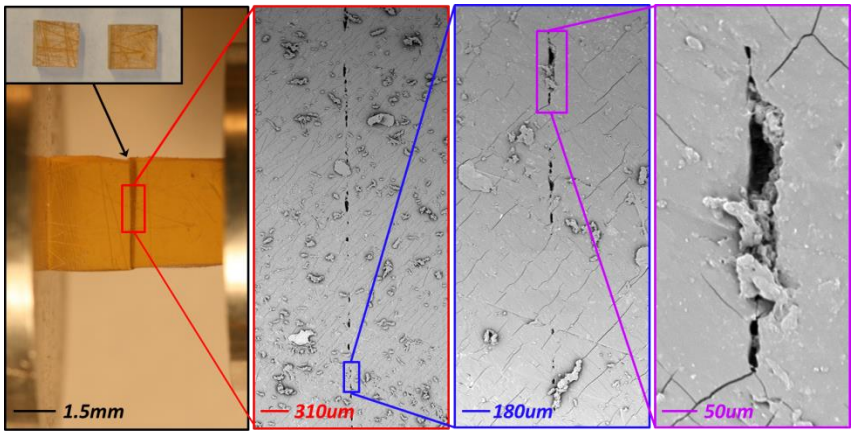

Figure 6.1. Interface morphology of two epoxy samples after being welded at 180 ^{o}C for 20min with 40 KPa applied

6.1.2 Uniaxial tension tests on welded polymer sample

The effective stress-strain behavior of the welded epoxy sample at room temperature was evaluated by using uniaxial tension tests on the DMA machine. The loading rate was chosen to be a small value (5 %/min for all tests) to minimize viscoelastic effects. Figure 6.2a shows the stress-strain curves of the thermosetting samples after being welded for different times (with 180 ^{o}C and 40 KPa applied). A fresh polymer sample was also tested (shown as dash line) to normalize the comparison. The inset view shows the appearance of the welded sample during the tests. Figure 6.2b and Figure 6.2c summarize the initial elastic modulus (within the first 10% stretch) of the welded sample with

different welding pressure and sample length. For each tension test, at least four samples were tested and the average values were reported. Generally, as shown in Figure 6.2a and Figure 6.2b, both ultimate stretch and elastic modulus of the welded samples can achieve the levels of fresh samples, with a clear trend where increasing either heating time and pressure can accelerate this process. Figure 6.2b shows the evolution of modulus as a function of time, pressure applied. The initial elastic modulus has been largely recovered within 30min of heating, before that the existence of interface will decrease the effective initial modulus of the welded sample. It is also interesting to see that the modulus is also a function of sample length, under otherwise identical reprocessing conditions. As shown in Figure 6.2c, as the sample length increase from 3mm to 12mm, the modulus measured at 10min reprocessing time increases by ~20% (from ~0.775 to ~0.925).

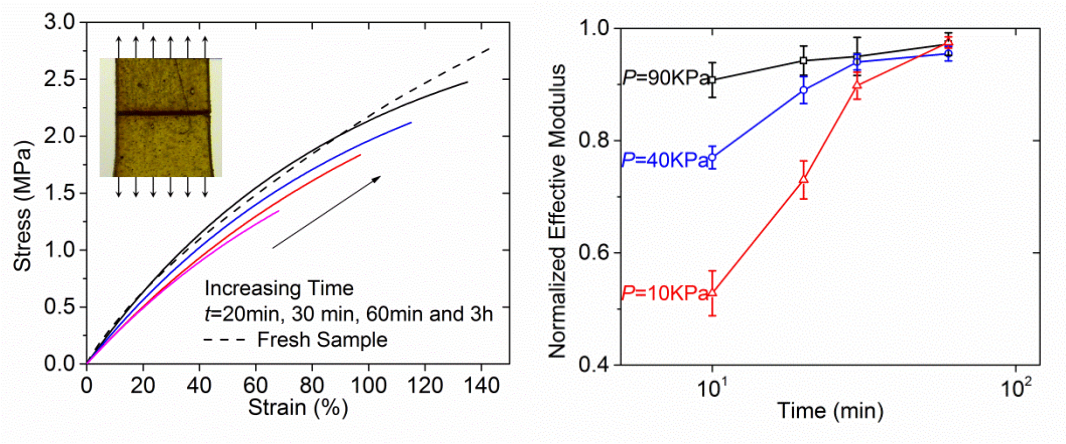

(a) (b)

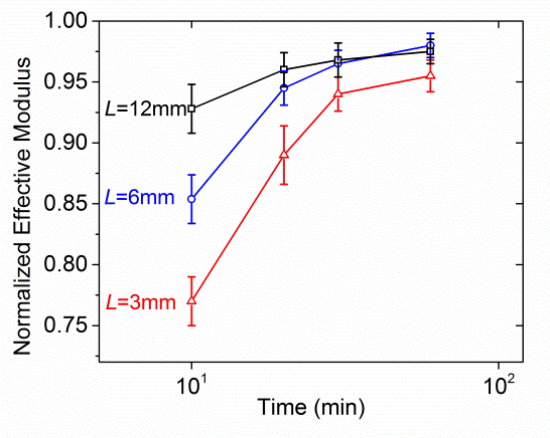

(c)

Figure 6.2.Mechanical properties of the welded epoxy sample. (a) Stress-strain curves of the thermosetting samples after being welded for different times. Inset view shows the appearance of the welded sample during experiment. The applied pressure is 40 KPa. (b) Initial elastic modulus (within the first 10% stretch) of welded sample with different pressure applied. The sample length

is 6mm (c) Initial elastic modulus (within the first 10% stretch) of welded sample with different sample length. The applied pressure is 40 KPa.

6.1.3 T-peeling experiments

Since the epoxy thermosetting polymer is flexible at the room temperature, we adopt the T-peeling test (ASTM D1876) [4] to measure the interfacial fracture energy of the welded sample. Two epoxy strips with the same dimension (20mm × 3mm × 2 mm) were compressed on the MTS machine for welding with different heating time, temperature and pressure applied. An open region was left at the end of the welded sample. After the welding process, each end of the welded sample was loaded into two opposing tensile grips of the DMA machine (see the inset view of Figure 6.3). During the peeling test, the grips were separated at a constant rate of speed (50mm/min) for all samples. Figure 6.3 shows the typical peeling force as a function of displacement after the epoxy sample being welded at 180 ^{o}C for 30min and 3h respectively. The maximum and minimum peeling force during the steady propagation of crack will be used to calculate fracture energy of interface.

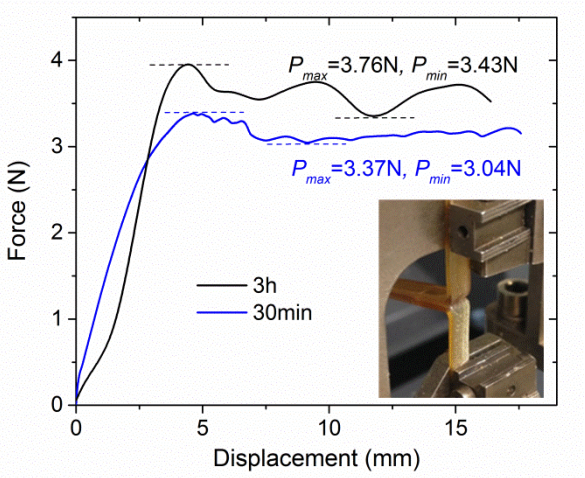

Figure 6.3.Peeling force as a function of displacement after the epoxy sample being welded at 180 ^{o}C for 30min and 3h respectively. Inset view shows the sample appearance on the DMA machine during the T-peeling tests.

6.2. Constitutive Modeling

6.2.1 A lattice model for interfacial welding

When the exchange reaction occurs within the backbone of a polymer network, it will lead to a diffusion of polymer chains and rearrange the overall network connectivity [5].

Therefore, we propose a two dimensional (2D) squared lattice model to geometrically describe the CANs topology, which is commonly used to study the chains random walking in polymer physics. We consider two identical networks (A and B in Figure 6.4a). Within the each network, we assume the amount of elastically ineffective features, such as dangling chains and loops, are negligible. Local crosslinking points of the thermosetting network are represented by a single point in average and denoted as each point on the lattice grid. The lattice side length is in nano-scale and is comparable to the radius of gyration of polymer chain. Between the two lattice points, we assume there are plenty chains connected to them. The chain density is denoted as Δ_i. It should be noted that although there should be more than one exchangeable bond rested on each point, we assume the situation that the chain broken and connected by themselves in forming a loop is highly impossible. In this manner, we only consider a single pair of exchangeable bond on each lattice side. The two networks are separated by one lattice distance.

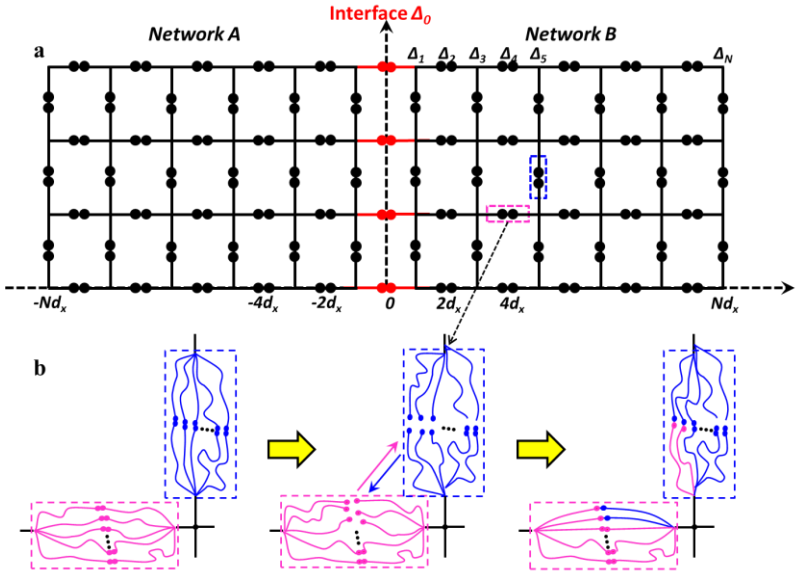

Figure 6.4.The proposed two dimensional (2D) squared lattice model to characterize interfacial kinetics. (a) The lattice geometry and (b) BER induced local chain redistribution between two neighboring lattice sides.

When the temperature is sufficiently high, BERs become active, which lead to the cleavage and reconnection of polymer chains within the adaptive network. Considering the two neighboring lattice sides shown in Figure 6.4b, during a time interval from t to Δt,

the amount of broken chains on a given side is $\Delta(t, x)Kdt$, where $\Delta(t, x)$ is the local chain density at the beginning of the time t at location x, and

$$K = \frac{1}{\tau} = k \exp\left[-\frac{\mu_a}{R(T+273)} \right]. \tag{6-1}$$

If we assume these broken chains will either stay in the same area, or jump into the neighboring side with the same probability, then we can write the local chain density at the end of time interval by the following incremental equation:

$$\begin{aligned} \Delta(t+dt, x) = \Delta(t, x) - \underbrace{\frac{8}{9}\Delta(t, x)Kdt}_{\text{chain lost to neighbors}} \\ + \underbrace{\left[\frac{1}{9}\Delta(t, x-2d_x) + \frac{2}{9}\Delta(t, x-d_x) + \frac{2}{9}\Delta(t, x) + \frac{2}{9}\Delta(t, x+d_x) + \frac{1}{9}\Delta(t, x+2d_x) \right]}_{\text{chain lost from neighbors}}. \end{aligned} \tag{6-2}$$

On the right hand side (RHS) of Eq. 6-2, the first item denotes the local chain density at the end of this time interval; the second item is the amount of chains escapes from the lattice point at x with the assumption that a point can lost a chain to its neighboring eight sites and itself (total nine) at equal probabilities but only the lost to the neighbors are the true lost; the third item is the gain from the eight neighboring sides to the local chain density.

After expanding each item in Eq. 6-2 by Taylor expansion, and ignoring higher order items, the incremental equation will be generalized into a continuous differential equation.

$$\frac{\partial \Delta}{\partial t} = \alpha^2 \frac{\partial^2 \Delta}{\partial x^2}, \tag{6-3a}$$

$$\alpha^2 = \frac{2}{3} K d_x^2 \tag{6-3b}$$

Eq. 6-3 indicates that within the CANs, the BERs induced chains migration is essentially a diffusion process with diffusivity α. This is consistent with previous studies by Leibler et al [6], where the diffusivity is taken to be $N_m b_m^2 / \tau$, with N_m denoting number of monomers and b_m denoting monomer length respectively. Therefore, the lattice size can be analogized to be $d_x^2 = \frac{3}{2} N_m b_m^2$. Eqs. 6-1-6-3 establish a direct connection between K or μ_a and diffusivity of chain due to BER in the material.

At the beginning of surface welding, the interfacial chain density is zero, namely $\Delta(0,x)=0$ for $-d_x \le x \le d_x$, and $\Delta(0,x)=\Delta_0$ for $-Nd_x \le x \le -d_x$ and $d_x \le x \le Nd_x$. For the sites inside the material, however, an initial chain density gradient exists and will drive the polymer chains gradually move onto the interface. Meanwhile, we assume the chain density on the lattice boundary ($x=\pm Nd_x$), does not change over time, namely $\left.\frac{d\Delta(t,x)}{dt}\right|_{x=\pm Nd_x}=0$, which indicates that the polymer matrix beyond the lattice area will provide numerous chains into the lattice modeling area.

Based on the above mentioned initial and boundary conditions, Eq. 6-3 can be solved easily. The chain density evolution within the lattice area is expressed as:

$$\Delta(t,x)=\Delta_0+\sum_{i=1} B_i \cos\left(\frac{2i-1}{2Nd_x}\pi x\right)\exp\left(-\frac{t}{\varphi_i}\right) \tag{6-4a}$$

with $$\varphi_i=\left(\frac{2N}{2i-1}\right)^2\frac{3}{2K\pi^2}, \text{ and } B_i=-\frac{4\Delta_0}{(2i-1)\pi}\sin\left(\frac{2i-1}{2N}\pi\right) \tag{6-4b}$$

The chain density evolution on the interface (*x=0*) is written as:

$$\Delta(t,0)=\Delta_0+\sum_{i=1} B_i \exp\left(-\frac{t}{\varphi_i}\right) \tag{6-5}$$

In Eq. 6-4 and 6-5, *N* denotes the amount of lattice layer parallel to the interface. Physically, it represents the depth of the concerned thermosetting network beneath the interfacial area during the characterization of interfacial kinetics.

6.2.2 Evolution of interface areas

The above mentioned constitutive relations describe the time and temperature dependent interface chain density. Intuitively, we can proceed to evaluate the mechanical properties of the welded epoxy polymer as it is determined by the chain density distribution. However, there are three non-trivial questions have to addressed. First, the initial modulus of the welded sample is dependent on the applied pressure while the lattice model ignores the influence of pressure because it does not affect the BER kinetics. The assumption of BER kinetics being independent of pressure remains to be true in the range of the pressure applied. Second, if we would treat the welded epoxy sample as a composite material with the interface layer perpendicular to the stretching direction, the

effective modulus should always be close to that of pure epoxy material because the volume fraction of the interface, namely the interface thickness compared to the sample length, is very small. But the initial modulus of the welded sample is seen to increase with as increasing sample length. This means the influence of interface on the material modulus cannot be simply characterized by using the classic theory of composite.

SEM micrographs shown in Figure 6.1 suggest that due to the surface roughness, contact does not spread over the interface of the welded epoxy samples, and microscopic voids still exist. A higher welding pressure will squeeze the surface asperities and increase the real contact area on the interface. The contact area will further increase when the BERs gradually release the stored elastic energy in the asperities. Eventually, a full contact can be reached after squeezing and heating the sample long enough. Since the polymer chains can only be connected on the real contact area, pressure will affect the mechanical properties of interface by affecting the interface contact morphology.

From above discussion, it is apparent that surface roughness, or true contact area and pressure play any important role determining the efficiencies of surface welding. Most previous contact mechanics theories are based on Hertz contact theory [7] for elastic spheres with perfectly smooth surfaces. The random surface asperities are approximated to be spherical or elliptical bumps, and the elastic coupling between the asperity contact regions is neglected. This is the basic strategy for both the Greenwood-Williamson theory [8] and the theory of Bush et al [9, 10]. A necessary condition for these theories is that the squeezing pressure must be so small that the area of real contact is very small compared to the nominal contact area. However, these assumptions are not valid when it comes to the soft CAN, where large deformation in asperities is expected and deformation of each asperity is no longer independent. In this case, we adopt Persson's contact theory [11-15] that removes the assumption of small pressure and small deformation, and is valid up to the full contact situation.

Following Persson et al [11-14], the ratio between real contact area and nominal contact area is written as:

$$\frac{A(\mathrm{t})}{A_0} = erf\left(\frac{1}{2\sqrt{\Omega}}\right), \tag{6-6a}$$

with $$\Omega = \frac{\pi}{4} C \left(\frac{E}{(1-\nu^2)p} \right)^2 , \tag{6-6b}$$

where A_0 is the nominal area of interface, p is the squeezing pressure, ν is the Poisson's ratio, and E is the elastic modulus of substrate material. Persson et al [14] also pointed out that the elastic modulus can be the relaxation modulus if viscous material is encountered. C is the surface roughness constant that is related with the surface asperity amplitude and wavelength, i.e.

$$C = \frac{1}{\sqrt{2\pi}} \int_{x_0}^{\infty} \int_{-\infty}^{\infty} H(x) \exp(-iqx) dx dq , \tag{6-6c}$$

where $H(x)$ is the surface height-height correlation function and x_0 is the measurement resolution [13, 15]. It should be noted that although the roughness constant can be experimentally determined by measuring the surface height profile, no attempt is made to this end in this study and C is treated as a fitting parameter in the following discussions.

6.2.3 Continuum level model of the effective modulus of welded sample

Substituting the temperature dependent relaxation modulus (Eq. 5-4), the real contact area in Eq. 6-6 will gradually increase over time and finally approach the full contact (A=A_0) (as illustrated in Figure 6.5).

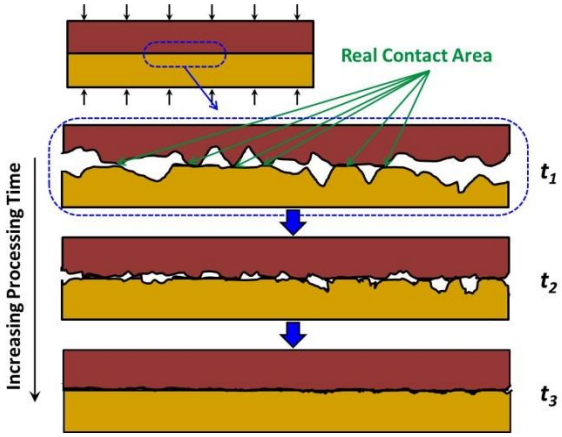

Figure 6.5. Real contact area increases as the increment of processing time.

During the increment of real contact area, polymer chains on the interface are connected at different time. At the timing point t, the accumulation of normalized chain density on the interface is written as:

$$n_f(t) = \frac{1}{A_0} \int_0^t \frac{dA(s)}{dt} \Delta(t-s) ds . \tag{6-7}$$

It is noted that while Eq. 6-5 describes the normalized interfacial chain density at the ideal condition, i.e. a perfect contact situation, Eq. 6-7 calculates the normalized chain density on the real polymer interface with the considerations of surface roughness and influence of squeezing pressure.

If we assume the connected polymer chains on the interface are ideal, each chain can be characterized as $f = k_f \chi$, where f is the force, χ denotes end to end displacement. k_f is the spring constant of single polymer chain which can be written as [16, 17]:

$$k_f = \frac{3k_b T}{N_k b_k^2}, \tag{6-8}$$

where k_b is the Boltzmann's constant, N_k is the number of Kuhn segment in one long chain, b_k is the length of single Kuhn segment.

For the welded epoxy sample, when a tension force F is applied, the length change of the bulk material is $\delta L = \frac{FL}{E_0 A_0}$, where L is the sample length and E_0 is the material modulus at the room temperature. In the interface, the length change is $\chi = \frac{F}{n_f m A_0 k_f}$, where m is the number of chains in the bulk material across unit area. Then the total engineering strain of the welded sample is $\varepsilon = \frac{\chi + \delta L}{L}$. The elastic modulus of the welded sample can therefore be written as:

$$\bar{E} = \frac{F}{A_0 \varepsilon} = \frac{1}{\left(\frac{1}{E_0} + \frac{N_k b_k^2}{3 n_f m k_b T L} \right)}, \tag{6-9a}$$

If we consider the modulus of bulk material is related with the volume chain density ζ as $E_0 = \zeta k_b T$, we further have:

$$\bar{E} = \frac{k_b T}{\left(\frac{1}{\xi} + \frac{N_k b_k^2}{3 n_f m L} \right)}. \tag{6-9b}$$

The second item in the bracket of the denominator of Eq. 6-9b indicates the influence of interface on the effective modulus of welded epoxy sample. First, the modulus of the welded sample depends on the sample length L. This influence of interface on the

effective modulus is more obvious when the sample length L is small. This is also qualitatively consistent with the classic composite theory that a lower effective modulus is resulted from the lower volume fraction of the interface with weak modulus. Second, at the beginning of surface welding, a small contact area and low degree of chain connections on the contact portions lead to a small chain density n_f. Increasing the welding time, temperature and pressure will increase n_f, and consequently increase the elastic modulus. Eventually, the second item in the bracket in the denominator will be negligible compared with the first item, which indicates a nearly full recovery of elastic modulus.

6.2.4 Interfacial fracture energy characterization

After finishing the interfacial model and determining the model parameters, we compare the prediction of interfacial fracture energy with the experimental measurement to valid the model effectiveness. As shown in Figure 6.3, the interfacial fracture energy of welded epoxy sample is tested by using the T-peeling tests, where the peeling force was recorded as a function of displacement. Following Griffith's energy balance law, when the welding substrate is elastomeric polymer, the adhesive fracture energy G_c can be calculated as [18, 19]:

$$G_c = \frac{2\bar{P}(1+e)}{b} - E_0 h e^2, \tag{6-10}$$

where $\bar{P}$ is the average peeling force during the steady propagation of crack (from t_1 to t_2), and is calculated as the time average of the real-time peeling force: $\bar{P} = \frac{\int_{t_1}^{t_2} P(t)\,dt}{t_2 - t_1}$. E_0 is the modulus of the material, h is the thickness, b is the width, and e is the elastic strain under force $\bar{P}$. It is generally accepted that the fracture energy across polymer interfaces is dependent on the amount of bridged polymer chains, as well as the rate of separation. Lake and Thomas et al [20] recognized that the fracture energy across polymer interface is amplified, because all the bonds of the polymer have to be activated even though only one bond ultimately breaks. The dependency of the fracture energy on the rate of separation is usually ascribed to bulk viscoelastic processes [21-23], mechanical entanglements near the interface [24-27], or chemical kinetic processes [28-31]. But

regardless of various mechanisms, if the separation rate is constant, the fracture energy is usually linear with the interfacial chain density. For example, in the theory of Chaudhury et al [32], the adhesion energy is formulated as:

$$G_c = \left(\frac{n_f}{2M}\right)\left[\left(\frac{k_b T}{\lambda}\right)\ln\left(\frac{MV\lambda\tau_{-1}}{\alpha kT}\right)\right]^2, \tag{6-11}$$

where n_f is the density of connected polymer chains across the interface, and can be calculated based on Eq. 6-7. τ_{-1} is bond dissociation time, M is the constant associated with polymer chains, V is the peeling velocity, λ is the activation length of a bond, n is the number of bonds in a unit chain. Note that τ_{-1}, M, λ and n are parameters associated with the polymer chain, therefore are constants for the same type of polymers. Eq. 6-11 tells that if two T-peeling tests are conducted under the same peeling speed, we will have $G_c^1/G_c^2 = \bar{n}_f^1/\bar{n}_f^2$. The interfacial fracture energy is linear with the number of connected polymer chains on the interface, which is calculated by Eq.6-7.

6.3. Results and Discussions

6.3.1 Interfacial chain density evolution

Figure 6.6 plots the normalized chain density evolution on the interface with different N applied in Eq. 6-4. The applied temperature is 180 ^{o}C. It is seen that as the number of lattice layer increases, the prediction curves converge at N=20. Since the lattice size is comparable to the radius of gyration of polymer chain, which is typically a few nanometers, the interface affecting depth is predicted to be around tens of nanometers. Beyond this depth, the chain density in the bulk material is unaffected and does not change over time.

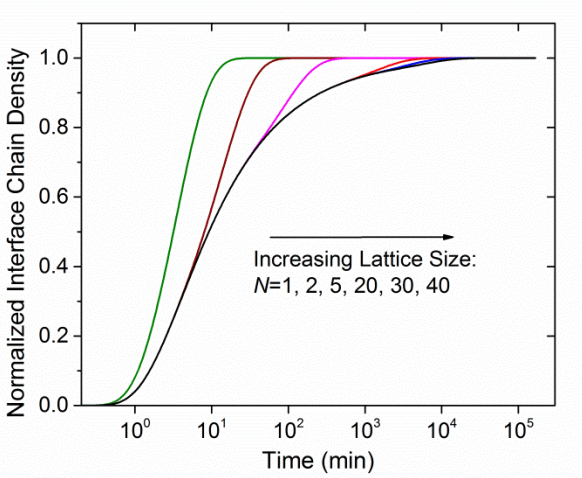

Figure 6.6. Normalized chain density evolution on the interface with different lattice size considered.

The influence of interface on the local chain density distribution beneath the interfacial area is further visualized in Figure 6.7, where the temperature is still 180 ^{o}C. In Figure 6.7a, a 40 by 40 lattice is constructed for each epoxy material and the normalized chain density distribution is plotted at different timing point. Figure 6.7b plots the normalized chain density distribution along the normal direction of the interface. It is seen that after the heating starts, the interfacial chain density increases and the interfacial affecting area expands. In the real thermosetting network, the chain density gradient provides driven force for the diffusion of polymer chains. At the beginning of surface welding process, the sharp contrast of chain density around interface leads to the rapid accumulation of polymer chains on the interface within the first few minute. With the increment of heating time, chains in the subsequent polymer matrix migrate towards the interface, resulting in an expanded gradient area. But due to the decreased the gradient magnitude, the interfacial chain density increasing speed decreases. Finally after 3.6 hours of heating, the adaptive network reaches a homogeneous and dynamic equilibrium state.

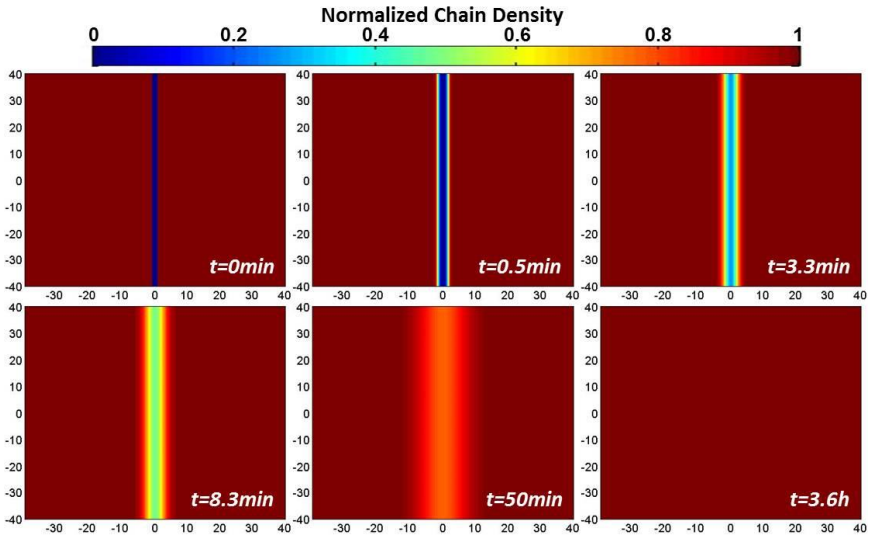

(a)

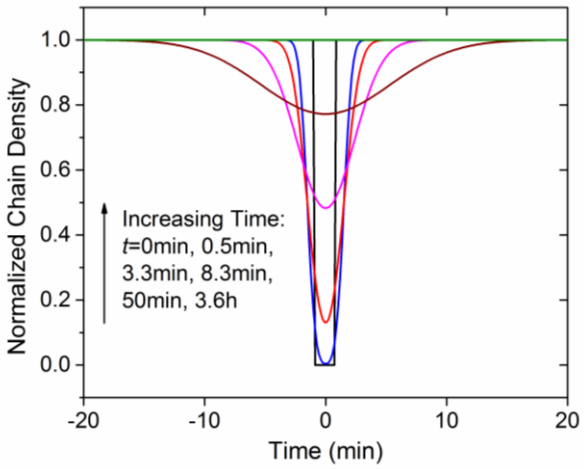

(b)

Figure 6.7**.** (a) Normalized chain density distribution within the lattice model at different timing point. The temperature is 180 ^{o}C. (b) Normalized chain density distribution at different heating time along the normal direction of the interface. The temperature is 180 ^{o}C.

6.3.2 Predictions on the effective modulus of welded sample

In Eq. 6-9, the number of Kuhn segment N_k can be estimated by stress-strain curve of fresh bulk material. For polymeric materials that is in the rubbery state, as the stretch ratio approaches a limiting value $\lambda_c^{\lim}$, the macromolecules are so extended that can no longer accommodate large deformation by rotation[33]. The stress increases dramatically and strain stiffening occurs. From non-Gaussian chain statistics, this limiting stretch ratio $\lambda_c^{\lim}$ is connected to the number of Kuhn segments by $\lambda_c^{\lim} = \sqrt{N_k}$ [34, 35]. In the previous work of Long et al [36], this number of Kuhn segment is determined to be

$N_k = 3.79$. b_k is set to be 1nm, which is the typical Kuhn length of polymers with randomly coiled chains [37]. The number of chains across unit area m can be related to the chain density of bulk material ζ: $m = \frac{1}{2}\bar{L}\zeta$ [20], where $\bar{L}$ is the mean displacement length for a single polymer chain. As shown in Figure 6.8, after properly adjusting the surface roughness constant as C=3.09×10^{-4}, the effective modulus of the welded sample can be adequately predicted with different welding pressure and sample length. The fact that only one parameter is used to predict the curves under different processing conditions confirms the validity of the developed model.

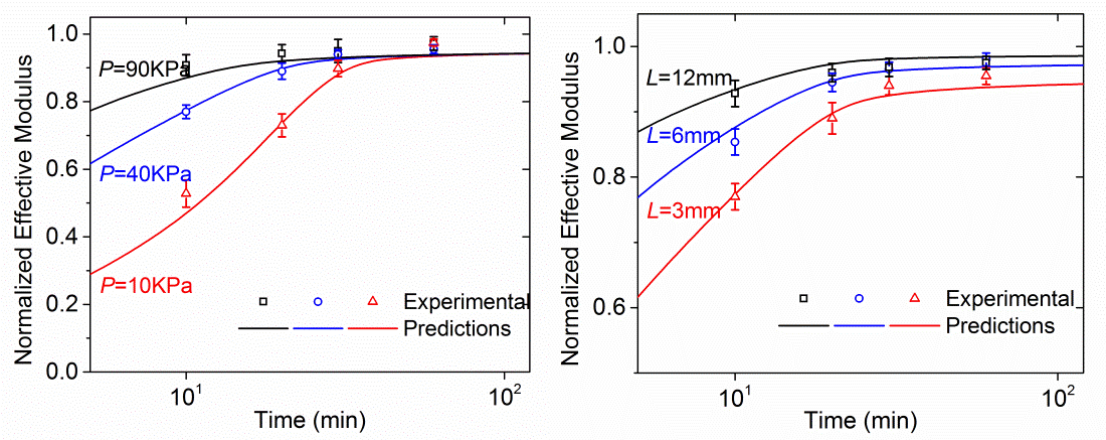

(a) (b)

Figure 6.8. Both experimental results and theoretical predictions of the initial modulus of the welded epoxy sample. The welding temperature is 180 ^{o}C. (a) Initial modulus with different pressure applied. The sample length is 6mm. (b) Initial modulus with different sample length. The applied pressure is 40 KPa.

6.3.3 Predictions on the interfacial fracture energy

The experimental results shown in Figure 6.2 reveal that with enough heating time applied, the initial modulus, stretch ability and strength of the welded epoxy samples could reach the same level as that of the fresh material. In our previous study [38], we also demonstrated that even after being grounded into micro-sized powder and heated long enough, the reprocessed epoxy polymer still process mechanical properties comparable to the fresh material. In this manner, we use the fracture energy of epoxy sample welded for 10 hours (at 180 ^{o}C and with 90 KPa applied) as the normalizer. According to stress-strain behavior shown in Figure 6.2a, it is reasonable to assume that the applied welding condition will achieve a full recovery of chain density on the

interface. By using the T-peeling test, the fracture energy of the welded epoxy sample is measured as 1887.7J/m^2.

Figure 6.9 shows comparasion between the experimental results and theoretical predictions of normalized interfacial fracture energy. It is seen that the developed interfacial model could predict the time, temperature and pressure dependent fracture energy with adequate accuracy. Besides, parametric studies on the welding pressure at different temperatures reveal some general features. First, for each welding temperature, there exists a critical welding time, before which the development of interfacial fracture energy is sensitive to the pressure. A higher pressure helps to increase the real contact area by squeezing surface asperities, and consequently assists the accumulation of connected polymer chains on the interface. After this critical welding time, the predictions of fracture energy join together indicating the independency of welding pressure. Second, below the critical welding time, the sensitivity of the welding pressure is weaker when the welding temperature is lower. This is because at low temperature, although increasing pressure still increases the real contact area, the fracture energy development is limited by the sluggish BER kinetics on the interface. Third, since BERs keep on releasing the elastic energy in surface asperities, even with 2KPa pressure, the fracture energy can reach the same level of that with high pressure applied after the critical heating time. Therefore, if highly recovered fracture energy on the interface is the manufacturing goal, excessively high pressure is unnecessary in terms of shortening the welding process.

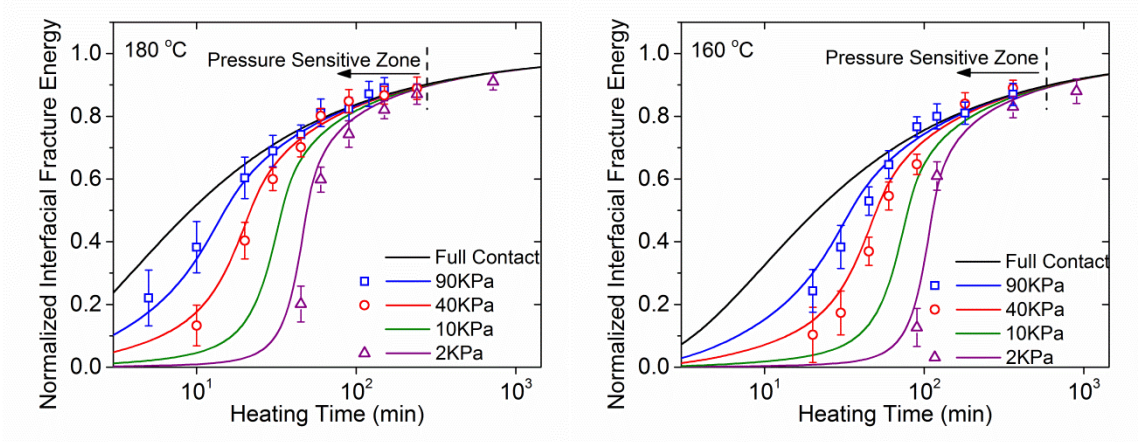

(a) (b)

Figure 6.9. Both experimental results and theoretical predictions of the normalized interfacial fracture energy. The experimental results are plotted as dots. (a) Normalized interfacial fracture energy of epoxy samples after being welded at 180 ^{o}C for different time and with different pressure applied. (b) Normalized interfacial fracture energy of epoxy samples after being welded at 140 ^{o}C for different time and with different pressure applied.

6.3.4 A master map for effective modulus and fracture energy

The aforementioned discussions reveal that both effective modulus and interfacial fracture energy of welded samples are dependent on processing time, temperature and pressure. These dependencies are originated from the time and temperature dependent BER kinetics, which follows the TTSP. Therefore, the real contact area and the interfacial chain density also follow the TTSP and can be mapped into a reference temperature T_r:

$$A(t,T) = A(t_r,T_r) \tag{6-12a}$$

$$\Delta(t,T) = \Delta(t_r,T_r) \tag{6-12b}$$

Usually, the new timing scale is called reduced time [39], which is the physical time divided by the corresponding shift factors

$$t_r = \int_0^t \frac{ds}{\alpha_T} \tag{6-13}$$

In this manner, the time and temperature dependency of surface welding can be unraveled by the reduced processing time. Different thermo-temporal processing conditions can be measured by the reduced processing time at the reference temperature; the reduced processing time and pressure determine both effective modulus and interfacial fracture energy. This process inspires the creation of a master map for the prediction of effective modulus, as shown in Fig. 12, where the left quadrant shows the normalized effective modulus as a function of both pressure and reduced processing time, and the right quadrant shows the conversion of the reduced processing time (the vertical axis) to the physical processing time (the vertical axis) at different processing temperatures (individual curves). For a given welding condition with a processing temperature and time at that temperature, one can obtain the reduced processing time from the right quadrant and then determine the normalized effective modulus combining the pressure by using the left quadrant.

In addition to the prediction, Figure 6.10 also reveals some general features of the effective modulus under various processing conditions. First, increasing processing

temperature will always increase the reduced processing time at a given physical heating time, and consequently increase the effective modulus, which is originated from the increment of BER rate and real contact areas. Second, within a specific pressure range, increasing pressure will also increase the effective modulus since it will assist the accumulation of real contact areas. Since an excessively high processing temperature might impair the integrality and stability of network, one can choose to increase the processing pressure instead in order to achieve the same level of effective modulus. Third, there exists a critical pressure magnitude (~130KPa), above which the effective modulus is independent on the pressure applied, but is determined by the temperature dependent BER rate. Similarly, a master prediction map for the interfacial fracture energy is also constructed as shown in Figure 6.11, which reveals similar rules. Generally, the constructed master prediction maps provide a facile strategy to select and optimize the processing conditions for an CAN.

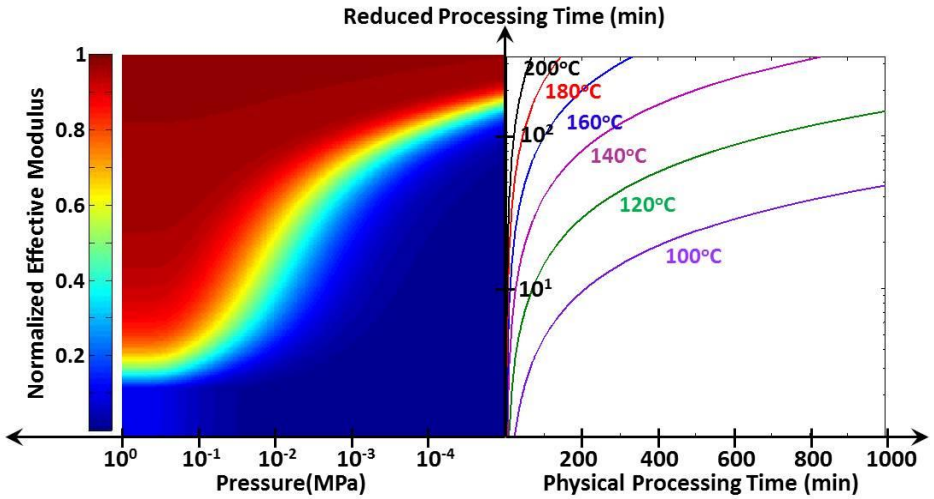

Figure 6.10. A master map for the prediction of effective modulus of the welded sample. The reference temperature for the reduced processing time is 160 ^{o}C

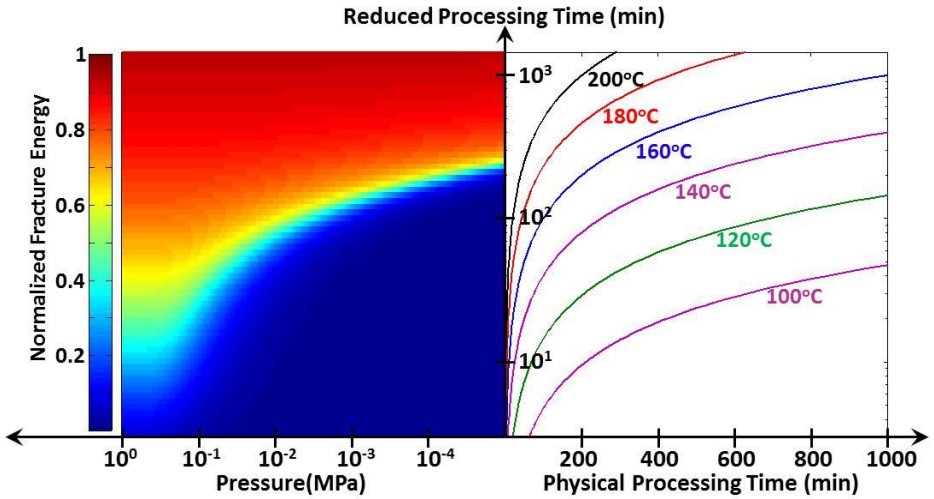

Figure 6.11. A master map for the prediction of interfacial fracture energy of the welded sample. The reference temperature for the reduced processing time is 160 ^{o}C

6.4 Conclusion

Thermo-responsive covalent adaptive networks (CANs) could be welded on the interfaces when the temperature is sufficiently high to activate the internal BERs. In this chapter, experimental observations show that such surface welding effect is dependent on the welding time and temperature. Besides, pressure affects the welding efficiency, which contradicts to our previous understanding of covalent chemical reactions that are not pressure sensitive when the pressure magnitude is moderate. In this chapter, we developed a theoretical model to study the dependency of CAN interfacial kinetics on the applied thermal and mechanical fields. Due to the surface roughness, the pressure will affect the real contact area on the interface, and consequently influence the mechanical properties of welded thermosetting polymer. On the real contact area, the chain density increment is only dependent on the welding time and temperature, and such dependency can be characterized based on the BER kinetics of bulk material. The model predictions agree well with experimental observations on the elastic modulus and interfacial fracture energy of welded thermosetting polymers. Due to the concise modeling frame and effectiveness of the developed model, it can be easily extended to other types of CANs with different stimuli, such as light and moisture etc.

6.5 References

1. Stukalin, E.B., et al., *Self-Healing of Unentangled Polymer Networks with Reversible Bonds.* Macromolecules, 2013. **46**(18): p. 7525-7541.
2. Rottach, D.R., et al., *Molecular dynamics simulations of polymer networks undergoing sequential cross-linking and scission reactions.* Macromolecules, 2007. **40**(1): p. 131-139.
3. Montarnal, D., et al., *Silica-Like Malleable Materials from Permanent Organic Networks.* Science, 2011. **334**(6058): p. 965-968.
4. *ASME-D 1876. Standard test method for peel resistance of adhesives (T-peel test).*
5. Bowman, C.N. and C.J. Kloxin, *Covalent Adaptable Networks: Reversible Bond Structures Incorporated in Polymer Networks.* Angewandte Chemie-International Edition, 2012. **51**(18): p. 4272-4274.
6. Leibler, L., M. Rubinstein, and R.H. Colby, *Dynamics of Reversible Networks.* Macromolecules, 1991. **24**(16): p. 4701-4707.
7. Hertz, H., *Ueber die Berührung fester elastischer Körper.* Journal für die reine und angewandte Mathematik, 1882. **92**: p. 156-171.
8. Greenwoo.Ja and Williams.Jb, *Contact of Nominally Flat Surfaces.* Proceedings of the Royal Society of London Series a-Mathematical and Physical Sciences, 1966. **295**(1442): p. 300-&.
9. A.W. Bush, R.D. Gibson, and G.P. Keogh, *The Elastic Contact of a Rough Surface* Wear, 1975. **35**: p. 87-111.
10. A.W. Bush, R.D. Gibson, and G.P. Keogh, *The Limit of Elastic Deformation in the Contact of Rough Surfaces* Mech. Res. Commun.,, 1976. **3**: p. 169-174.
11. Persson, B.N.J., *Adhesion between an elastic body and a randomly rough hard surface.* European Physical Journal E, 2002. **8**(4): p. 385-401.
12. Persson, B.N.J., *Contact mechanics for layered materials with randomly rough surfaces.* Journal of Physics-Condensed Matter, 2012. **24**(9).
13. Persson, B.N.J., *Contact mechanics for randomly rough surfaces.* Surface Science Reports, 2006. **61**(4): p. 201-227.
14. Persson, B.N.J., et al., *Contact area between a viscoelastic solid and a hard, randomly rough, substrate.* Journal of Chemical Physics, 2004. **120**(18): p. 8779-8793.
15. Persson, B.N.J., et al., *On the nature of surface roughness with application to contact mechanics, sealing, rubber friction and adhesion.* Journal of Physics-Condensed Matter, 2005. **17**(1): p. R1-R62.
16. de Gennes, P.G., *Scaling Concepts in Polymer Physics.* Cornell University Press, Ithaca, 1979.
17. Jensenius, H. and G. Zocchi, *Measuring the spring constant of a single polymer chain.* Physical Review Letters, 1997. **79**(25): p. 5030-5033.
18. Moore, D.R., G.W. James, and P. A., *Fracture mechanics testing methods for polymers, adhesives and composites.* Elsevier, 2001. **28**.
19. Kawashita, L.F., D.R. Moore, and J.G. Williams, *Protocols for the measurement of adhesive fracture toughness by peel tests.* Journal of Adhesion, 2006. **82**(10): p. 973-995.

20. Lake, G.J. and A.G. Thomas, *Strength of Highly Elastic Materials.* Proceedings of the Royal Society of London Series a-Mathematical and Physical Sciences, 1967. **300**(1460): p. 108-&.
21. Raphael, E. and P.G. Degennes, *Rubber Rubber Adhesion with Connector Molecules.* Journal of Physical Chemistry, 1992. **96**(10): p. 4002-4007.
22. Gent, A.N. and J. Schultz, *Effect of Wetting Liquids on Strength of Adhesion of Viscoelastic Materials.* Journal of Adhesion, 1972. **3**(4): p. 281-&.
23. Andrews, E.H. and A.J. Kinloch, *Mechanics of Adhesive Failure .1.* Proceedings of the Royal Society of London Series a-Mathematical and Physical Sciences, 1973. **332**(1590): p. 385-399.
24. Brown, H.R., *Chain Pullout and Mobility Effects in Friction and Lubrication.* Science, 1994. **263**(5152): p. 1411-1413.
25. Ruths, M. and S. Granick, *Rate-dependent adhesion between polymer and surfactant monolayers on elastic substrates.* Langmuir, 1998. **14**(7): p. 1804-1814.
26. Creton, C., H.R. Brown, and K.R. Shull, *Molecular-Weight Effects in Chain Pullout.* Macromolecules, 1994. **27**(12): p. 3174-3183.
27. Deruelle, M., L. Leger, and M. Tirrell, *Adhesion at the Solid-Elastomer Interface - Influence of the Interfacial Chains.* Macromolecules, 1995. **28**(22): p. 7419-7428.
28. Perutz, S., et al., *Adhesion between hydrolyzed surfaces of poly(dimethylsiloxane) networks.* Macromolecules, 1997. **30**(25): p. 7964-7969.
29. Blake, T.D. and J.M. Haynes, *Kinetics of Liquid/Liquid Displacement.* Journal of Colloid and Interface Science, 1969. **30**(3): p. 421-&.
30. Kendall, K., *Peel Adhesion of Solid Films - Surface and Bulk Effects.* Journal of Adhesion, 1973. **5**(3): p. 179-202.
31. Mangipudi, V.S. and M. Tirrell, *Contact-mechanics-based studies of adhesion between polymers.* Rubber Chemistry and Technology, 1998. **71**(3): p. 407-448.
32. Chaudhury, M.K., *Rate-dependent fracture at adhesive interface.* Journal of Physical Chemistry B, 1999. **103**(31): p. 6562-6566.
33. Qi, H.J., K. Joyce, and M.C. Boyce, *Durometer hardness and the stress-strain behavior of elastomeric materials.* Rubber Chemistry and Technology, 2003. **76**(2): p. 419-435.
34. Westbrook, K.K., et al., *A 3D finite deformation constitutive model for amorphous shape memory polymers: A multi-branch modeling approach for nonequilibrium relaxation processes.* Mechanics of Materials, 2011. **43**(12): p. 853-869.
35. Yu, K., et al., *A thermomechanical constitutive model for an epoxy based shape memory polymer and its parameter identifications.* Mechanics of Time-Dependent Materials, 2014. **18**(2): p. 453-474.
36. Long, K.N., *The mechanics of network polymers with thermally reversible linkages.* Journal of the Mechanics and Physics of Solids, 2014. **63**: p. 386-411.
37. Prasad, A.V.S.S., T. Grover, and S. Basu, *Coarse grained molecular dynamics simulation of crosslinking of DGEBA epoxy resin and estimation of the adhesive strength.* International Journal of Engineering, Science and Technology 2010. **2**(4): p. 17-30.

38. Yu, K., et al., *Reprocessing and recycling of thermosetting polymers based on bond exchange reactions.* Rsc Advances, 2014. **4**(20): p. 10108-10117.
39. Yu, K., Q. Ge, and H.J. Qi, *Reduced time as a unified parameter determining fixity and free recovery of shape memory polymers.* Nature Communications, 2014. **5**.

CHAPTER 7

OVERALL CONCLUSIONS AND RECOMMENDED FUTURE WORK

7.1 Overall Conclusions

The overall objective of my study is to understand the complex thermomechanical behaviors of active network polymers through experimental and theoretical investigations. Two representative polymer systems are selected in this dissertation: shape memory polymers (SMPs) and covalent adaptive networks (CANs) with bond exchange reactions (BERs). Both polymers are active in performing prescribed functions upon changing temperature. The research strategy include experimental testing on the material thermomechanical behaviors, and then develop constitutive models to predict material behavior, reveal working mechanism and assist design for engineering applications.

Specifically, by using a one-dimensional (1D) thermoviscoelastic constitutive model, we studied several new and interesting shape memory effects in thermos-sensitive amorphous network polymers, which advance our traditional understanding of this material. For example, by studying the influence of stretch induced softening effect on the free recovery of SMPs, we demonstrated that the material equilibrium modulus provides the driven force to the shape recovery of SMPs; by examining the multi-shape memory effect, we revealed the energy releasing mechanism during the shape recovery of SMPs; by investigating the polymer temperature memory effect (TME), we showed how both programing and recovery conditions will affect the free recovery behavior in group. Subsequently, based on the experimental observations, we generalized a unified method to predict the shape memory performance of thermo-rheologically simple SMPs under different thermo-temporal conditions. The fundamental conclusion is that the influence of programming conditions to free recovery can be unified by a reduced programming time that uniquely determines shape fixity, which consequently uniquely determines the shape recovery with a reduced recovery time. The developed prediction method is independent on the model details. After extending the 1D constitutive model into three-dimensional

(3D) finite deformation model, we examined the thermomechanical and shape recovery behaviors of two types of SMP composites, which is respectively reinforced by magnetic particles and microvasculars. These two materials represent a common group of SMP composites which rely on internal heating sources to volumetrically heat up the SMP matrix. The results revealed some general features of the shape memory behavior: first, the initial thermal conduction and thermally induced shape recovery successively dominate the total shape recovery process; second, there always exists a critical filler size, below which the initial heat transfer can occur almost instantaneous and the shape recovery rate is independent on the filler size.

For the CANs, we studied BER induced stress relaxation, surface welding, reprocessing and recycling capabilities. The stress relaxation behaviors at different stoichiometric ratios help us to establish the connection among BER kinetics, network relaxation modulus and glass transition temperature (T_g). That is, the network relaxation time is dependent on the BER kinetics, where the reaction energy barrier is linear with T_g. We also correlated the BER kinetics with surface welding effect through a continuum level constitutive model, where the model parameters can be determined by testing the properties of bulk material. During the surface welding, the polymer chains migrate towards interface and reconnect there. The migration is essentially a diffusion process and the diffusivity is only dependent on the rate of exchange reactions. In addition, due to the surface roughness, the pressure will affect the real contact area on the interface, and consequently influence the mechanical properties of welded thermosetting polymer. The model predictions agree well with experimental observations on the elastic modulus and interfacial fracture energy of welded thermosetting polymers.

7.2 Future Work Recommendation

The research in my dissertation may be further developed in the following two ways:

1. Developing 3D finite deformation computational frame to combine both BER induced stress relaxation and surface welding effect of CANs. Such a 3D constitutive model will enable us to study complex 3D problems, such as the reprocessing and recycling effects under the influence of temperature and pressure. However, as we revealed in Chapter 6, the dependency of real contact area on the surface roughness leads

to a time-convolution type interfacial chain density evolution, which is computationally expensive to capture in existing FEM packages. In this case, developing new and effective computational methods will be a challenge.

2. Combining SMPs with BERs to develop novel multifunctional active polymers. Such combination will advance the current applications of SMPs to a new level. One notable example is the free standing two-way shape memory polymers [1, 2] based on the liquid crystalline elastomers, where network topology will be evolved along the programming deformation at high temperature. This is a truly remarkable progress in developing two-way SMPs, and its thermomechanical and two-way shape changing properties can be studied by using approaches developed in this dissertation.

7.3 References

1. Pei, Z.Q., et al., *Mouldable liquid-crystalline elastomer actuators with exchangeable covalent bonds.* Nature Materials, 2014. **13**(1): p. 36-41.
2. Yakacki, C.M., et al., *Tailorable and programmable liquid-crystalline elastomers using a two-stage thiol- acrylate reaction* RSC Advances (availabe online), 2015(DOI: 10.1039/c5ra01039j).

VITA

Kai Yu

Mr. Yu was born in the Shan Dong Province of China, hometown of the Confucius. He received his Bachelor's degree in Engineering Mechanics from Harbin Institute of Technology (China) in 2008. After coming to the United States in 2011, he was initially studying in the University of Colorado at Boulder, and then transferred to Georgia Tech in 2014 along with his advisor to continue the Ph.D study.

When he is not working on his research, Mr. Yu enjoys playing basketball and table tenuis. He is also obsessed to the world history, particularly the ancient and modern history of China.